1999

PH.D.

X. DU
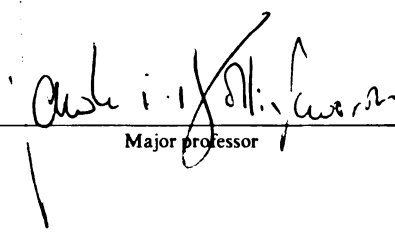
This is to certify that the

dissertation entitled

Lipid Spatial Alignment and Motional Dynamics: the
Two Important Factors that Determine Membrane Properties

presented by

Xiaoyang Du

has been accepted towards fulfillment
of the requirements for

___Ph.D.___ degree in _Chemistry_

_____
Major professor

Date _02/01/99_

PLACE IN RETURN BOX to remove this checkout from your record.
TO AVOID FINES return on or before date due.
MAY BE RECALLED with earlier due date if requested.

DATE DUE	DATE DUE	DATE DUE

1/98 c/CIRC/DateDue.p65-p.14

LIPID SPATIAL ALIGNMENT AND MOTIONAL DYNAMICS: THE TWO IMPORTANT FACTORS THAT DETERMINE MEMBRANE PROPERTIES

By

Xiaoyang Du

A DISSERTATION

Submitted to
Michigan State University
in partial fulfillment of the requirements
for the degree of

DOCTOR OF PHILOSOPHY

Department of Chemistry

1999

ABSTRACT

LIPID SPATIAL ALIGNMENT AND MOTIONAL DYNAMICS: THE TWO IMPORTANT FACTORS THAT DETERMINE MEMBRANE PROPERTIES

By

Xiaoyang Du

Membranes are formed through lipid self-assembly. The properties of the self-assembled membrane are determined critically by lipid spatial alignment and lipid chain motional dynamics. The goal of this dissertation research was to obtain both lipid alignment information and motional dynamics information in order to have a fuller understanding of lipid membrane.

The study on lipid spatial alignment has been conducted in a lipid multilayer system. A new methodology utilizing phase contrast and confocal reflection microscopy has been developed to characterize the partially ordered layer system based on light-lipid interactions. Four types of lipid domain structures, oily streaks, polygonal arrays, bubble domains and stripe domains were visualized and analyzed in detail by phase contrast and confocal reflection microscopy. The images obtained through phase contrast and confocal reflection microscopy have better correlation with lipid alignment models than those through the conventional polarizing microscopy. The complementary nature of polygonal arrays has been revealed by confocal reflection microscopy. Both confocal reflection microscopy and phase contrast microscopy have been used to characterize the stripe to bubble domain transition processes.

Under thermal energy, the formation of a bubble domain is through a continuous contracting process of a stripe domain. Under hydrodynamic flow, a bending stripe

corresponding to the activation state of the domain transition process has been clearly visualized. These experimental observations directly showed that the stripe-to-bubble domain transition process is a typical first order phase transition process. The domain transition has been further analyzed in terms of modulated phase based on the framework of competing interactions.

A novel membrane probe with pyrene moieties covalently attached to the end of both lipid chains and a positive charge at the lipid head group has been utilized to study membrane dynamics. This probe in isotropic solvents forms a strong intramolecular excimer through the trans-gauche isomerization process. The deviation of power dependence of excimer formation rate on solvent viscosity from unity in diffusive limit was analyzed in great detail in terms of reaction dynamics theory in solution phase and found to be due to the reactive mode coupling to non-reactive modes. The mode coupling and long barrier crossing and re-crossing time in the diffusive limit enable the reaction to choose a reaction pathway with least friction, which, in turn, enhances the excimer formation.

This novel membrane probe was also incorporated into DPPC large unilamellar vesicles. Based on fluorescence measurement, the enthalpy of main phase transition at low pH is significantly reduced compared to the enthalpy at neutral pH condition, which is in excellent agreement with the measurement based on differential scanning calorimeter. Analyzing the magnitude of E/M ratio and the apparent activation energy of the excimer formation under two pHs indicates that the membrane net surface charge strongly affects lipid chain mobility. The enthalpy reduction of main phase transition is the direct consequence of lipid chain mobility change.

To my grandmother who taught me love

and

To my parents who teach me hard working.

ACKNOWLEDGEMENTS

TABLE OF CONTENTS

LIST OF TABLES

LIST OF FIGURES

xiii

LIST OF ABBREVIATIONS

DHPA	dihexadecyl phosphatidic acid
DMPC	dimyristoyl phosphatidylcholine
DPPA	dipalmitoyl phosphatidic acid
DPPC	dipalmitoyl phosphatidylcholine
DPPS	dipalmitoyl phosphatidylserine
DSC	differential scanning calorimetry
E/M	excimer-to-monomer fluorescence intensity ratio
FRAP	fluorescence recovery after photobleaching
GLE	generalized Langevin equation
L_α	lamellar liquid crystalline phase
L_β	lamellar gel phase
LSM	Laser Scanning Microscopy
LUV	large unilamellar vesicle
MLV	multilamellar vesicle
PBA	pyrene butyric acid
PA	phosphatidic acid
PC	phosphatidylcholine
PE	phosphatidylethanolamine
PS	phosphatidylserine
TST	transition state theory

Chapter 1

Literature Review

Membrane and Lipid Domain Structures

In 1972, Singer and Nicolson (1) proposed the widely accepted fluid mosaic model as shown in Figure 1.1 to explain the structure, organization and motion of biological membrane. In this model, lipids are organized in the form of a bilayer supporting peripheral and integral proteins. This model considers the lipid bilayer as a two-dimensional fluid in which lipids and proteins are free to diffuse. As a direct consequence, both types of molecules would be expected to be randomly distributed within the membrane and lack any significant degree of lateral order. Even though the fluid mosaic model served as a conceptual foundation for the current understanding of membrane architecture, it is too simple to explain many complex phenomena of biological membrane. More and more evidence has shown that the molecular distribution in membrane is in fact heterogeneous with high degree of organization such as lipid domains.

A lipid domain can be defined in the most general way as any area in a membrane which differs in lipid composition from other areas in the membrane (2). Lipid domain can be formed due to multiple-lipid phases. The coexistence of lipids in more than one phase within a membrane is synomous with existence of lipid domains.

The simple and elegant experiment of this kind is the lipid monolayers at the air-water interface by epifluorescence microscopy. Because of the simplicity and controllability through temperature and monolayer surface pressure, the phenomena of
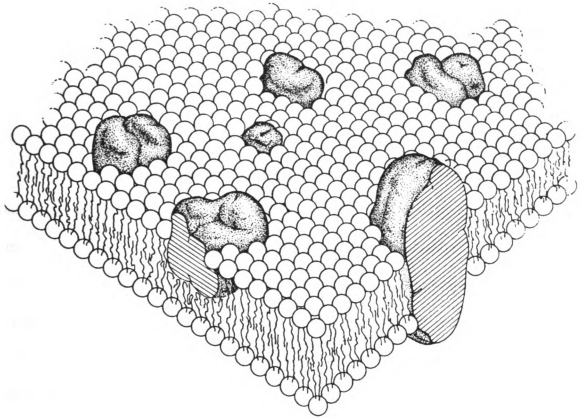
Figure 1.1: The fluid mosaic model of biological membranes in which the proteins and lipids form a two-dimensional viscous fluid. Adapted from reference 1.

domain size and shape have been extensively studied both experimentally and theoretically. The representative work has been done in McConnell's laboratory (3) and in Möhwald's laboratory (4). Typically, this experiment is carried out by incorporating amphiphilic fluorescent probes into the monolayer films at concentrations of the order of 1 mole %. Experiment has shown that the influence of the probe at such low concentration can be neglected (5). By fixing temperature and varying surface pressure, black "islands" are surrounded by white "ocean"(6). The "islands" are in lipid gel phase in which lipids are tightly packed and lipid chain is in an all-trans conformation. In contrast, the white area is in liquid crystalline phase. The "islands" are black because the tight packing of lipids "squeezes" the probe molecule out of the "islands" (7). In another word, the probe is not soluble in gel phase. The gel domains are compact and their size distribution is monodisperse with the mean size increasing with surface pressure. In addition, a long range order exists in the gel domains, for example, a hexagonal superlattice in this case.

The gel domain depends not only on the surface pressure but also on the molecular chirality. Weis and McConnell performed an elegant experiment (8) which shows that the handedness of the gel domains is directly related to the enantiomorphic configuration of the lipids composing the monolayer. The shape of these domains provides direct visual evidence for long range orientational order in two-dimensional crystals.

The coexistence of gel and liquid crystalline can happen not only in monolayer system as discussed above but also in model membrane. The most well-studied example of this kind is binary systems in which two different lipids can coexist in the liquid crystalline and gel phase over a fairly large temperature range (2, 9). When a two-phase system is present, similar to monolayer system, one component exists as "islands" in the sea of the other component. As the amount of the first component increases, the area occupied by the "islands" grows larger until they become the connected phase. The compositional points on the phase diagrams at which the liquid crystalline phase connects have been defined by fluorescence recovery after photobleaching (FRAP) for several gel-liquid crystalline mixtures: dimyristoyl phosphatidylcholine and distearoyl phosphatidylcholine (10), dimyristoyl phosphatidylcholine and dipalmitoyl phosphatidylcholine (11), 1-docasanoyl, 2-dodecanoyl phosphatidylcholine and diheptadecanoyl phosphatidylcholine (12), N-lignoceroyl-dihydrogalactosylceramide and dipalmitoyl phosphatidylcholine (13).

Lipid domains can also be formed when negatively charged lipids interact with ions. The notable examples are the addition of a divalent cation, such as calcium, to liquid crystalline mixtures of phosphatidylcholine or phosphatidylethanolamine with a negatively charged lipids, such as phosphatidic acid or phosphatidylserine, results in a lateral phase separation which can involve formation of a cochleate phase (14). Domains of this type were observed by freeze-etch electron microscopy when calcium or polylysine was added to an equimolar mixture of dioleoyl phosphatidic acid and dioleoyl phosphatidylcholine (15). Larger lipid domains enriched in phosphatidic acid have been

observed by fluorescence digital imaging microscopy of large phosphatidylcholine vesicles containing small amounts of phosphatidic acid (16)or erythrocyte ghost (17) in the presence of calcium.

Lipid Structures and Phase Behaviors

Lipids are amphiphilic molecules. They contain both a hydrophilic and a hydrophobic moiety. The three major kinds of membrane lipids are phopholipids, glycolipid and cholesterol. The hydrophobic and hydrophilic units of the three kinds of lipids are listed in Table 1.1 (18). The structures of some lipids are shown in Figure 1.2. The diversity of lipid structures is manifested by the variation of aliphatic chain length, branching and unsaturation in lipid hydrophobic region and the change of structures, shape and charge in lipid headgroup.

Table 1.1: Hydrophobic and hydrophilic units of three major membrane lipids, adapted from reference 18.

Membrane lipids	Hydrophobic unit	Hydrophilic unit
Phospholipids	Fatty acid chains	Phosphorylated alcohol
Glycolipids	Fatty acid chains and hydrocarbon chain of sphingosine	One or more sugar residues
Cholesterol	Entire molecule except for OH group	OH group at C-3

The lipid phase behavior depends on the intra- and inter-molecular forces of the lipid molecules. The aliphatic chain of the lipid experiences steric repulsive and van der

6
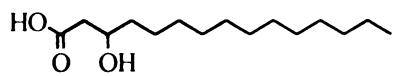
3-hydroxytetradecanoic acid
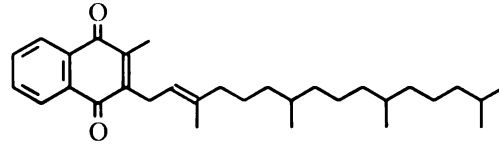
Vitamin K₁
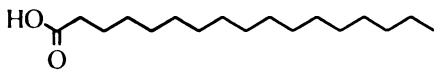
palmitic acid

Cholesterol
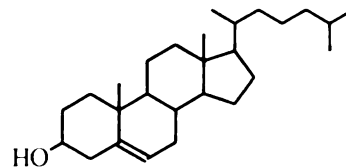
R= -OH   phosphatidic acid
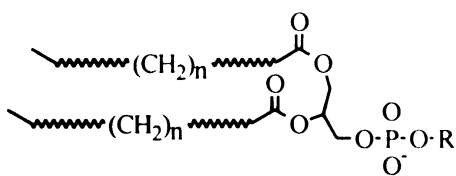
general structure of a
diacylglycerophospholipid

phosphatidylcholine

phosphatidylethanolamine

phosphatidylserine

phosphatidylglycerol

phosphatidylinositol
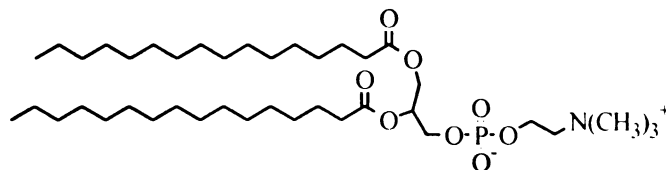
dipalmitoylphosphatidylcholine

Figure 1.2. The chemical structures of some common membrane components.

7

Waals attractive forces. The polar headgroup of lipids are influenced by steric repulsion, electrostatic interactions and hydration forces (19). The molecular forces of both the hydrophobic and the hydrophilic regions of the lipids are balanced to provide the minimum free energy of the lipid aggregate. This delicate balance of forces dictates their lipid aggregate properties and consequently their phase behavior. The factors that influence the delicate balance include temperature, pressure, pH, ionic strength and many others. In this section, I limit my discussion to only three factors: temperature, pH and ionic strength which are closely related to the research I have done in the following chapters.

Temperature is the most dramatic factor that affects the lipid phase behavior. Take the phase behavior of dipalmitoyl phosphatidylcholine (DPPC) (see Figure 1.2 for DPPC structure) as an example. Dipalmitoylphosphatidylcholine (DPPC) is in the lamellar gel ($L_{\beta'}$) phase below 35°C (Figure 1.3). When this lipid is heated to 35°C, it undergoes a transition to the ripple phase ($P_{\beta'}$). Continued heating results in another phase transition at 42°C, the gel to liquid crystalline (L_α) main phase transition. This cooperative phase transition involves the conversion of relatively ordered gel-state bilayer, in which the hydrocarbon chains exist predominately in their rigid, extended, all-trans conformation, to a relatively disordered liquid crystalline bilayer, in which the hydrocarbon chains contain a number of gauche conformers and exhibit greatly increased rates of intra- and inter-molecular motions. The gel to liquid crystalline phase transition is accompanied by a pronounced lateral expansion and a decrease in the bilayer thickness as well as by a small increase in total volume occupied by each lipid molecules (20).

35°C → 42°C →

Lamellar Gel   Ripple   Lamellar Liquid Crystalline
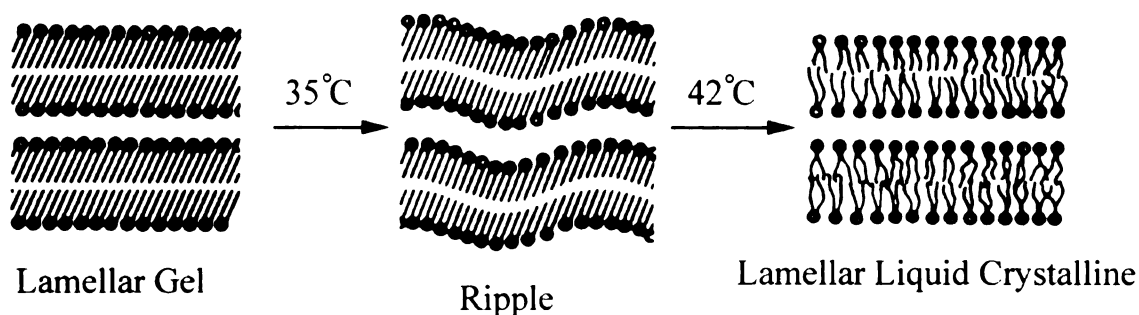
Figure 1.3. A schematic of the phase behavior of dipalmitoylphosphatidylcholine as function of temperature. Modified from reference 20.

pH is another important factor to lipid phase behavior especially to ionizable lipids such as phosphatidic acid (PA) and phosphatidylserine (PS). For instance, the main phase transition temperature of dipalmitoyl phosphatidic acid (DPPA) at pH 6.5 is 67 ^{0}C while only 58 ^{0}C at pH 9.1 (21). The significant change in T_m generally occur over the pH range in which there is protonation/deprotonation of ionizable group. DPPA at pH 6.5 is a single charged lipid. It becomes double charged at pH 9.1 through deprontonation of phosphatidic acid. The protonation and/or deprotonation of ionizable groups would inevitably alter polar headgroup and consequently change the relative stability of the gel phase by their effects on the close packing interactions of the lipid molecules. Generally, increasing charge density at membrane surface decreases the main phase transition temperature as shown in Figure 1.4. The only exception is phosphatidylcholine (PC). At pH 0 in which dimyristoyl phosphatidylcholine (DMPC) and dipalmitoyl phosphatidylcholine (DPPC) are positively charged, T_m of DMPC and DPPC is 36 ^{0}C and 50 ^{0}C, respectively. At pH 8 in which DMPC and DPPC are zwitterionic, however, T_m of DMPC and DPPC decreases to 23 ^{0}C and 42 ^{0}C, respectively (22). This is probably

9
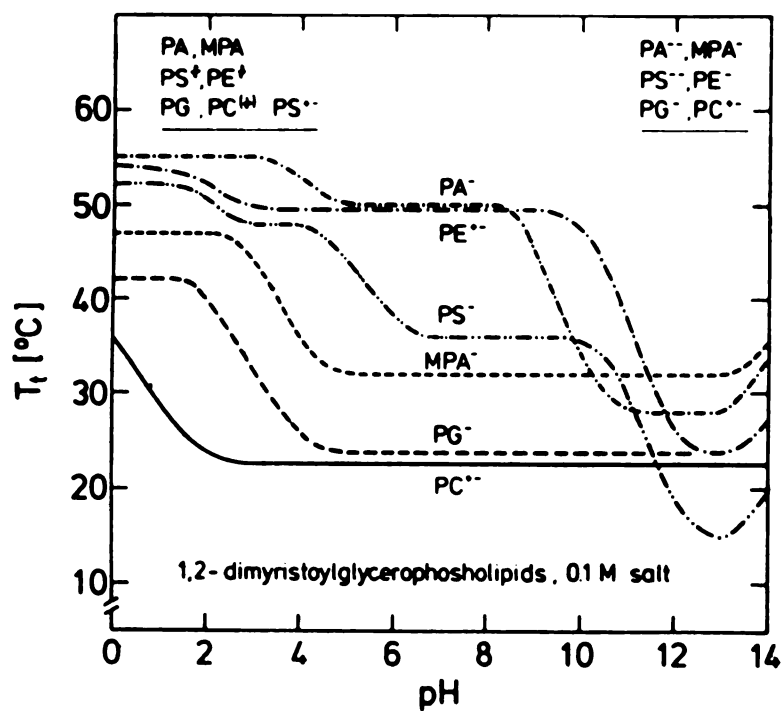
Figure 1.4. pH dependence of the chain-melting phase transition temperatures of various dimyristoylphospholipid bilayers. The superscripts on each lipid give the lipid charge. Adapted from reference 20.

because the close packing of DMPC and DPPC renders a strong short-range interaction between the phosphate ester moieties. The neutralization of phosphate ester at low pH decreases the repulsive force and increases the stability of gel phase. The positive charged trimethyl amonium moiety near the end of phosphatidylcholine group has relatively higher freedom and affected much less by the close packing of aliphatic chain than phosphate ester. Furthermore, the trimethyl amonium is located in the buffer region. The screening due to ions in buffer significantly reduces the short range interaction of the positively charged trimethyl amonium. Therefore, the stability of PC gel phase is mainly determined by the charge at phosphate ester moiety.

The decrease on main phase transition temperature due to membrane net surface charge is often accompanied by a decrease on phase transition enthalpy (ΔH). One of the contributions to the enthalpy reduction is the electrical double layer energies ($\Delta \Gamma$) as proposed by Trauble etal (22, 23). If charge difference is 1 at two pHs, the $\Delta \Gamma$ can be approximated by

$$\Delta \Gamma = \Gamma(L_\alpha) - \Gamma(L_\beta) = -2RT \times \frac{f_\alpha - f_\beta}{f_\alpha} \qquad (1.1)$$

R and T have their usual meaning. f_α and f_β are the lipid mean molecular area at liquid crystalline (L_α) and get state (L_β) respectively. $\Delta \Gamma$ calculated from Equation. 1.1 is in the order of 1.5 kJ/mol. Because f_α is always greater than f_β, the negative value of $\Delta \Gamma$ signifies that the charge at membrane surface reduces the phase transition enthalpy.

However, this reduction of ΔH due to electrical double layer only accounts a very small portion of total enthalpy reduction. Jacobson and Papahadjopoulos (21) reported that ΔH decreases from 21.7 kJ/mol to 12.1 kJ/mol when negative charge of DPPA increases from 1 (at pH 6.5) to 2 (at pH 9.5). They postulated that the ionization of headgroup to produce charged bilayer will produce structural alteration in the hydrocarbon region especially in gel state. More specifically, the repulsive force between ionized phosphate groups would cause a disordering effect in the lipid hydrocarbon region, which, in turn, decreases the van der Waals forces between lipid chain. Therefore, ΔH is reduced. MacDonald etal (24) found that the phase transition enthalpy of dipalmitoyl phosphatidylserine (DPPS) falls from about 38 kJ/mol to about 13 kJ/mole as the protonated DPPS is converted to the ionized form. They attributed enthalpy reduction mainly to hydrogen bonding for the protonated form. Jähnig etal (25) concluded that the increase in the net surface charge of ionizable lipids, dihexadecylphosphatidic acid (DHPA), induces a tilt in lipid aliphatic chain based on X-ray diffraction and Raman spectroscopy. Blume and Eible (26) explained the ΔH decrease of DHPA with increase of surface charge mainly due to the change of internal energy and van der Waals interactions of the system induced by the tilting of the hydrocarbon chains at high pH.

The effect of ionic strength of aqueous solution on the thermotropic phase behavior can be understood as the interaction between the charge groups. For example, at neutral pH, the elevation of T_m of PS bilayers by an increase in ionic strength of the bulk aqueous phase can be attributed to the increased shielding of the charged moieties of the headgroup which reduces the repulsive force between the charged groups and enhances

the packing order of lipid aliphatic chains (27). When specific binding of cations such as Ca^{2+} and Li^+ to anionic lipid bilayers occurs, there is significant elevation in T_m (28). This effect can be understood as the binding of counterion promotes closer packing of lipids by neutralization of the charged moiety in the headgroup and thus stabilizes the gel phase of the lipids. In those instances where divalent cations are bound, there may be even further promotion of lipid close packing by formation of divalent cation bridges between the polar headgroups (29).

Fluorescence in Membranes

Fluorescence methods have been widely used in the studies of membrane. This is because of the inherent sensitivity of this technique and the favorable time scale of the phenomenon of fluorescence. Fluorescence emission occurs about 10^{-8} sec (10 nsec) after light absorption which coincides with a wide range of lipid motions. In addition, there are numerous fluorescence probes available which can be used to yield very specific information on membrane properties. The fundamental aspects of fluorescence and the biochemical applications of this methodology are described exhaustively in Lakowicz's book (30). There are a few very good reviews (for example: 31, 32) which emphasize the application of fluorescence techniques to membrane systems. In this section, I start with brief introduction on the physical origins of fluorescence and then discuss a few fluorescence techniques commonly used in the study of membrane properties. Finally, we discuss a specific probe, dipyrenyl probe, on the application of the lipid properties of rotational and lateral diffusion.

The light absorption and emission can be illustrated by the famous Jablonski energy diagram (Figure 1.5) (33). After light absorption, a fluorophore is usually excited to some higher vibrational level of S_1 or S_2 state. With a few rare exceptions, molecules in the condensed phases rapidly relaxed to the lowest vibrational level of S_1 state through internal conversion. The internal conversion generally occurs in psec time scale which is much shorter than the fluorescence lifetime (~10 nsec). After the internal conversion, the fluorophore has three pathways to return to ground state. One is through radiation process to give out fluorescence. The rate of this process is essentially determined by the fluorophore structure. Temperature and solvent have little effect on the radiation rate. The second pathway is through radiationless deactivation process. The fluorophore at excited state transfers energy to solvent through thermal collision. Therefore the rate of this deactivation process is sensitive to temperature and environment in which the probe resides. In most cases that intersystem crossing is negligible, fluorescence lifetime is thus one over the summation of the radiation and radiationless rate constants. It is because the rate of radiationless deactivation process is sensitive to the probe environment that the fluorescence lifetime can be used to sense the environmental difference of the fluorophore. The third pathway is that the fluorophore in the S_1 state undergoes an intersystem crossing to the first triplet state T_1. Emission from T_1 is called phosphorescence and is shifted to longer wavelength relative to fluorescence. The lifetime of phosphorescence is normally in millisecond time scale because the transition
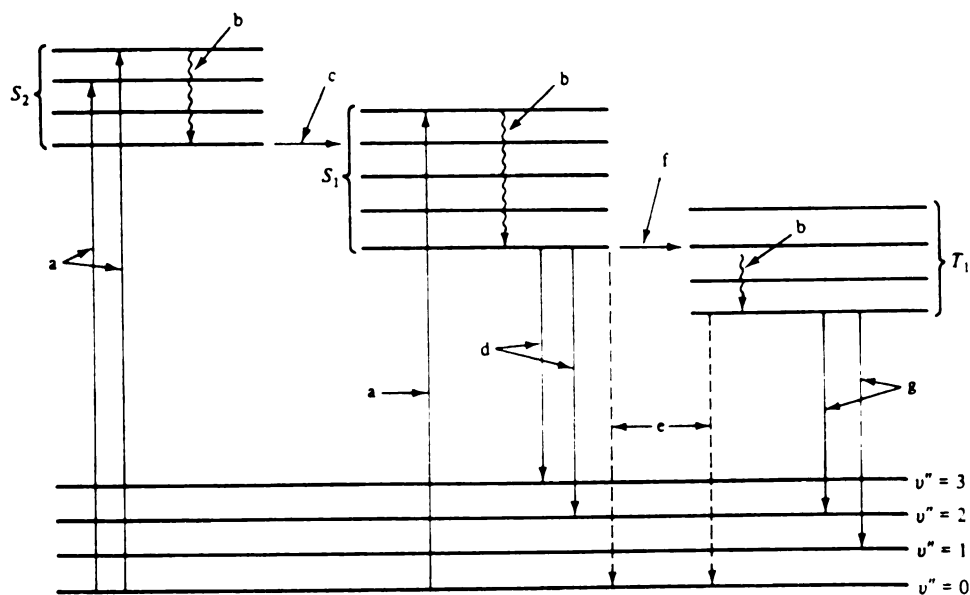
Figure 1.5. the Jablonski diagram for deactivation processes of an excited molecule. S_1 and S_2: the first and second electronic state; T_1: triplet state; v'': vibronic state; a: absorption; b: vibrational relaxation; c: internal conversion; d: fluorescence; e: external conversion; f: intersystem crossing; g: phosphorescence. Adapted from reference 33.

from T_1 to S_0 is forbidden. The very long lifetime makes the fluorophore at T_1 state vulnerable. Many other thermal processes will deactivate the molecule at T_1 state rapidly. Therefore, phosphorescence exists mostly in very low temperature and is generally negligible when discussing fluorescence phenomena at room temperature.

The fluorescence emission has three characteristics. The first one is Stokes' shift. The Stokes' shift is due to internal conversion which causes an energy loss relative to absorption. Therefore, fluorescence emission in solution phase always occurs at longer wavelength comparing to absorption spectrum. The second characteristic of fluorescence emission is the emission spectrum is independent on excitation wavelength. This is also related to the internal conversion process. The internal conversion process is much faster than fluorescent process. Upon excitation into higher electronic and vibrational levels, no mater how high the electronic or vibrational levels are, the excess energy is always quickly dissipated, leaving the fluorophore in the lowest vibrational level of S_1. The third characteristic is that fluorescence spectrum is normally a mirror image of absorption spectrum. This is so because the absorption spectrum reflects the vibrational levels of electronically excited states and fluorescence spectrum reflects the vibrational levels of the ground electronic state. Generally, electronic excitation does not alter the spacing of vibrational energy levels.

The properties of membranes commonly studied by fluorescence techniques include motional, structural and organizational aspects. Motional aspects include the rate of motion of lipid aliphatic chains, the phospholipid headgroups and other lipid

components. Organizational aspects include the distribution of lipids both laterally, in the plan of membrane such as phase separations, and across the membrane bilayer such as phospholipid asymmetry and distances from the surface or depth in the bilayer. Finally, membrane surface properties include such as surface charge and dielectric properties. Table 1.2 summarizes the fluorescence techniques which are commonly used to investigate the above-mentioned membrane properties.

Table 1.2. Common fluorescence techniques used in the study of membrane properties. Adopted from reference 31.

Membrane Property	Fluorescence techniques
Motion	
Rotational diffusion and orientation	Anisotropy
Lateral diffusion	Intensity and lifetime; quenching
Organization	
Lateral (phase separations)	Intensity and lifetime
Longitudinal (distance from surface)	Anisotropy; quenching; energy transfer
Surface density	Quenching; energy transfer
Lipid-lipid association	Quenching; energy transfer
Surface properties	
Surface charge	Intensity and lifetime
Dielectric properties	Solvent effects

Excimer formation can be considered as one type of fluorescence quenching. The monomer fluorescence intensity is reduced as a result of monomer at excited state reacting with a monomer at ground state to form an excimer which emits at lower energy level. The reaction rate depends on the fluorescence lifetime of the monomer, average distance between fluorophores and how fast the monomer at excited state diffuses around

to encounter another monomer at ground state for the reaction to occur. The excimer reaction is therefore widely used to study lateral diffusion of membranes.

Pyrene and pyrene derivatives are the most widely used fluorophores for the study of the lateral diffusion rate of lipid membranes. There are two reasons for that. First of all, fluorescence of pyrene has very high quantum yield and thus provide enough sensitivity. Secondly, excimer can be formed upon excitation and subsequent association of pyrene at excited state with pyrene at ground state. The excimer emission with very high quantum yield is red-shifted and well separated from the monomer emission (34).

The lateral diffusion is mainly determined by singly labeled pyrene probe in which pyrene is covalently attached to one end of lipid aliphatic chains. The typical example of this kind is 1-palmitoyl-2-pyrene decanoyl phosphatidylcholine (PPDPC).

Galla etal (35) incorporated this probe in artificial vesicles as well as biological membranes. They concluded that the simple excimer technique yields reliable values of lateral diffusion coefficients. They further extended that diffusion coefficients within local fluidized areas of biological membranes may be measured by this technique.

Hresko etal (36) used the same probe in small unilamellar vesicles of DPPC, DMPC and POPC under anaerobic conditions. Excimer-to-monomer fluorescence intensity ratio (E/M) was determined as a function of temperature. Based on the

observation, they found that the probe is essentially randomly distributed in pure gel and fluid phosphatidylcholine bilayers.

The PPDPC probe was used once again by Lemmetyinen etal (37). Based on tiem-dependent fluorescence methods, they found that there are two different paths for excimer formation. The first path is a diffusion-controlled excimer formation process. The second path is a static process, where the pyrene moieties are aggregated in such a way that only small rotation is required for them to attain the excimer configuration. In liquid crystalline phase, the diffusion controlled path is the major one. In the gel phase, however, the excimer is probably determined solely by rotational process. This is understandable since lateral diffusion in gel phase is essentially zero.

Pyrene can also be covalently attached to both ends of aliphatic chains. In this case, the excimer is formed intramolecularly (a pseudo-monomolecular reaction) instead of intermolecularly (a bimolecular reaction). The intramolecular excimer formation depends primarily on the closeness and relative orientation of the two pryene moieties within the same molecule. A conceptual vision to explain the excimer formation is that two pyrene moieties at end of lipid chains come together first through translational diffusion and reorient themselves to a suitable conformation for the excimer formation through rotational diffusion (38, 39). The most commonly used dipyrenyl probe is di(1'-pyrenedecanoyl)-phosphatidylcholine (dipy$_{10}$PC). Vauhkonen etal (40) and Sassaroli etal (41) utilized the probe in four types of multilamellar vesicles (MLVs). Their results showed that the excimer-to-monomer ratio (E/M) is sensitive to membrane phase

transition initiated by both temperature and pressure. The free volume model, which is used to treat the problem of self-diffusion in liquid solution and two-dimensional diffusion in lipid bilayers, can describe the pressure and temperature dependence of intramolecular excimer formation rate. This results indicates that some hydrodynamic properties are common in isotropic system (i.e. liquid solution) and anisotropic system (i.e. lipid membranes) since the same hydrodynamic model can be utilized to describe the hydrodynamic behaviors of both systems. Their results also indicate that the rotation of the pyrene moiety is the rate-limiting step for intramolecular excimer formation.

In contrast to the conventional Birks' 2-state model (34) for intermolecular excimer reaction in which every collision between pyrene at excited state and pyrene at ground state results in excimer formation, Cheng etal (38, 39) proposed a 3-state model as shown in Figure 1.6.

The 3-state model suggests that the existence of three excited species of pyrene derivatives, monomer M^*, aggregated state A^* and excimer D^*. The pyrene moieties form an aggregated state through translational diffusion. The corresponding reaction constants K_{am} and K_{ma} are therefore closely related to the translational diffusion rate. In the excited aggregated state A^*, the two pyrene moieties are in close apposition and an elementary change in relative orientation of pyrene moieties might result in intramolecular excimer D^* formation. The corresponding rate constants K_{da} and K_{ad} are thus related to rotational diffusion rate. Birks' 2-state model only considers the excimer formation and ignores how the excimer is formed. The 3-state model separates the two types of diffusion rates

3-State Model
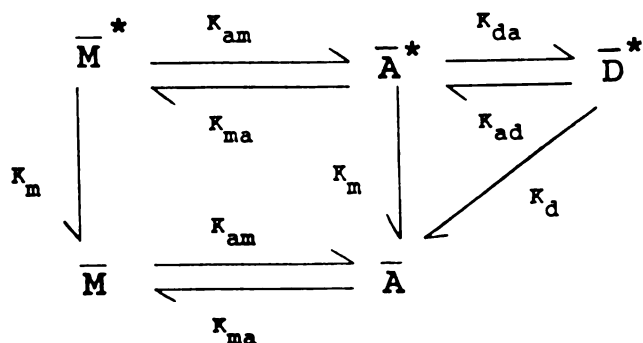
2-State Model
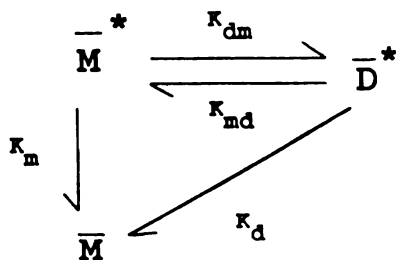
Figure 1.6. Schematic diagrams of the 2- and 3-state kinetic models of dipyrenyl membrane probe. K_{dm}: excimer association rate; K_{dm}: excimer dissociation rate; K_m: monomer decay rate; K_d: excimer decay rate; K_{am}: aggregate association rate; K_{ma}: aggregate dissociation rate; K_{da}: excimer formation rate from aggregate state; K_{ad}: excimer association rate to aggregate state. Adapted from reference 38.

and thus provides a clear conceptual vision on how the intramolecular excimer is formed. One thing worthy to note is that the Birks' 2-state model is adequate to describe the excimer formation especially intermolecular excimer formation because the time required for rotational diffusion is much less than the molecular diffusing together through translation diffusion, which also explains that intermolecular excimer formation is diffusion-controlled reaction and the rate for excimer formation is equal to the molecular collision rate (42). Even though the 3-state model is very informative on physical concept, the use of this model requires extensive analysis of time-resolved data. The curve fitting involves so many variables, which usually generates huge data uncertainties.

Reaction Dynamics in Solution Phase

1. Transition State theory (TST)

The earliest theory for chemical reactions in solution is the transition state theory. The transition state is identified with an imaginary "dividing surface" separating the reactant and product state in the configuration space. For a one-dimensional potential surface, the transition state is usually chosen to be the state with the maximum energy in the barrier region. The general expression (43) for the transition state rate constant can be given by:

$$k_{TST} = \frac{k_B T}{h} \frac{Q_+}{Q_R Q_R} \exp(-E_0 / k_B T) \qquad (1.2)$$

where Q_+, Q_R and Q_P are the canonical partition functions of activated complex, the reactant and the product, respectively. k_B is the Boltzmann constant, h is the Planck constant and T is the temperature. E_0 is the intrinsic activation energy. In the solution phase, the Equation 1.2 can be rewritten:

$$k_{TST} = \frac{\omega_R}{2\pi} \exp(-E_0 / k_B T) \qquad (1.3)$$

where ω_R is the vibrational frequency of molecule in the reactant well.

The basic assumption in TST is that once the reacting system crosses the transition state, it never returns back to product side of dividing surface. The rate constant is therefore proportional to the total flux of trajectories from reactant to product side of the dividing surface. However, this assumption breaks down in solution phase. The frictional force exerted by solvent molecules induce recrossing of the trajectories and reduce the rate below the TST result.

2. Kramers' Theory

In order to study the effects of frictional forces on the rate of chemical reaction in solution, Kramers (44) modeled the reactive motion as the passage of a Brownian particle over a one-dimensional potential barrier. Kramers assumed that the motion along the reaction coordinate is given by the following ordinary Langevin equation:

$$\mu\frac{dv}{dt} = F(x) - \zeta v(t) + f(t) \qquad (1.4)$$

where μ is the effective mass, v is the velocity along the reaction coordinate, $F(x)$ is the force arising from the potential in the barrier region, ζ is the zero-frequency friction parameter and $f(t)$ is the delta-correlated Gaussian white noise. ζ and $f(t)$ are correlated by the fluctuation dissipation theorem (45):

$$< f(0)f(t) >= k_B T \zeta \delta(t) \qquad (1.5)$$

$F(x)$ is assumed to arise from a static potential which is an inverted parabola in the barrier region with imaginary frequency ω_b:

$$F(x) = \mu\omega_b^2 x \qquad (1.6)$$

After solving the stationary solutions of the Fokker-Planck equation, Kramers obtained the following simple and elegant equation for the reaction rate constant:

$$k = \frac{\omega_R}{2\pi\omega_b} \times [(\frac{\zeta^2}{4} + \omega_b^2)^{1/2} - \frac{\zeta}{2}]\exp(-E_0 / k_B T) \qquad (1.7)$$

This equation has two limiting cases. If the barrier frequency ω_b is much larger than the frequency parameter ζ, Equation 1.7 can be reduced to Equation 1.3, the rate constant of transition state theory. Another limiting case is when $\zeta \gg 2\omega_b$:

$$k = \frac{\omega_R \omega_b}{2\pi\zeta} \exp(-E_0 / k_B T) \tag{1.8}$$

The rate constant is inversely proportional to the friction parameter. This limit is called the Smoluchowski limit (46).

The two limits can be understood from simple physical reasoning. If the barrier is very sharp, then the particle spends too short time on the barrier top to feel the frictional forces. The solvent friction has no effect on the reaction rate, the transition state result (Equation 1.3). On the other hand, if the barrier top is flat, then the motion is diffusive on the barrier top. The reactive rate is thus inversely proportional to the friction that the solvent exerts on the reaction.

3. Skinner-Wolynes Theory

In Kramers theory, the reactant is treated as a Brownian particle. In many realistic situations, however, the size of reactive molecule is comparable to that of solvent molecules. Kramers theory is thus broken down. Skinner and Wolynes (47, 48) adopted a different stochastic approach to the dynamics of chemical reactions in solution. They used the BGK collision model (49, 50), which is considered to yield the best description

when solute and solvent molecular masses are comparable. The potential surface was assumed to be symmetric, i.e. the frequency at the reactant well is same as the imaginary frequency at the barrier top. The rate constant for barrier crossing can then be calculated from the expression:

$$k_{SW} = \frac{2\pi g}{\omega} [1 + \frac{\pi g}{\omega} + \frac{(2\pi g)^2}{2\pi \omega^2}]^{-1} k_{TST} \qquad (1.9)$$

where k_{TST} is the transition state theory rate constant (Equation 1.3) and g is the average collision frequency, which is related to the friction coefficient ζ and the moment of inertia μ of the reactive molecule in the form of

$$g = \frac{\zeta}{\mu} \qquad (1.10)$$

In order to obtain an expression for the rate constant which is related to experimental parameters such as solvent viscosity η, the collision frequency is expressed in terms of a hydrodynamic expression, i.e. $g \propto \eta$. Thus,

$$k_{SW} = \frac{4\pi A \eta}{B} (1 + \frac{2\pi \eta}{B} + \frac{8\pi \eta^2}{B^2})^{-1} \exp(-E_0 / k_B T) \qquad (1.11)$$

The viscosity dependence of the rate constant is through the factor

$$f_{sw}(\eta) = \frac{4\pi\eta}{B}(1 + \frac{2\pi\eta}{B} + \frac{8\pi\eta^2}{B^2})^{-1}$$ (1.12)

where $A = \omega/2\pi$ and $B/\eta = 2\omega/g$.

4. Grote-Hynes Theory

Kramers theory adopted an ordinary Langevin equation (Equation 1.4) which uses an adiabatic approximation. The adiabatic approximation is only true when the imaginary frequency ω_b at barrier top (saddle crossing frequency) is much less than the solvent bath correlation frequency (ζ/μ). The solvent molecules in this situation can adjust themselves rapidly in the time scale of the reactive molecular motion so that the reactive molecule can feel all of the solvent molecular motions. The friction used in the Kramers theory is thus zero-frequency friction constant. However, the adiabatic approximation is not always true. In fact, the saddle crossing is often nonadiabatic. The saddle crossing frequency ω_b is often comparable to or bigger than the solvent bath correlation frequency. Therefore, the reactive step occurs before the solvent can totally adjust. The reactive motion can only feel part of solvent molecular motions. The friction that the reactive motion experienced is therefore reactive frequency dependent.

Grote and Hynes (51) used the above reasoning and assumed the following generalized Langevin equation (GLE) for the dynamics along the reaction coordinate:

$$\mu\frac{dv}{dt} = F(x) - \int_0^t d\tau\zeta(\tau)v(t-\tau) + f(t) \tag{1.13}$$

By comparing Equation (1.13) with Equation (1.4), the difference is the frequency dependent friction $\zeta(t)$ which can be related to Gaussion random force f(t) by the fluctuation dissipation theorem:

$$\zeta(t) = <f(0)f(t)>/k_B T \tag{1.14}$$

As with the Kramers theory, the systematic force F(x) is one-dimensional. In the barrier region, it is given by:

$$F(x) = \mu\omega_B x^2 \tag{1.15}$$

From the GLE, Grote and Hynes derived a generalized Fokker-Planck equation and obtained the following expression for rate constant:

$$k = k_{TST}(\lambda_r / \omega_b) \tag{1.16}$$

where k_{TST} is the transition state rate constant given by Equation (1.3). λ_r is the reactive frequency given by the following self-consistent relation:

$$\lambda_r = \frac{\omega_b^2}{\lambda_r + \hat{\zeta}(\lambda_r)/\mu} \qquad (1.17)$$

where $\hat{\zeta}(p)$ is the Laplace transform of the time dependent friction

$$\hat{\zeta}(p) = \int_0^\infty dt \exp(-pt)\zeta(t) \qquad (1.18)$$

For very week friction, λ_r is approximately equal to ω_b. Grote-Hynes rate constant

(Equation 1.16) collapses to transition state rate constant. For low barrier frequency, ω_b is

so small that $\hat{\zeta}(\lambda_r)$ can be replaced by $\hat{\zeta}(0)$ in Equation 1.17. The friction is zero-

frequency friction constant which corresponds to Kramers theory. Therefore, the Kramers

theory and transition state theory can be considered as two extreme cases of Grote-Hynes

theory.

5. The Multidimensional Expansion of Reaction Dynamics Theory in Solution Phase

The aforementioned theories assume that there is only one reactive mode along

the reaction coordinate. Those theories are therefore one-dimensional. In reality,

however, most of the reactive molecules may have many non-reactive modes besides the

reactive mode. In gas phase, these modes are orthogonal to each other. They are thus

called normal modes. Normal modes are uncoupled and independent. In solution phase,

due to solvent interactions, the reactive and non-reactive modes are usually dynamically

coupled. The non-reactive modes will, therefore, have fundamental impact to the reaction rate constant. Grote and Hynes (52) discussed the reactive modes in condensed phase reactions and expanded the theory they developed to multidimensional space.

A. Multidimensional expansion of transition state theory

In TST, the modes are uncoupled. With the normal mode separability assumption, the saddle region reaction system Hamiltonian is thus separable:

$$H_s = H_r + H_n \tag{1.19}$$

where H_s, H_r and H_n are the Hamiltonian in saddle region, Hamiltonian of reaction mode and the Hamiltonian of the sum of uncoupled non-reactive normal modes, respectively.

By solving Schrodinger equation corresponding to the H_s, the reaction rate constant can be obtained as the following expression:

$$k_{TST} = [\prod_{i \in n} (\frac{\omega_{Ri}}{\omega_i})](\frac{\omega_R}{2\pi}) \exp(-\Delta U / k_B T) \tag{1.20}$$

where ω_{Ri} and ω_i are the non-reactive mode frequency at reactant well and saddle region, respectively. The prefactor product of frequency ratios is related to entropy ΔS from reactant well surface to saddle surface: (53)

$$\prod_{i \in I} (\frac{\omega_{Ri}}{\omega_i}) = \exp(\Delta S / k_B) \qquad (1.21)$$

Therefore,

$$k_{TST} = \frac{\omega_R}{2\pi} \exp(-\Delta G / k_B T) \qquad (1.22)$$

with the total free energy of activation $\Delta G = \Delta U - T\Delta S$. This expression (Equation 1.22) is same as the one-dimensional one but the magnitude may be different due to the entropy term.

B. Multidimensional expansion of Grote-Hynes theory: uncoupled modes

Grote and Hynes assumed that reactive and non-reactive modes are governed by generalized Langevin equation (GLE):

$$\mu \frac{dv_r}{dt} = F_r(x) - \int_0^t d\tau \zeta_r(\tau) v_r(t-\tau) + f_r(t) \qquad (1.23)$$

$$\mu \frac{dv_i}{dt} = F_i(x) - \int_0^t d\tau \zeta_i(\tau) v_i(t-\tau) + f_i(t) \qquad (1.24)$$

where subscript r represents the reactive mode and i the non-reactive modes. The rate constant corresponding to the GLE can be derived as:

$$k = [\prod_{i \in I} (\frac{\omega_{Ri}}{\omega_i})]\exp(-\Delta U / k_B T)(\lambda_r / \omega_r)$$

$$= [\prod_{i \in I} (\frac{\omega_{Ri}}{\omega_i})] \times k_r \qquad (1.25)$$

Similar to the multidimensional expansion of TST, the effect of uncoupled reactive modes to the final rate constant is included in the prefactor product of frequency ratios. Therefore, Equation 1.25 can be further reduced to:

$$k = k_{TST}(\lambda_r / \omega_r) \qquad (1.26)$$

where λ_r is the reactive frequency with the same self-consistent relation as Equation 1.17, ω_r is the reactive mode frequency in the saddle region. Again, the reaction rate constant of uncoupled multidimensional expansion has the same expression as the one-dimensional Grote-Hynes theory (Equation 1.16)

C. Multidimensional expansion of Grote-Hynes theory: coupled modes

The GLE of mode coupling to between reactive mode and non-reactive mode can be expressed by:

$$\mu\frac{dv_r}{dt} = F_r(x) - \int_0^t d\tau \zeta_r(\tau)v_r(t-\tau) + \sum_{i \in I}\int_0^t d\tau \zeta_{ri}(\tau)v_r(t-\tau) + f_r(t) \qquad (1.27)$$

32

In a similar manner, the GLE of mode coupling between non-reactive mode:

$$\mu \frac{dv_i}{dt} = F_i(x) - \int_0^t d\tau \zeta_i(\tau) v_i(t-\tau) + \sum_{i \neq j} \int_0^t d\tau \zeta_{ij}(\tau) v_j(t-\tau) + f_i(t) \qquad (1.28)$$

The additional summation terms are due to mode coupling between reactive mode (r) and non-reactive mode (i) (Equation 1.27) and coupling between the non-reactive modes (Equation 1.28).

The final rate constant has the same expression as Equation 1.26, the multidimensional expansion without mode coupling. The sole, but essential, difference is that the reactive frequency carries the information that reactive mode is dynamically coupled to the remaining modes. The effective friction

$$\zeta_r(t) = \zeta_{rr}(t) + \zeta_{rn}(t) \qquad (1.29)$$

is composed of the direct friction $\zeta_{rr}(t)$ on the reactive mode and the friction $\zeta_{rn}(t)$ arising from the dynamical coupling to all of the non-reactive modes.

References

1. Singer, S. J.; Nicholson, G. L. *Science* **1972**, 175, 720

2. Welti, R.; Glaser, M. *Chem. Phys. Lipids* **1994**, 73, 121

3. McConnell, H. M. *Annu. Rev. Phys. Chem.* **1991**, 42, 171

4. Möhwald, H. *Annu. Rev. Phys. Chem.* **1990**, 57, 669

5. Miller, A.; Möhwald, H. *J. Chem. Phys.* **1987**, 86, 4258

6. Lösche, M; Duwe, H.-P.; Möhwald, H. *J. Coll. Interf. Sci.* **1988**, 126, 432

7. Seul, M.; Eisenberger, P.; McConnell, H. M. *Proc. Natl. Acad. Sci. USA* **1983**, 80, 5795

8. Weis, R. M.; McConnell, H. M. *Nature* **1984**, 310, 47

9. Silvius, J. R. in *Lipid-Protein Interactions* edited by Jost, P. C. and Griffith, O. H.; vol. 2, Wiley Interscience: NY, PP.239-281, 1981

10. Vaz, W. L. C.; Melo, E. C. C.; Thompson, T. E. *Biophys. J.* **1989**, 56, 869

11. Vaz, W. L. C.; Melo, E. C. C.; Thompson, T. E. *Biophys. J.* **1990**, 58, 273

12. Bultmann, T.; Vaz, W. L. C.; Melo, E. C. C.; Sisk, R. B.; Thompson, T. E. *Biochemistry.* **1991**, 30, 5573

13. Almeida, P. F. F.; Vaz, W. L. C.; Thompson, T. E. *Biochemistry* **1992**, 31, 7198

14. Graham, I.; Gagne, J.; Silvius, J. R. *Biochemistry* **1985**, 24, 7123

15. Hartmann, W.; Galla, H.-J.; Sackmann, E. *FEBS Lett.* **1977**, 78, 169

16. Haverstick, D. M.; Glaser, M. *Proc. Natl. Acad. Sci. USA* **1987**, 84, 4475

17. Rodgers, W.; Glaser, M. *Proc. Natl. Acad. Sci. USA* **1991**, 88, 1364

18. Stryer, L. *Biochemistry,* 4th ed.; Freeman and Company: New York; chapter 11

19. Israelachvili, J. N.; Marcelja, S.; Horn, R. G. *Q. Rev. Biophys.* **1980**, 13, 121

20. Lewis, R. N. A. H.; McElhaney, R. N. in *the structures of Biological Membranes* (Ed. Yeagle, P.) **1992**, CRC Press: Boca Raton, Florida, Ch. 2

21. Jacobson, K.; Papahadjopoulos, D. *Biochemistry* **1975**, 14, 152

22. Träuble, H.; Eibl, H. *Proc. Nat. Acad. Sci. USA* **1974,** 71, 214

23. Träuble, H.; Teubner, M.; Woolley, P.; Eibl, H. *Biophys. Chem.* **1976,** 4, 319

24. MacDonald, R. C.; Simon, S. A.; Baer, E. *Biochemistry* **1976**, 15, 885

25. Jähnig, F.; Harlos, K.; Vogel H.; Eibl, H. *Biochemistry*, **1979**, 18, 1459

26. Blume, A.; Eibl, H. *Biochim. Biophys. Acta* **1979**, 558, 13

27. Cevc, G.; Watts, A.; Marsh, D. *Biochemistry* **1981,** 20, 4955

28. Demel, R. A.; Paltauf, F.; Hauser, H. *Biochemistry* **1987**, 26, 8659

29. Feigenson, G. W. *Biochemistry* **1986,** 25, 5819

30. Lakowicz, J. R. *Principles of Fluorescence Spectroscopy* Plenum Press: New York and London, 1983

31. Stubbs, C. D.; Williams, B. D. *Fluorescence in Membrane* chapter 5; in *Topics in Fluorescence Spectroscopy;* Lakowicz, J. R. (ed.); Plenum Press: New York, 1992

32. Azzi, A. *Quart. Rev. Biophys.* **1975,** 8, 237

33. Ingle, J. D.; Crouch, S. R. *Spectrochemical Analysis* **1988**; Prentice Hall: Englewood Cliffs, N. J.; Chapter 12

34. Birks, J. B. *Photophysics of Aromatic Molecules;* Wiley Interscience: New York, 1970; Chapter 7

35. Galla, H.-J.; Hartmann, W.; Theilen, U.; Sackmann, E. *J. Membr. Biol.* **1979,** 48, 215

36. Hresko, R. C.; Sugar, I. P.; Barenholz, Y.; Thompson, T. E. *Biochemistry* **1986**, 25, 3813

37. Lemmetyinen, H.; Yliperttula, M.; Mikkola, J.; Virtanen, J. A.; Kinnunen, P. K. J. *J. Phys. Chem.* **1989,** 93, 7170

38. Cheng, K. H.; Ruymgaart, L.; Liu, L.-I.; Somerharju, P.; Sugar, I. P. *Biophys. J.* **1994,** 67, 902

39. Cheng, K. H.; Ruymgaart, L.; Liu, L.-I.; Somerharju, P.; Sugar, I. P. *Biophys. J.* **1994,** 67, 914

40. Vauhkonen, M.; Sassaroli, M.; Somerharju, P.; Eisinger, J. *Biophys. J.* **1990,** 57, 291

41. Sassaroli, M.; Vauhkonen, M.; Somerharju, P.; Scarlata, S. *Biophys. J.* **1993,** 64, 137

42. Birks, J. B.; Lumb, M. D.; Munro, I. H. *Proc. Roy. Soc. A,* **1964,** 280, 289

43. Laidler, K, *Theories of Chemical Reactions Rates* McGraw Hill: New York; 1969; Ch. 3

44. Kramers, H. A. *Physica* **1940,** 7, 284

45. Kubo, R. *Rep. Prog. Phys.* **1966,** 29, 255

46. Smoluchowski, M. V. *Z. Phys. Chem.* **1917,** 92, 129

47. Skinner, J. L.; Wolynes, P. G. *J. Chem. Phys.* **1978,** 69, 2143

48. Skinner, J. L.; Wolynes, P. G. *J. Chem. Phys.* **1980,** 72, 4913

49. Bohm, D.; Gross, E. P. *Phys. Rev.* **1949,** 75, 1864

50. Bhatnagar, P. L.; Gross, E. P.; Krook, M. *Phys. Rev.* **1954,** 94, 511

51. Grote, R. F.; Hynes, J. T. *J. Chem. Phys.* **1980,** 73, 2715

52. Grote, R. F.; Hynes, J. T. *J. Chem. Phys.* **1981,** 74, 4465

53. Vineyard, G. H. *J. Phys. Chem. Solids* **1957,** 3, 121

Chapter 2

Instrumentation Description

Lipid membrane is a very complex system. The properties of the membrane are governed by many factors. In this thesis, two of them, spatial alignment and motional dynamics, are of our particular interests. The instruments used to extract the two types of information are laser scanning microscopy to observe lipid spatial domain structures, spectrofluorometer and differential scanning calorimeter (DSC) to study lipid chain motional dynamics. In this chapter, I will describe the three instruments in detail.

I.   Laser Scanning Microscopy

The microscope used in this thesis research is Zeiss LSM 210 Laser Scanning Microscope (LSM) (Carl Zeiss, Thornwood, NY). It can be operated in either "conventional" mode or laser scanning mode. Table 2.1 lists the comparison of the two operational modes.

Table 2.1. the comparison between two operational modes in Zeiss LSM 210.

Operation Modes	Conventional	Laser Scanning
Light Sources	(1) tungsten (2) mercury	(1) dual line argon ion laser (2) He-Ne laser
Signal Detector	Human eyes	PMT or silicon diode
Signal Type	Analog	Digital after A/D converter
Signal Recording	Camera	Computer disk
Confocal option	No	Yes

In laser scanning mode, the images are digitized into pixels after an analog-to-digital converter and saved on computer disks. The digital form of signal enables users to further process (e.g.: edge enhance filter) and manipulate (e.g.: 3-D image reconstruction) the images. In addition, the laser scanning microscope has a confocal option which offers

many special features over microscopes without a confocal unit. Both the digital signal and the confocal option in laser scanning modes make the laser scanning microscope far more versatile and powerful than the conventional light microscope.

In the following, I will be branching into a few subsections detailing the light microscopic techniques I have used to acquire data in Chapter 3 and 7. There are many good books describing the basic principles and applications of the light microscopy. Two of them, one discussing the light microscopy in general (1) and another one confocal laser scanning microscopy in particular (2), have been used extensively in this section.

1. Imaging Modes

The Laser Scanning Microscope (LSM) offers three types of images: transmission, reflection and fluorescence. The transmission image can be further divided into four types: brightfield (based on light absorbance of the specimen), darkfield (by inserting an opaque stop in the microscope condenser so that only light that scattered or reflected by the specimen enters the objective or detector), phase contrast (to convert light phase difference into light intensity variation) and polarization (to observe the specimen with birefringent materials). The reflection and fluorescence images have confocal options while transmission image is not confocal. Three imaging modes: phase contrast, polarization and confocal reflection (Image is obtained by collecting light reflected from specimen surface while a confocal unit is placed in the light path), were routinely used in this thesis research and will be described in detail. The confocal option

is a unique and powerful feature of this microscope and a full section on this feature will follow.

Reflection microscopy detects the light reflected from the specimen surface. Therefore, the light source and detector must be on the same side of the specimen. After hitting the specimen, the light may scatter in any direction above the specimen, but only the photons passing through the objective lens contribute to the image. The wavelength of the light remains the same after the radiation is reflected from the specimen surface (Raman scattering negligible). In this thesis, reflection microscopy is utilized to visualize the lipid membrane surface fluctuations. For well-aligned lipid multilayers, the surface is uniaxial and smooth. No reflection structures can be observed even though the surface does reflect light. For lipid multilayers aligned with defects, that is, the lipids aligned at some angles with respect to membrane normal, the membrane surface will fluctuate in order to keep lipid bilayer spacing constant. Light will be reflected differently at different region, which, in turn, gives reflection structures or images.

Both polarization mode and phase contrast mode belong to transmission microscopy in which light passes through the specimen and is detected by a detector on the other side. In a conventional light microscope, light comes from below the specimen and is perceived by an observer looking through the oculars. For laser scanning operation in this LSM, light comes from the above specimen and detected by a silicon diode detector located in the microscope base. The difference between polarization and phase contrast is manifested by the light modification.

In conventional polarization microscopy, polarized light is generated by placing a polarizer in the light path above the specimen and a rotating analyzer below the specimen. The polarizer and analyzer are in a crossed position. In laser scanning mode of this LSM, the light from argon ion laser itself is polarized. Therefore, only an analyzer is necessary to perform polarized imaging. If the specimen doesn't polarize light, that is, the material in the specimen doesn't have birefrigence, the light passing through a polarizer will be extinguished by an analyzer. However, if the materials in the specimens do polarize light, a bright image will be obtained against a dark background. In this thesis, the specimen is lipid multilayers. Whether the multilayers are birefringent or not depends on the lipid alignment. For well-aligned multilayers, lipid optical axis is along the light propagating direction. Birefringence is not generated. A dark image is thus obtained under polarization mode. However, if the multilayers are aligned with defects (i.e.: lipid optical axis is at some angle with respect to light propagating direction), the lipid optical axis in those regions is no longer parallel to the light propagating direction. Birefringence is produced in the defect region. The defect structures can be observed under polarization microscope. The defect domain here is the optical microscope detectable macrodomain with domain size in the μm scale.

Phase contrast microscopy works by converting light phase difference which can not be sensed by the human eye into amplitude difference which can be perceived as varying intensities. The phase difference is generated due to refractive index difference at different regions in the specimen. The physical principle for converting the phase to

amplitude is through interference. When two rays in phase are combined, constructive interference occurs, which results in an increased amplitude or brightness. Conversely, if the two rays are out of phase, destructive interference occurs and consequently, brightness will be decreased. In polarization microscopy, the polarized image is obtained by inserting a polarizer above the specimen and an analyzer below the specimen. Similarly, phase contrast is realized by inserting a phase annulus below the specimen and a phase plate above the specimen. The phase annulus is a ring inserted in the microscope condenser (Figure 2.1). Again, similar to the polarization microscope in which analyzer and polarizer are in a crossed position, the phase annulus and the phase ring in the phase plate are complementary to each other. The optical setup for phase contrast microscopy is illustrated in figure 2.1. In this thesis, phase contrast microscopy is utilized to visualize lipid multilayer structures by taking advantage of refractive index that is dependent on the lipid alignment. For well-aligned multilayers, the lipid optical axis is parallel to light propagating direction. The electric field of the radiation is always perpendicular to the lipid optical axis. The interaction between the electric field and lipids will be same. Only one refractive index is generated. There will be no refractive index difference and consequently no phase contrast structures can be observed in the specimen. However, when lipid is aligned at some angles with respect to light propagating direction, the electric field of the radiation will interact with lipids differently depending on the angle between the electric field and the lipid optical axis. A refractive index difference will be generated in this region. The defect structures will be observed by the phase contrast microscopy.
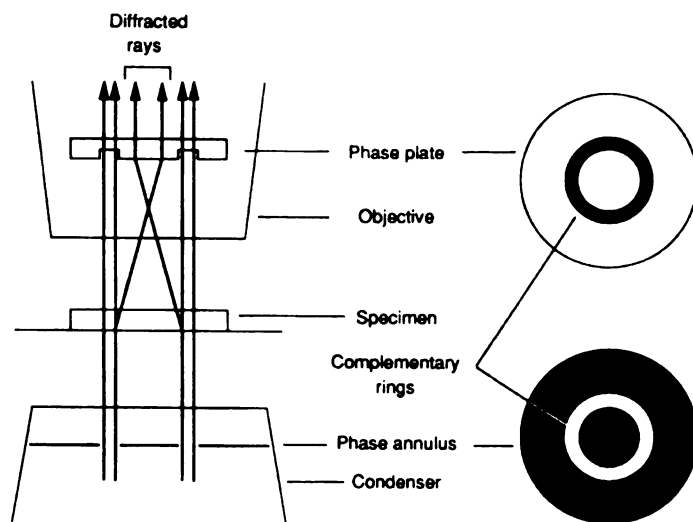
Figure 2.1 The optical elements in a phase contrast illumination system. Note the complementary rings in phase annulus and phase plate. Adapted from reference 3.

2. Confocal Imaging and its Special Applications

The major difference between confocal microscopy and conventional microscopy is that in a confocal microscope, a confocal unit with a small pinhole is placed at a strategic point in the light path as shown in figure 2.2. The pinhole is so small that it only allows the radiation from the objective's focal plane to pass through it and to be detected by the PMT detector. Out-of-focus light will be blocked by the confocal unit. Therefore, the first advantage of the confocal microscopy is that it gives a much sharper image. The image obtained from the objective's focal plane is called an optical section. Many other optical sections can be obtained by changing the focal planes. A three-dimensional image can be reconstructed by stacking many optical sections with help of computer programming. So the second advantage of the confocal microscopy is that it provides a non-intrusive way to study three-dimensional structures of an either transparent or opaque specimen.

One special type of optical sectioning is called phi-z sectioning. As shown in figure 2.3, rather than scanning in the customary horizontal plane (x-y plane), the phi-z sectioning fixes the laser beam in the x-y plane and the laser beam is then scanned repeatedly at successively deeper levels. So a cross-sectional view (x-z plane) can be observed. This feature is especially useful for layered specimens such as lipid multilayers in this thesis research. One can obtain the layer correlation through the phi-z sectioning.

Another special feature of the LSM is time series. The time series is a program which facilitates collection of images at specific time intervals. It is most commonly used
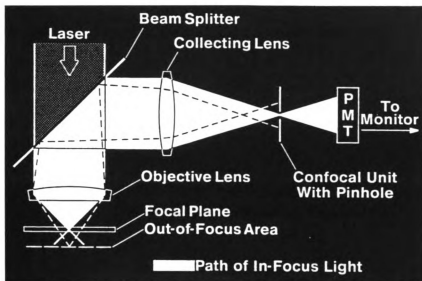
Figure 2.2. The principles of confocal imaging. The confocal unit with pinhole is put in such a special position that only the in-focus light is allowed to pass through it. Out-of-focus light represented by the dash line will be blocked by the confocal unit. Adapted from reference 2.
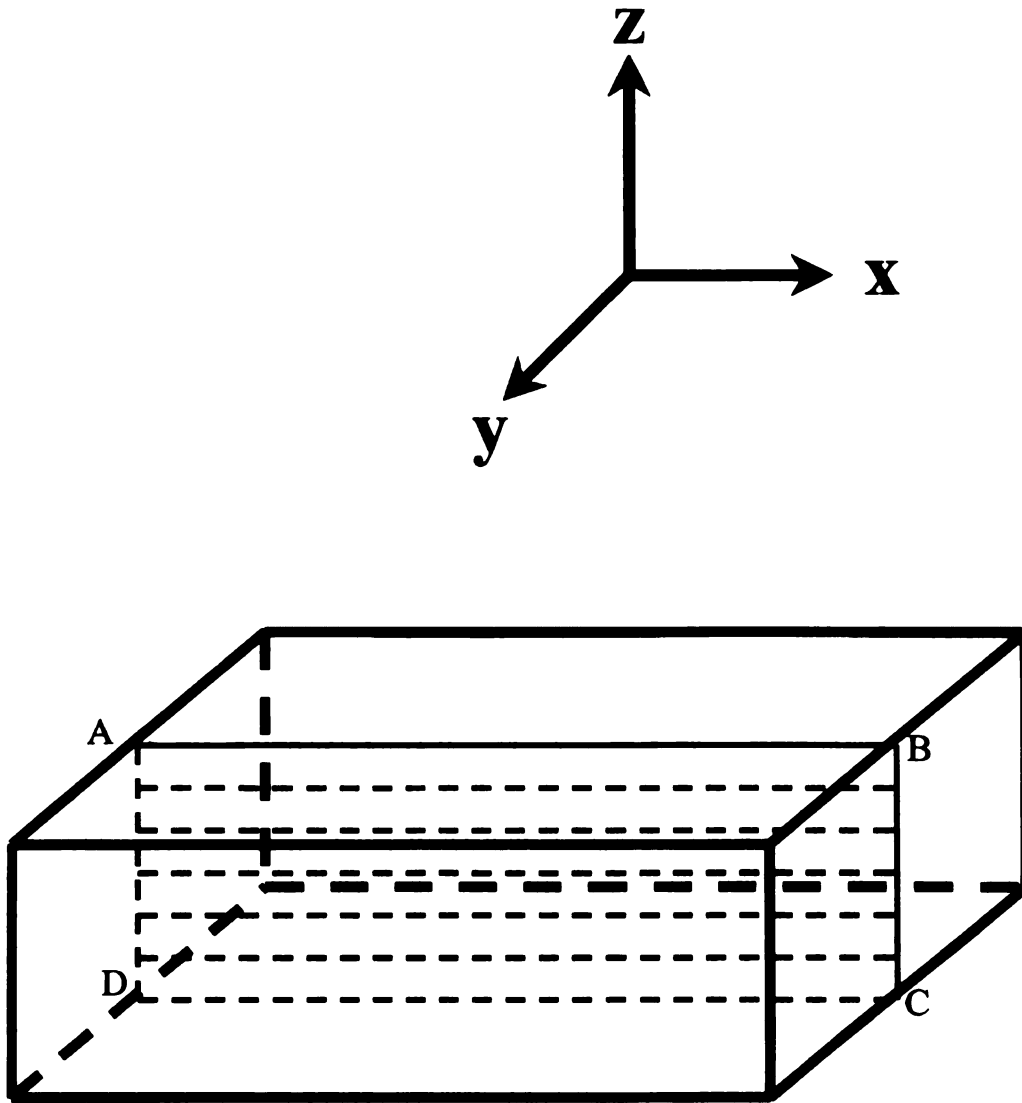
Figure 2.3. The principle of phi-z sectioning. The laser beam (AB) is fixed at xy plane and scanned deep down by changing focal length in the xz plane. A cross-sectional view of the specimen (ABCD) is thus obtained.

to visualize dynamic events such as the domain transition process under hydrodynamic flow in real time (chapter 7). The time interval between two consecutive images depends on the image size. For a 128 × 128 (in pixel size) image, the time interval is about 0.3 second; 256 × 256 image, 0.9 second; 512 × 512 image, 2 seconds.

II. Spectrofluorometer

1. The Instrument and the Operational Overview

All of the fluorescence spectra are taken in FluoroMax-2 spectrofluorometer (Instruments S. A., Edison, NJ). Figure 2.4 shows the simplified block diagram of the instrument (4). Lights from the 150W xenon lamp enters the excitation spectrometer, which delivers monochromatic light with an adjustable bandwidth to the sample compartment. Prior to reaching the sample compartment, however, 8% of the light is directed to the reference photodiode via a quartz beam splitter. Light emitted from the sample is dispersed by the emission spectrometer and directed to the signal PMT detector. This signal is then amplified and displayed on the computer monitor. The signal intensity is in the form of counts per second (CPS). The spectrofluorometer offers three measurement options: (1) emission spectra by scanning the emission monochrometer while exciting the sample with a fixed wavelength of light; (2) excitation spectra by scanning the excitation monochrometer with the emission spectrometer at a fixed wavelength and (3) synchronous spectra by scanning both spectrometers simultaneously with a fixed wavelength difference.
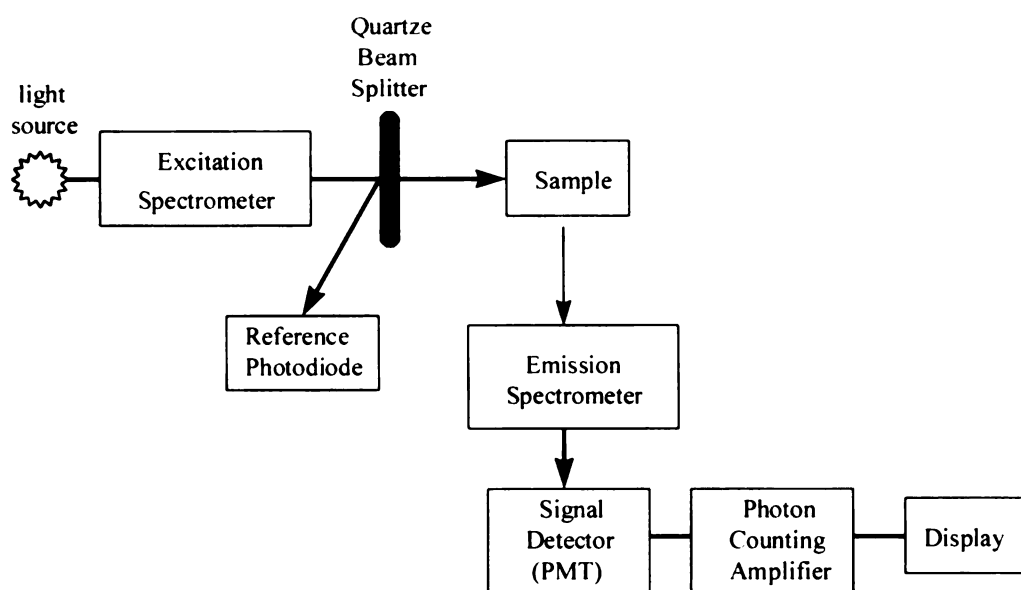
Figure 2.4. The simplified block diagram of FluoroMax-2 Spectrofluorometer.

2. The Spectrometers

The FluoroMax-2 is equipped with modofied Czerny-Turner spectrometers in both the excitation and emission positions. In each spectrometer, a grating disperses the light from 200 nm to 900 nm. The gratings in the excitation and emission spectrometers have a groove density of 1,200 grooves/mm and are blazed at 330 nm and 500 nm, respectively. The entrance and exit ports of each spectrometer have continuously adjustable (in 0.025 mm increments), computer-controlled slits. The slits of the excitation spectrometer determine the amount of light passing through the excitation spectrometer to the sample. The emission spectrometer slits control the intensity of the fluorescence signal recorded by the signal PMT detector. Adjusting slit widths select the intensity and wavelength spread (bandpass) of light. The bandpass is calculated using the equation:

$$\text{Bandpass (in nm)} = \text{slit width (in mm)} \times \text{system dispersion} \qquad (2.1)$$

The dispersion of this spectrofluorometer with groove density 1,200 grooves/mm is 4.25 nm/mm. Most of the spectra are obtained with bandpass 1 nm of both excitation and emission after considering the requirement of signal intensity and spectrum resolution.

3. Sample Compartment and Sample Cell

Light from the excitation spectrometer is focused and directed to the sample compartment. Before the light enters the sample compartment, however, a beam splitter directs 8% of the light from the excitation spectrometer to the reference phtodiode, and the remaining light continues to the sample. Fluorescence from the sample is collected

and directed to the emission spectrometer. Note that the excitation light beam is perpendicular to the fluorescence collection direction. This design is aimed at reducing the background from the strong excitation light. The light fluctuation is normally corrected by ratioing the fluorescence signal to the reference signal.

The sample cell is home-made for the purpose of degassing by freeze-pump-thaw circles as shown in figure 2.5. It consists of two parts: degassing part (A) and measurement part (B). The two parts can be connected and sealed through an O-ring and a clamp. Before degassing, sample is loaded into the container in part A. Part A and part B are then connected and sealed. Valve a and b are in close position. After the sample is frozen, open the valve a and b. Gas in the sample cell will be pumped out. Close valve a, leave valve b open and let the sample thaw. After a few of the freeze-pump-thaw circles, the sample is free of air. The solution will then be transferred from the container in part A to the quartz cell in part B. Close the valve b and then take part A and part B apart. Part B is then ready to be put into the sample compartment of the FluoroMax-2 for measurement. All of dipy samples in isotropic solvent are prepared in this way to eliminate the oxygen quenching effect. Dipy samples in lipid vesicles are not degassed for the reason explained in chapter 5. Experimental evidence has shown that oxygen quenching is negligible for dipy sample in lipid vesicles. The pyrene derivatives such as pyrene butyric acid (PBA) and dipy do not possess the symmetry that pyrene has. The quenching is thus significantly reduced.
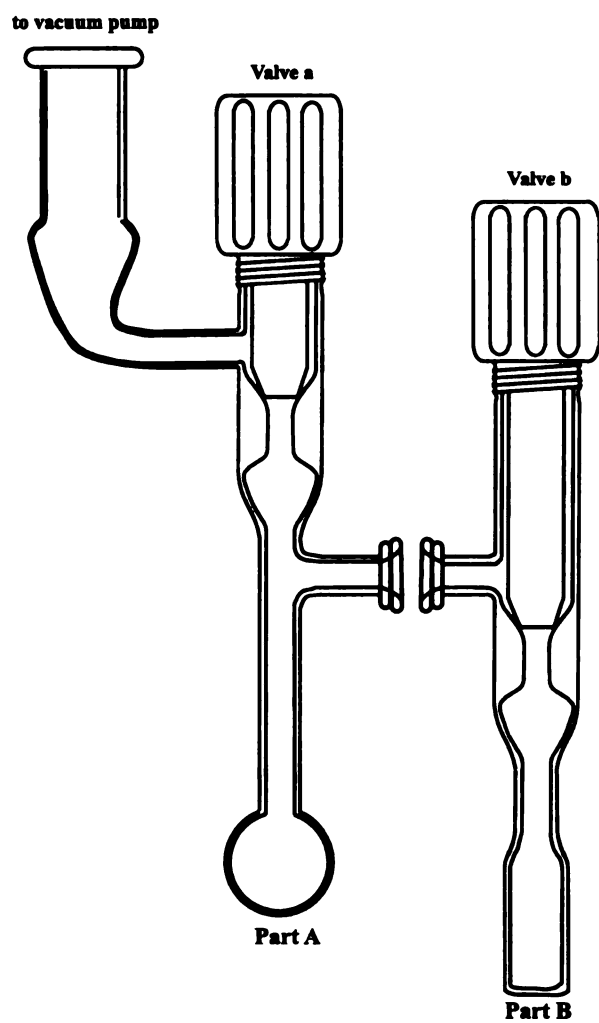
Figure 2.5. The diagram of sample cell for degassing (Part A) and fluorescence measurement (Part B).

III.   Differential Scanning Calorimeter

The phase transition temperature and enthalpy measurement on lipids were made on an MC-2 high sensitivity scanning calorimeter (Microcal, Inc., Amherst, MA). The MC-2 is a differential instrument with two cells, one for sample (cell A) and another for reference (cell B). A block diagram of the cell assembly is shown in Figure 2. 6 (5). The sample cell (A) is filled with lipid vesicles and buffer. The reference cell is filled with just buffer.

Each cell has its own heaters on its outer surface. The sample and reference cells are heated simultaneously at identical, predetermined rates. Thus the temperatures of the sample and reference cells initially increase linearly with time and the temperature difference between them is maintained at zero. If the sample (lipid vesicle in this case) undergoes a thermally induced event such as phase transition of lipid, the control system, normally a feedback heater on the cell outer surface (not shown in Figure 2.6), senses the resulting temperature differential between the sample cell and reference cell and supplies more or less heat (power) to the sample cell to hold its temperature equal to that of the reference cell. The recorded parameter in DSC measurement is thus the differential heat as a function of temperature or specific heat. If the sample does not undergo a thermal event, then the recorder should trace a straight, horizontal baseline denoting a zero differential power output. If a thermal event occurs, however, the recorder pen is deflected from the baseline, the direction of the deflection depending on whether the event is endothermic (positive deflection) or exothermic (negative deflection), and the
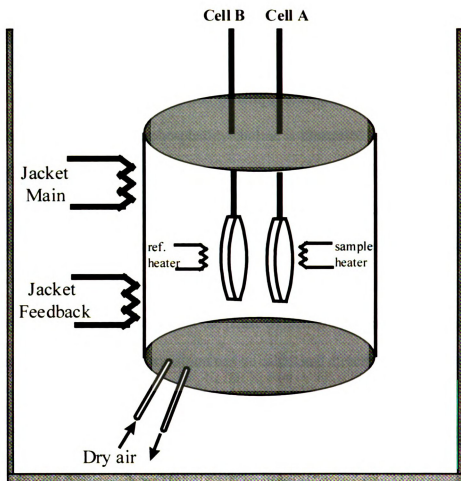
Figure 2.6. The simplified block diagram of MC-2 differential scanning calorimeter.
Modified from reference 5.

magnitude of the deflection depends on the magnitude of the differential heating rate. Upon completion of the thermal event, the recorder pen returns to the baseline or to a new baseline if a change in the specific heat of the sample has occurred.

The specific heat as function of temperature for a gel-to-liquid crystalline phase transition of a single, pure phosphatidylcholine is illustrated in figure 2.7 (6). From such a DSC trace, a number of important parameters can be determined directly. The phase transition temperature, T_m, is that temperature at which the excess specific heat reaches a maximum. The peak area under the DSC trace, when calibrated with a known standard, is direct measurement of the phase transition enthalpy, ΔH_{cal}. Since the change in free energy ΔG of the system is zero at the phase transition midpoint temperature, the entropy change associated with the transition can be calculated directly from the equation:

$$\Delta S = \Delta H_{cal}/T_m \qquad (2.2)$$

Another thermal parameter, the van't Hoff enthalpy ΔH_{vH} can also be determined from the DSC trace by the following equation:

$$\Delta H_{vH} \cong 6.9\, T_m^2/\Delta T_{1\,2} \qquad (2.3)$$

where $\Delta T_{1\,2}$ is the peak width at the half peak height. From the ratio of $\Delta H_{vH}/\Delta H_{cal}$, the cooperative unit size (CUS) can be determined. The CUS is a measure of the degree of
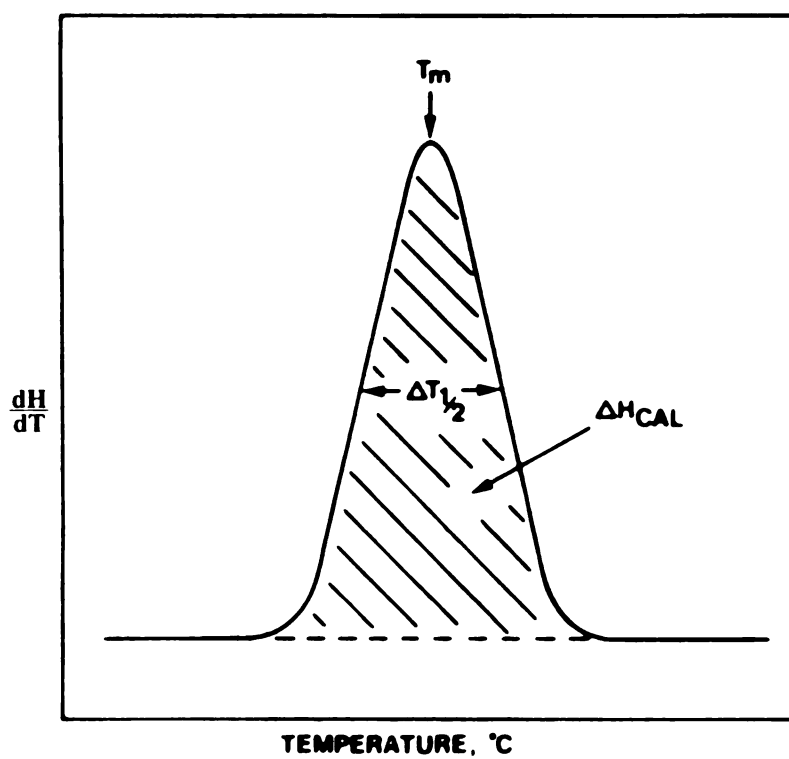
Figure 2.7. The specific heat (dH/dT) as a function of temperature for two-state endothermic phase transition. Modified from reference 6.

intermolecular cooperation between phospholipid molecules in a bilayer. For a completely cooperative, first-order phase transition of an absolutely pure substance, this ratio should approach infinity, while for a completely non-cooperative process this ratio should approach unity. Although the absolute CUS values determined should be regarded as tentative, since this parameter is markedly sensitive to the presence of impurities and may be limited by instrumental parameters, carefully determined CUS values can be useful in assessing the purity of synthetic phospholipids and in quantitating the degree of cooperativity of lipid phase transitions.

IV.   References

1. Delly, J. G. *Photography Through the Microscope* Rochester, NY: Eastman Kodak Company, 1988

2. Whallon, J. H. *Introduction to Laser Scanning Confocal Microscopy* East Lansing, MI: LSM laboratory, Michigan State University, 1993

3. Rawlins, D. J. *Light Microscopy* BIOS Scientific Publishers, 1992

4. Instrument S. A. *FluoroMax-2 Operation Manual* Edison, NJ: Instrument S. A., 1988

5. Microcal *MC-2 Operational Manual* Amherst, MA: Microcal, Inc., 1986

6. Lewis, R. N. A. H.; McElhaney, R. N. in *the structures of Biological Membranes* (Ed. Yeagle, P.), CRC Press: Boca Raton, Florida, 1992, Ch. 2

Chapter 3

Characterization of Lipid Multilayer Microphase Structures by Phase Contrast and Confocal Reflection Microscopy

Introduction

Liquid crystals are of great interests not only for their wide industrial applications but also because of their biological importance. It is well known that lipids in cell membranes, as described by the fluid mosaic model (1), are in a liquid crystalline state. This state is characterized by the high degree of short-range order or organization characteristic of solids but the lack of long-range order. As such, liquid crystals have many of the properties of liquids. The cell membrane thus has both intrinsic rigidity and fluidity. It is rigid enough to confine the contents of the cell. It is also fluid enough for molecules such as enzymes and other proteins to move around in a time scale that allows the myriad of membrane associated biochemical events to take place (2).

Egg lecithin-water mixtures form a lyotropic smectic A (L_α) liquid crystal at room temperature with alternate water layers and lipid layers. In this phase, there is orientation of the lipids in a 2-dimensional sheet as well as a higher level of supramolecular organization in which the sheets are layered on top of each other with a water layer sandwiched in between sheets. In each sheet, not all of the lecithin molecules point in the same direction. In one area, the bulk of lipid molecules might point in one direction and in another area they may orient in a different direction. Between the two areas defects (areas of abrupt change of physical properties related to order) are observed. Optical microscopy has been extensively used to characterize and analyze liquid crystals because orientations and defects in these systems generate optical anisotropy. The most commonly used optical technique for characterizing liquid crystal systems is polarized

light microscopy. This takes advantage of birefringence, a phenomenon in which the speed of light is different in the same material (3). By definition, this difference in speed means that the refractive indices differ. Because molecular orientation affects refractive indices, it is possible to discern regions in liquid crystalline with a net orientational difference by phase contrast microscopy.

In a lipid smectic A phase, the lipid bilayer spacing has to be constant because of the high elastic energy cost required to change the bilayer spacing (4, 5). As a result, the different net orientations of lipids in different regions of the layers produce bilayer surface fluctuations through bilayer bending. Lipid bilayer bending requires much less energy comparing to bilayer spacing variation (4, 5). Light reflection (due to topographical differences) will vary from area to area along with refraction (due to order-derived refractive index changes). Both reflective and phase contrast microscopy will therefore give information on variation of lipid organization. Confocal reflection microscopy has special utility because of the high resolving power of the confocal optics. In this paper, we report that a combination of phase contrast, polarization and confocal reflection microscopy can be used to fully characterize and analyze the defect structures and morphological forms common in lipid layers. These include such defects as oily streaks, parabolic focal conics and bubble and stripe domains. Through detail analysis, we found that the images obtained by phase contrast and confocal reflection microscopy are even more directly related to the proposed molecular alignment models than the images by polarizing microscopy.

There are other commonly used techniques for analyzing membrane domain structure. One of these is fluorescence microscopy. This suffers from the shortcoming that a fluorescent probe (which is perturbing) is employed. The probe will not allow the visualization of domains from which it is excluded. Several domains might be present and go undetected. The probe can also generate domains of its own giving totally erroneous information. Another technique that is increasing in popularity is Brewster angle microscopy. In this method, refractive index differences between lipid domains are exploited. The special condition in which all of the polarized light incident on a dielectric surface is transmitted (with the electric vector just emerging parallel to the substrate surface) is violated to differing extents by the differing refractive indices of the domains of a lipid layer placed over the dielectric. Differing amounts of light from domains of differing refractive index therefore reach a detector placed above the film thus allowing one to image the domains. This technique has increased in popularity and is proving to be quite general in its applicability (6-9).

Materials and Methods

1. Sample preparation

Egg lecithin was purchased from Sigma Chemical Company (St. Louis, MO) and cholesterol from Aldrich (Milwakee, WI). Both were used without further purification. Other chemicals were reagent grade. The lipid or lipid-cholesterol mixture was first dissolved in 2:1 chloroform methanol and pipeted onto microscope slides on a hot plate at ~50°C. The solvent was allowed to evaporate and the slides were placed under vacuum (~

10^{-3} torr) for about 2 hours to remove the last traces. They were then put into a closed chamber at constant temperature (~ 60°C) and 100% humidity for 4-7 days. During this period, lipids form multilamellar phases through a slow hydration process. Twenty μl of 0.01 M potassium phosphate buffer, pH = 7.00, containing 0.05 M potassium chloride and 0.02M sodium azide was dropped onto the slide and the preparation covered with a cover slip. The edges of the cover slip were sealed with silicone grease to avoid water evaporation during the experiment. The sealed specimen was then placed in the closed chamber for another day to ensure fully lipid hydration.

In order to eliminate surface impurity effects from the microscope slide or cover slip, they were first soaked in hot chromic acid for at least 4 hours and then rinsed in a stream of distilled water for at least another 4 hours. The clean slides and cover slips were used immediately to avoid contamination by dust.

All images were obtained at room temperature with a Zeiss LSM 210 laser scanning confocal microscope (Carl Zeiss, Thornwood, NY) equipped with a 488 nm Ar laser. A 40X dry lens was used unless otherwise specified.

2. Defects Visualization

For well aligned lipid multilayers, the optical axis of egg lecithin is perpendicular to the microscope slide and parallel to the light propagation direction. The electric field of the radiation is therefore always perpendicular to the optical axis (Figure 3.1a). Consequently, the interaction between lipids and the electric field is the same in any

direction of the field. This gives rise to the same refractive index in any direction. The refractive index is $n_\perp$ or n_o ordinary refractive index. The images obtained under this situation are therefore black under cross polarizers. There is no phase contrast image since the refractive index is the same throughout the multilamellar phase. Because of the constant d spacing of the well aligned multilayers, the bilayer surface is flat. There is no reflection structure even though the surface does reflect light.

The situation is different, however, for multilayers aligned with defects. The optical axis is no longer parallel to the light propagating direction. Instead, lipids in defect regions tilt at different angles with respect to the light propagation direction. The extreme case is when the light propagation direction is perpendicular to the optical axis (Figure 3.1b). The electric field of the radiation can then be decomposed into two components: $E_\perp$ with a refractive index of $n_\perp = c/v_\perp$ and the $E_{//}$ with a refractive index of $n_{//} = c/v_{//}$. Here, v is the velocity of propagation. When the electric field is along the lipid chains, the interaction between it and the lipids will be stronger than the interaction when the field is perpendicular. $V_{//}$ is therefore less than $V_\perp$ and consequently, $n_{//}$ is larger than $n_\perp$. A birefringence is thus generated in the defect region.

When light passes through the birefringent liquid crystal film at an arbitrary angle between 0^0 and 90^0 with respect to the optical axis, it is divided into two components: an ordinary ray with refractive index n_o and extraordinary ray with refractive index n_e (Figure 3.1c). The ordinary value n_o is always equal to $n_\perp$ while n_e lies between $n_\perp$ and $n_{//}$

Figure 3.1. The schematic diagrams of generating birefringence or refractive index difference. (a). Light propagating direction k is parallel to lipid optical axis (OA). E-field of radiation is always perpendicular to lipid OA. No birefringence or refractive index difference is generated. (b). k is perpendicular to lipid OA. E-field can be divided into two components: parallel to OA shown as E and perpendicular to OA shown as a black dot. The light propagating speed of the two components is different due to different E-field-lipid interactions. As a result, a birefringence or a refractive index difference is generated. (c). When lipids tilt at some angle with respect to k. E-field is divided to two components, one of which (black dot) is always perpendicular to lipid OA which give rise to ordinary refractive index $n_o = n_\perp$. Another shown as E can be further divided to two components: $E_{//}$, parallel to lipid OA (aa) with speed $V_{//}$ and $E_\perp$, perpendicular to lipid OA (bb) with speed $V_\perp$. As a result, the light propagating speed V depends on the relative contribution of $V_{//}$ and $V_\perp$. The extraordinary refractive index n_e, therefore, lies in between n_o and $n_{//}$. (a) (when $V = V_{//}$) and (b) (when $V = V_\perp$) are the special cases of (c). $n_{//}$ and $V_{//}$: the refractive index and light speed respectively when E-field is parallel to lipid OA. $n_\perp$ and $V_\perp$: the refractive index and light speed when E-field is perpendicular to lipid OA.

OA

$E_∥$ $V_∥$ E $V_⊥$ $E_⊥$

k

OA

$$n_e = \frac{C}{V} \; ; \; V_∥ < V < V_⊥$$

$$n_⊥ < n_e < n_∥$$

$$n_o = n_⊥ = \frac{C}{V_⊥}$$

OA

E OA

k

OA

$$n_e^o = n_∥ = \frac{C}{V_∥}$$

$$n_o = n_⊥ = \frac{C}{V_⊥}$$

$$V_⊥ > V_∥ \longrightarrow n_o < n_e$$

OA

E

OA

k

$$n_o = n_⊥ = \frac{C}{V_⊥}$$
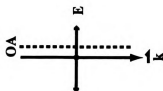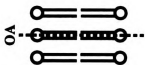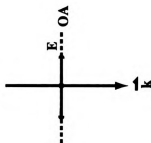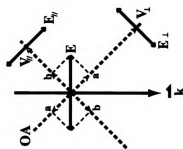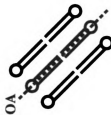
depending on the lipid orientation with respect to the light propagation direction (10). The closer to 90^0 the lipid tilting angle is, the greater the birefringence and the larger the refractive index difference. Therefore, the defect structures can be observed by both polarizing and phase contrast imaging. Because the bilayer surface fluctuates due to lipid tilting, its reflectivity will be different in different regions. The reflection images of the defects can therefore be obtained.

Results and Discussion

An egg lecithin-water mixture undergoes a gel to liquid crystalline phase transition at about -10^0C (11,12). At room temperature, egg lecithin and water form a lyotropic smectic A (L_α) liquid crystal with alternate layers of water and fluid-like phospholipid bilayers (13). Perfectly aligned multilamellar phases should be smooth, flat and uniaxial with high symmetry. In reality, however, lipids in multilamellar phases have many orientational variations in order to increase configurational entropy (14) or to relax long range stress (15). The different orderings and orientations give rise to many defect structures. The defects generally involve modifications of the lipid alignment that impact on refractive index making them discernible by phase contrast microscopy.

1. The undulation of oily streaks

Oily streaks are one of the most common defects in Smectic A liquid crystals. Figure 3.2 shows typical oily streaks by phase contrast microscopy. Note especially the undulations.

Due to edge dislocations in the lipid Smectic-A phase, the original well aligned lipid layer structure which is smooth, uniaxial and parallel to the substrate is disrupted. Lipid bilayer spacing has to be constant because of the high elastic energy cost to change the spacing. One way to keep the spacing constant in the case of edge dislocations is that the lipid layers turn around and form concentric tori centered at the edge dislocation line F and F' as shown in Figure 3.3(a).

Oily streaks can be viewed as a pair of edge dislocations. A dislocation in Smectic A phase consists of a +1/2 and −1/2 disclination. In the case of oily streaks, the distance between two −1/2 disclinations is zero, leaving two +1/2 disclinations in close contact at L and centered around two edge dislocation lines F and F'. The distance between the two dislocation lines is the amplitude of Burgers vector b (16-18). The two edge dislocation lines are not straight lines. They undulate in the microscopic viewing plane (Figure 3.3(b)), giving rise to the undulating oily streaks as shown in Figure 3.2. Thermal energy is probably responsible for the undulation since after thermally excited shape fluctuation, configurational entropy is increased (14). The width of the streaks, about 1.5 μm, corresponds to the distance between two dislocation lines, which is the amplitude of the Burgers vector. Considering the typical D spacing of egg lecithin-water mixture is 60 Å, the Burgers vector b of the undulating streaks is then approximately 250 lattice vectors.
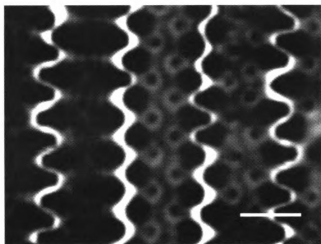
Figure 3.2. The undulation of oily streaks in an egg lecithin water mixture by phase contrast microscopy. The faint structures between the streaks are parabolic focal conics. Bar scale: 5 µm.

Figure 3.3. Established model for oily streaks. (a) The cross-sectional (x-z plane) view. The line represents one lipid bilayer surface. b is burger vector with strength of 7 in this figure. (b) paired disclination lines undulate in the x-y plane. Adapted from reference 16.
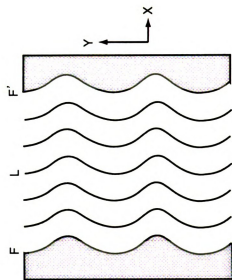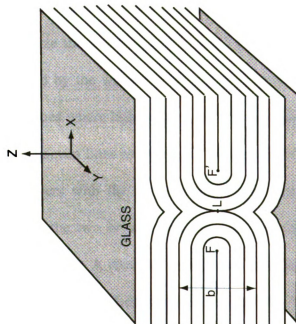
b: Burgers vector

As stated in the Materials and Methods section, only curved regions can have refractive index differences and thus generate phase contrast images. The phase contrast image we obtained exactly matches the proposed model. The faint structures between the undulating streaks are the parabolic focal conics. The two types of defects always coexist (18).

2. The Complementary Structure of Parabolic Focal Conics (PFC's)

Lecithin forms another well-known defect structure, parabolic focal conics (PFC's). The microscopy texture of PFC's is in the form of so-called polygonal arrays (18). Figure 3.4(a) shows the confocal reflection image when the microscope is focused on the top layers. A mechanical operation specific for confocal optics, phi-z sectioning, was utilized to visualize the structure of the cross sectional view corresponding to the scanning line indicated by the white line on the bottom half of Figure 3.4(a). Another operation that determines where light reflection is the strongest was then used. The two operations yield two uneven lines as shown in the top half of Figure 3.4(a) that indicate that there are two layers with the strongest light reflection in this Smectic A liquid crystal. By comparing the two broken lines, we can conclude that the two layers are complementary to each other. A clear x-y image corresponding to the bottom broken line can be obtained by lowering the focal plane (Figure 3.4(b)). By overlaying the top (red) and bottom (black and white) images (Figure 3.4(c)), the complementary nature of the polygonal arrays is further illustrated.

Figure 3.4. Parabolic focal conics by confocal reflection microscopy. (a) bottom part: confocal reflection image when the focal plane is at top of specimen. The white line is the laser scanning line where the phi-z sectioning starts; top part: two broken lines are phi-z sectioning after vertical maximum which determines the strongest reflective layers. Note the complementary nature of the two broken lines. (b) the clear confocal reflection image when the focal plane is at the bottom of specimen. (c) the overlay view of top (red) and bottom (black and white) images. Bar scale in (b) is 25 μm.

(a)

(b)

(c)

72
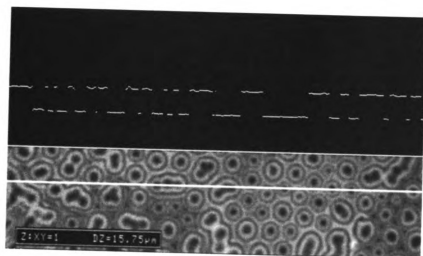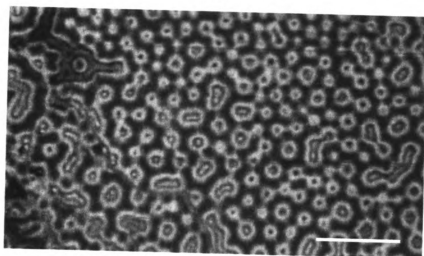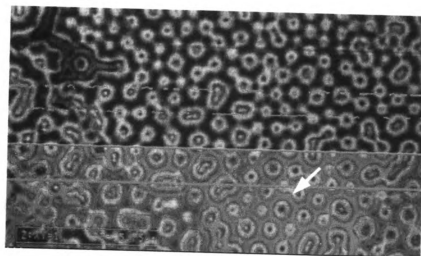
The model responsible for the PFC's has been proposed in both thermotropic (19) and lyotropic (18) Smectic A liquid crystal as shown in Figure 3.5(a). In this model, lipid layers are not flat. Instead, lipids within each layer are tilted towards cusps, which then causes bilayer surface fluctuation. Therefore, concave surfaces are formed centered at cusps while convex between 2 cusps. The concave surfaces centered at cusps behave like a concave lens. Light reflected from the surface is thus focused and the corresponding images around cusps appear bright. In opposite, the confocal reflection images appear dark for the convex surfaces between cusps since light reflected from the surface is dispersed. Connecting the cusps at each individual smectic layer forms parabolas. The paired parabolas from the top half and the bottom half of the specimen pass through each other's focus and are orthogonal as diagrammed in Figure 3.5(b). The two orthogonal parabolas give rise to the complementary cusp positions between the top and bottom smectic layers, which then gives rise to the complimentary nature of PFC's.

3. Bubble Domain and Stripe Domain

A bubble domain was formed when lecithin was mixed with 15% cholesterol. The bubble domain is confirmed by the unique Maltese cross with arms at the 45^0 and 135^0 position under cross polarizers (Figure 3.6(a)). The bubbles, each about 5.5 μm in diameter, are imbedded in the homeotropic matrix of Smectic A phase. Close packing of the bubbles leads to an approximately hexagonal structure. The hexagonal packing is further illustrated by the phase contrast (Figure 3.6(b)) and confocal reflection images (Figure 3.6(c)). The appearance of phase contrast image (Figure 3.6(b)) can be described

Figure 3.5 The model for the parabolic focal conics and the complementary nature of layers. (a) three-dimensional view of layer tilts at top and bottom layer. The tilted layer forms cusps within each layer. Connecting the cusps at each individual layer forms parabola. (b) the cusp positions at top (filled circle) and bottom (open circle) which are complementary to each other due to the orthogonal crossing parabolas. Adapted from reference 18, 19.

TOP
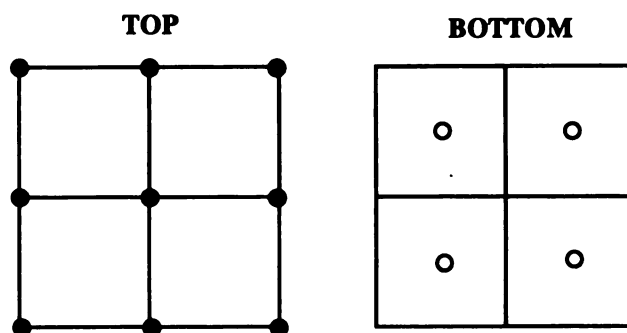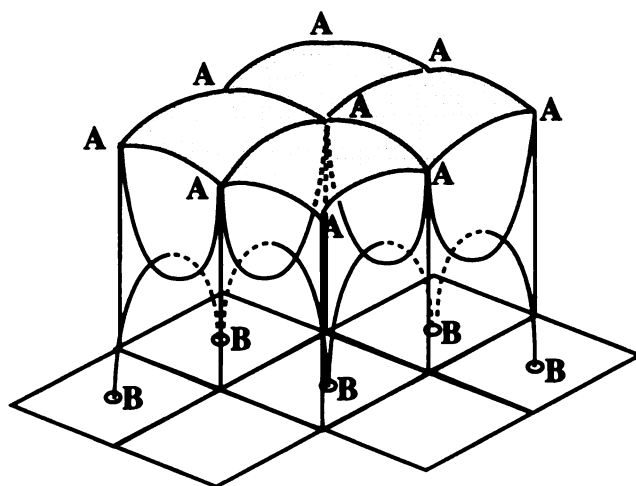
BOTTOM

A: cusp at top layer

B: cusp at bottom layer

Figure 3.6. the bubble and stripe domains under (a) polarization mode; (b) phase contrast mode; (c) confocal reflection mode. Note the coexistence of stripe domains and bubble domains in (b) and (c). A, B, C in (c) denote the different stages of stripe-to-bubble domain transition. Bar scale in (a) is 10 μm.
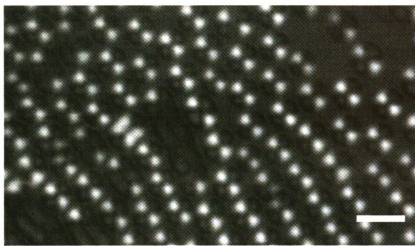
(a)
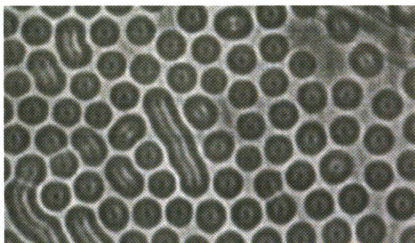
(b)
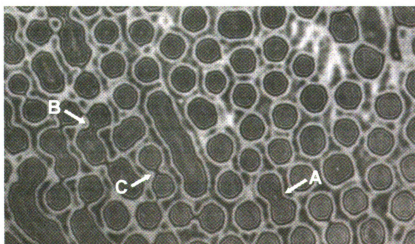
(c)

as a black dot at the center, a bright circle around the black dot and then black circle at edge of the bubble. The structure can be visualized more clearly in the enlarged images (Figure 3.7(a)). In the confocal reflection image, the most prominent appearance is the concentric interference fringe within each bubble. Figure 3.7(b) is the enlarged image to facilitate the visualization of the interference fringe. Along with the bubble domain, stripe domains, either longer or shorter, are also found in the Smectic A phase. The stripe domain is closely related to the bubble domain, which will be discussed in the following.

According to Cladis and Kléman's notation, the molecular alignments (20,21) in Figure 3.8 are responsible for the stripe and bubble domains (Figures 3.6 and 3.7). Let's focus first on the phase contrast images since they give more direct molecular alignment information. In the center of the bubble, molecules are normal to the microscope slide. The optical axis of the molecules is therefore parallel to the light propagation direction. The refractive index n at the center is equal to $n_\perp$ or n_o. No birefringence or refractive index difference is produced in this region. The image in the center therefore appears dark. As one moves outwards from the center, the lipid optical axis then gradually moves away from the light propagation direction. The extraordinary refractive index n_e becomes larger and larger until the light propagation direction is perpendicular to the lipid optical axis where n_e is the highest. n_e then diminishes as the light propagating direction is no longer perpendicular to lipid OA. The refractive index difference in this region gives rise to the bright circle band in Figure 3.6(b) and Figure 3.7(a). At edge of the bubble, the molecule OA is parallel to the light propagating direction again. As a result, the image at

Figure 3.7. (a) Phase contrast image of enlarged bubble domain. Note the black Dot in the center, the bright circle in the middle and the black fringe at edge of the bubble. (b) The concentric interference fringe of confocal reflection image. Bar scale in (b) is 5 μm.
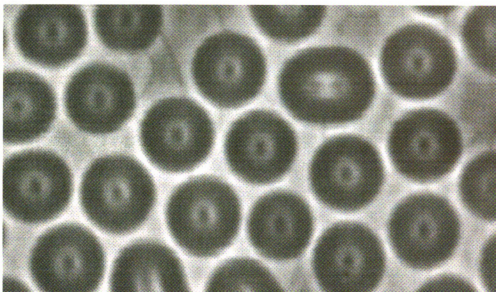
(a)
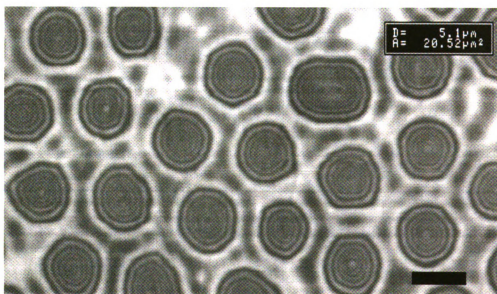
(b)

Figure 3.8. Molecular alignments for (a) bubble and (b) stripe domains. Dot: lipid perpendicular to paper; short stripe: lipid parallel to the paper; nail: lipid aligned at an angle with respect to the paper normal. Arrows in (b) show where the stripe-to-bubble transition is initiated. Adapted from reference 20, 21.
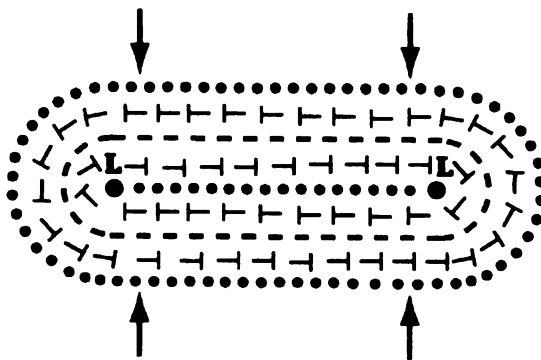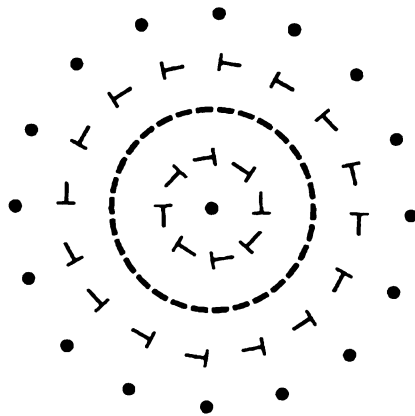
L: Singularity

that point appears black, just like the center of the bubble domain. The same argument applies to the appearance of stripe domain shown in Figure 3.6(b).

The concentric interference fringes in the confocal reflection image are due to refractive index differences within each bubble. The difference in refractive index renders the optical path difference:

$$\Delta = \left| n_{/\!/} - n_{\perp} \right| d$$

where $n_{\perp}$ denotes the refractive index when the light propagating direction is parallel, the electric field of the radiation perpendicular, to lipid OA. The $n_{\perp}$ is equal to n_o, the ordinary refractive index. $n_{/\!/}$ is equal to n_e, the extraordinary refractive index, when electric field is parallel to lipid OA. d is the specimen thickness. When the two rays, ordinary ray and extraordinary ray, are focused together by the microscope lens, the concentric interference fringes are thus formed.

A stripe domain can undergo a transition to a bubble domain. The transition, stripe contracting to bubble, was initiated near the singularity "L" in Figure 3.8(b) because high elastic stress around the singularity caused domain shape instability. The domain shape instability and subsequent domain transition are common phenomena in a variety of chemical, physical and biological systems (22-24). A common mechanism based on the framework of competing interactions has been proposed recently by Seul and Andelman (25). The transition between bubble and stripe is considered to be a first

order process. After passing an energy barrier (21a), the stripe goes through a smooth and continuous transition (contracting) process and finally becomes a bubble. Our snapshot images, especially the confocal reflection image, exactly document the transition (contracting) process in the order of A to C in Figure 3.6(c). The domain shape transition process can also be visualized in real time by generating a gentle hydrodynamic flow. The detail analysis about this part of work will be published elsewhere (26).

Conclusions

The structures, phase properties and dimensions of the defects and other morphological features of lipid liquid crystals, as discerned by phase contrast and confocal reflection microscopy, are consistent with accepted physical models on how light interacts with partially ordered lipid multilayer structures. These forms of microscopy were utilized to visualize common defect structures revealed by conventional polarizing microscopy. The images we obtained under phase contrast microscopy exactly correlated with the molecular alignment models of oily streaks, bubble domains and stripe domains. Confocal reflection microscopy revealed the complementary nature of parabolic focal conics. The stripe to bubble domain transition process was clearly observed at different stages under both confocal reflection and phase contrast microscopy. As we have demonstrated here, phase contrast and confocal reflection microscopy provide a strong analytical means of characterizing lipid liquid crystalline systems.

Reference

1. Singer, S.J.& Nicolson, G.L. *Science* **1973**,175, 720

2. Collins, P.J. *Liquid Crystals,* Princeton University Press: Princeton, New Jersey, 1990

3. Kelker, H. And Hatz, R. *Handbook of Liquid Crystals,* Verlag Chemie, 1980

4. Kléman, M. *Points, Lines and Walls,* J. Wiley: New York, 1983

5. De Gennes, P.-G. And Prost J. *The Physics of Liquid Crystals,* 2nd ed.; Charendon: Oxford, 1993

6. Hénon, S. and Meunier, J. *Rev. Sci. Instrum.,* **1991,** 62, 936

7. Hönig, D. and Dietmar, M. *J. Phys. Chem.* **1991,** 95, 4590

8. Schaaf, P., Déjardin, P. and Schmitt A. *Langmuir,* **1987,** 3, 1131

9. Makimoto, T., Yamauchi, Y., Kobayashi, N., Horikoshi, Y. *Japan. J. Appl. Phys.* **1990,** 29, L207

10. Pedrotti, F.L. & Pedrotti, L.S. *Introduction of Optics*, Prentice-Hall: New Jersey, 1987; Chapter 18

11. Caffrey, M and Feigenson, G. *Biochemistry* **1984,** 23, 323

12. Katsikas, H. and Quinn, P. *Eur. J. Biochem.* **1982,** 124, 165

13. Small, D. *J. Lipid Res.* **1967,** 8, 551

14. Lipowsky, R. *Nature* **1991,** 349, 475

15. Asher, S.A. and Pershan, P.S *Biophys. J.* **1979,** 27, 393

16. Schneider, M.B. and Webb, W.W. *J. Phys. (Paris)* **1984,** 45, 273

17. Kléman, M., Williams, C. E., Costello, M.J. and Gulik-Krzywicki, T. *Philos. Mag.* **1977,** 35, 33

18. Asher, S.A. and Pershan, P.S *J. Phys. (Paris)* **1979,** 40, 161

19. Rosenblatt, C.S., Pindak, R., Clark, N.A. and Meyer, R.B. *J. Phys. (Paris)* **1977**, 38, 1105

20. Kawachi, M., Kogure, O. and Kato, Y. *Japan. J. Appl. Phys.* **1974,** 13, 1457

21. Nawa, N. & Nakamura, K. (a): *Japan. J. Appl. Phys.* **1978,** 17, 219; (b): *Japan. J. Appl. Phys.* **1978,** 17, 2165

22. Ouyang, Q. And Swinney, H. L. *Nature* **1991,** 352, 610

23. Seul, M. and Chen, V. S. *Phys. Rev. Lett.* **1993,** 70, 1658

24. Meinhart, H. *Models of Biological Pattern Formation,* Academic: New York, 1982

25. Seul, M. and Andelman, D. *Science* **1995,** 267, 476

26. Du, X. and Hollingsworth, R. I. Manuscript in preparation

Chapter 4

A Novel Dipyrenyl Membrane Probe: Spectroscopic and

Thermodynamic Properties and Influence of Viscosity

Introduction

Fluorescence has been widely used to measure membrane properties for two reasons: first, fluorescence lifetime is in the time scale of many membrane motions; second, a wide number of fluorescence probes are available so that specific information about membrane can be generated (1). Of the many fluorescence probes, those similar to a lipid are the most suitable for membrane studies because they best fit best into membrane organization and minimize the associated perturbation, providing information that is related to the properties of the system under (2).

Pyrene associated membrane probes are one type of the most popular probes. First of all, fluorescence of pyrene has very high quantum yield and thus provide enough sensitivity. Secondly, excimer can be formed upon excitation and subsequent association of pyrene at excited state with pyrene at ground state. The excimer emission with very high quantum yield is red-shifted and well separated from the monomer emission (3).

Single pyrene labeled lipid either at lipid head group or at the end of one lipid aliphatic chain has been used for quite long time mainly for studying membrane lateral diffusion (4-8). Upon light excitation, the probe at excited state diffuses around until it finds another probe at ground state within the fluorescence lifetime to form intermolecular excimer, which then gives out excimer emission. In order to have reasonable amount of excimer emission, a relative high concentration of this probe has to be doped in the membrane (2), which may cause a strong perturbation to the real

membrane organization. An additional drawback for this monopyrenyl lipid probe is that the probe must be randomly distributed in the host membrane system in order to apply a suitable model, which is hard to fulfill especially in gel phase (9).

One way to avoid this situation is to label pyrene at each end of lipid aliphatic chains. So the excimer can be formed intramolecularly (a pseudo-monomolecular reaction) instead of intermolecularly (a bimolecular reaction). The intramolecular excimer formation depends primarily on the closeness and relative orientation of the two pryene moieties within the same molecule. A direct but probably oversimplified vision to explain the excimer formation is that two pyrene moieties at end of lipid chains come together first through translational diffusion and reorient themselves to a suitable conformation for the excimer formation through rotational diffusion (10). Both translational and rotational diffusions are sensitive to the immediate environment in which the probe resides, which enables the probe to be sensitive to the membrane microenvironment such as microviscosity (11, 12).

The commercially available dipyrenyl probe (13) is mostly phospholipid based. The potential drawback for this type of probe is that the probe is vulnerable to enzyme, especially phospholipase, if the probe is incorporated into biological membranes, and thus gives erroneous information. A new routine to synthesize a dipyrenyl probe without phosphate in the lipid head group has been reported recently (14). Due to the lack of phosphate, phopholipase C and D will have no reaction with the probe. Our initial experimental results also indicated that the probe is resistant to phospholipase A_1 and A_2

(15). In addition, the probe introduces a positive charge at the head group, which can interact with negative charged species such as DNA. Therefore, the probe is a potential tracer to trace DNA transfection process in gene therapy. In this report, we studied the spectroscopic properties and measured thermodynamic parameters of this probe in isotropic media. We found that the excimer formation is strongly influenced by solvent viscosity.

Materials and Methods

1. Chemicals

The probe synthesis was reported early (14). The purity of the probe was checked by TLC (4 : 1 CH_3Cl : CH_3OH). Pyrene butyric acid (PBA) was from Aldrich (Milwakee, WI) and used without further purification. The structures of the dipy probe and PBA are shown in Figure 4.1. All of solvents were of Spectra AR grade and used without further purification.

2. Solvent Viscosity Measurement

Solvent viscosity was varied by mixing different ratios of acetonitrile and PEG 600 (polyethylene glycol with average molecular weight: 600). The kinematic viscosity of the solvent mixtures was determined with Cannon-Fenske viscometers (Ace Glass, Vineland, NJ) which were thermostated in 50:50 ethylene glycol : water bath controlled by Neslab RTE-111 (Portsmouth, NH). The densities of the solvent mixtures were
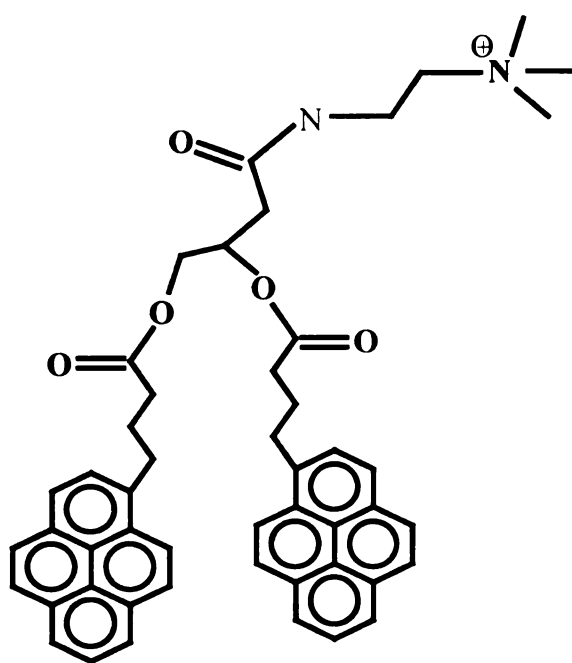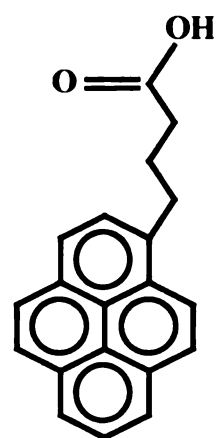
(A)   (B)

Figure 4.1. The chemical structures of dipy (A) and PBA (B).

determined by specific gravity bottles (Ace Glass, Vineland, NJ). The absolute viscosity was then product of kinematic viscosity and solvent density.

3. Fluorescence Measurement

All of the fluorescence measurements were made on FluoroMax-2 (Instruments S.A. Inc., NJ). The excitation for the emission spectra was set at the second vibrational band (0-1) of the $S_0 \rightarrow S_2$ transition. This wavelength is in the range of 326 ± 2 nm depending on solvent refractive index. The emission wavelength for excitation spectra was chosen at 0-0 band of monomer emission, normally at 375 nm. The peak of excimer emission is around 470 nm, varying very little with solvent polarity. The excimer-to-monomer ratio (E/M) was the intensity ratio of the emission at 470 nm and 375 nm respectively. The sample temperatures were regulated by a water bath (RTE-111, Neslab Instruments, Inc., Portsmouth, NH). The temperatures were recorded by a Fluke 51 K/J thermocouple (John Fluke MFG Co., Everett, WA) inserted into the fluorometer cell compartment in close contact with quartz cell.

The samples were degassed through freeze-pump-thaw cycles (at least 3 times) All solvents showed no fluorescence in the range of interests. All of the spectra reported here were solvent (background) subtracted.

Results and Discussion

1. UV Absorption Spectra and Fluorescence Spectra

Absorption spectra and excitation spectra of dipy in organic solvents are similar to the spectra of PBA. Beer's law is obeyed by the absorption of dipy for concentration up to 20 μM. The absorption is saturated for concentration above 20 μM. The molar extinction coefficient of dipy in ethanol at 342 nm is 80,000 $M^{-1}cm^{-1}$ in good agreement with the result of di-(1-pyrenedecanoyl)-phophatidylcholine (9).

The peak positions of absorption and fluorescence spectra in different solvents studied were listed in Table 4.1 along with solvent refractive indices (n), refractive index parameters (f(n)), dielectric constants (ε) and polarity parameters (Δf). The peak maximum of absorption or excitation spectra is assigned as the 0-0 band of $S_0 \rightarrow S_2$ transition of pyrenyl chromophore while the peak maximum of monomer fluorescence as the 0-0 band of $S_1 \rightarrow S_0$ transition. From Table 4.1, the absorption spectra shifted towards red as increasing solvent refractive indices in accordance with McRae theory (16, 17). Both monomer and excimer bands of the fluorescence spectra of dipy as shown in Table 4.1, however, are affected very little by solvent polarities in contrast with absorption spectra. This suggested that dipole moments in S_1 state are similar to those of S_0 state while the dipole moments in S_2 state do differ from those of S_0 state. These observations on dipole moments at S_1 and S_2 state can also partially explain the weak absorption of the $S_0 \rightarrow S_1$ but strong absorption of $S_0 \rightarrow S_2$ in the absorption spectra of pyrene and pyrene derivatives such PBA and dipy.

Table 4.1. Some physical parameters of organic solvents and the emission (0-0 band, $S_1 \to S_0$) and absorption (0-0 band, $S_0 \to S_2$) maxima of dipy in these solvents at 25 ^{0}C.

solvent	ε	n	Δf	f(n)	λ_e (nm)	λ_a (nm)
ethanol	24.3	1.361	0.2886	0.1812	374.2	340.9
t-amyl alcohol	5.82	1.405	0.1844	0.1969	374.2	341.4
n-pentanol	13.9	1.410	0.2493	0.1986	374.3	342.1
n-octanol	10.3	1.430	0.2254	0.2051	374.4	342.7
2-octanol	9.1	1.426	0.2179	0.2040	374.4	342.6

ε: dielectric constant; n: refractive index; λ_e: emission maximum; λ_a: absorption maximum; Δf: solvent polarity parameter, $\Delta f = (\varepsilon - 1)/(2\varepsilon + 1) - (n^2 - 1)/(2n^2 + 1)$; f(n) = $(n^2 - 1)/(2n^2 + 1)$.

Physical parameters of solvents are from *CRC Handbook*, 66th edition, CRC Press: Boca Raton, FL,.

Figure 4.2 shows the fluorescence spectra of dipy and PBA with the same concentration of pyrene moieties (5 μM). A strong excimer fluorescence is formed in dipy but no excimer in PBA. For PBA in such a low concentration, pyrene moiety at excited state couldn't diffuse far enough to find another pyrene to form excimer within the fluorescence lifetime. For dipy, however, the two pyrene moieties are always in close contact through bond connection. Upon light excitation, one pyrene moiety at excited state can almost certainly associate with another one in the same molecule to form excimer. The excimer formation within the same molecule is called intramolecular excimer formation. The excimer-to-monomer ratio is a function of temperature, solvent viscosity, which will be discussed in the following, but not a function of dipy concentration in the low concentration range.

2. Solvent Viscosity Effects

In order to form intramolecular excimer, the pyrene moieties in dipy have to diffuse together and orient themselves to a optimum configuration in which two pyrene rings are in a plane-parallel orientation with distance between pyrene planes about 3.5 A$^{\circ}$ (18). The molecular motion can be pictured (maybe oversimplified) by translational diffusion to bring the two pyrene moieties together and rotational diffusion to re-orient them (10). Both diffusions are directly related to solvent viscosity. Figure 4.3 shows that the rate constant for excimer formation as represented by E/M ratio is indeed strongly affected by solvent viscosity.
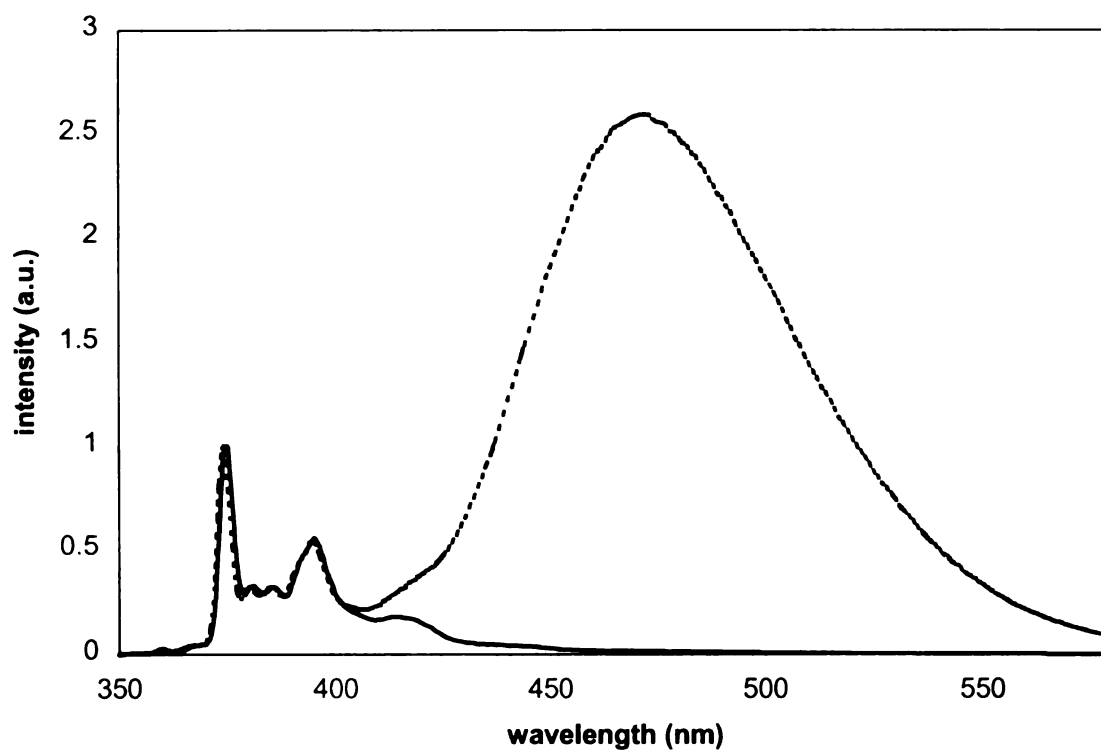
Figure 4.2. The normalized fluorescence spectra of dipy (dashed line) and PBA (solid line). The concentrations of pyrene moiety for dipy and PBA are 5 μM. The temperature is thermostated at 20 °C. Note the strong excimer emission for dipy but no excimer emission for PBA.
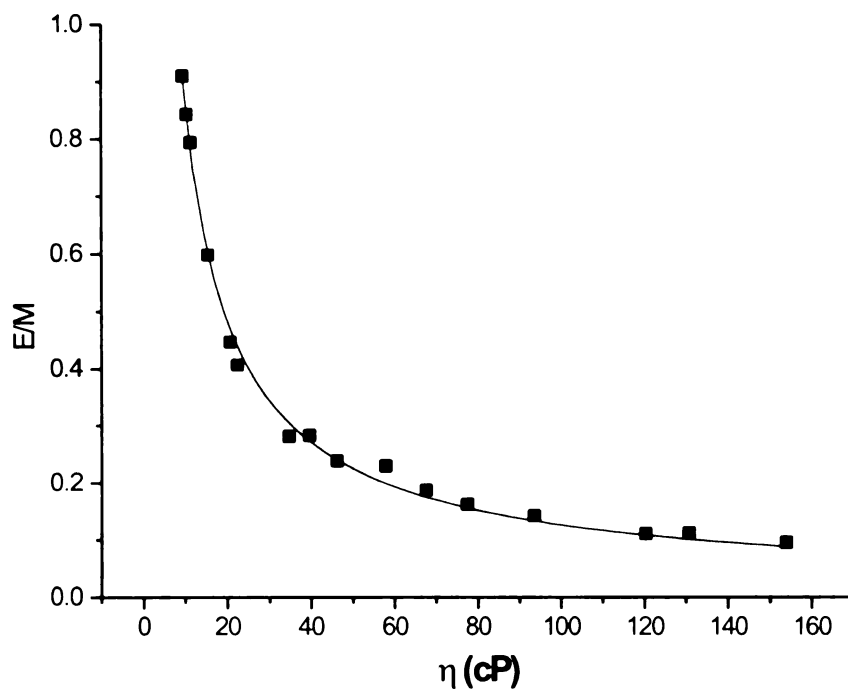
Figure 4.3. The solvent viscosity effects on the rate constant (E/M) for intramolecular excimer formation. Solid squares are the actual data points. The solid line is the best curve fitting based on Equation 4 with α = 0.80. All of the data are measured at temperature: 5 ^{0}C.

The kinetic mechanism of pyene excimer formation was first proposed by Birks (3) in the case of intermolecular excimer formation. The mechanism was later modified for intramolecular excimer formation of 1, 3-di(1-pyrenyl) propane (DPP) in isotropic solvent (11, 19). The kinetic process of intramolecular excimer formation in dipy is believed similar to the mechanism in DPP, which is shown in scheme 4.1:
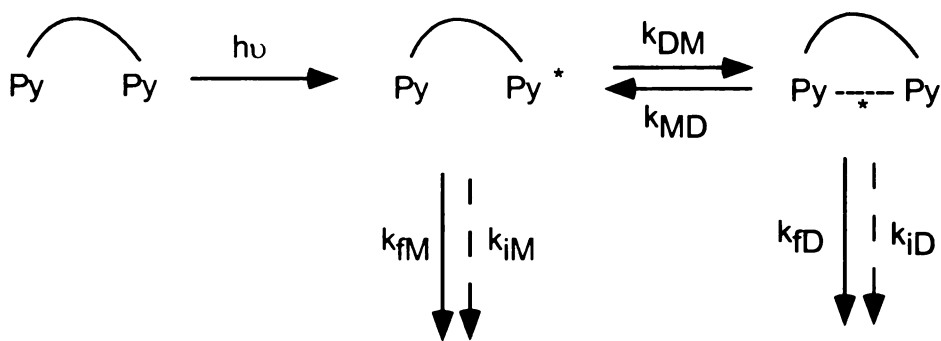
Based on the above mechanism and assuming a δ-function of the light pulse, the rate equations after excitation are giving as following (20, 21):

$$d[M^*]/dt = -(k_M + k_{DM})[M^*] + k_{MD}[D^*] \qquad (4.1)$$

$$d[D^*]/dt = -(k_D + k_{MD})[D^*] + k_{DM}[M^*] \qquad (4.2)$$

where M^* and D^* represent monomer and excimer at excited state, respectively; $k_D = k_{fD} + k_{iD}$; $k_M = k_{fM} + k_{iM}$. At $t = 0$, $[M^*] = [M^*]_0$ and $[D^*] = 0$ (20, 21).

According to the definition of the monomer and excimer quantum yields (20),

98

$$\phi_M = k_{fM} [M^*]/I_0 \tag{4.3}$$

$$\phi_E = k_{fD} [D^*]/I_0 \tag{4.4}$$

where I_0 is the quanta absorbed by monomer. From Equation 4.3 and 4.4

$$\frac{\phi_E}{\phi_M} = \frac{k_{fD}}{k_{fM}} \times \frac{[D^*]}{[M^*]} \tag{4.5}$$

From steady state approximation, $d[D^*]/dt = 0$. Equation 4.2 is thus reduced to

$$[D^*]/[M^*] = k_{DM}/(k_{MD} + k_D) \tag{4.6}$$

Combining Equation 4.5, 4.6 and $k_D = k_{fD} + k_{iD}$,

$$\frac{\phi_E}{\phi_M} = \frac{k_{fD}}{k_{fM}} \times \frac{k_{DM}}{k_{MD} + k_{fD} + k_{iD}} \tag{4.7}$$

A more vigorous derivation of Equation 4.7 without steady state approximation can also be obtained. With the initial condition at t = 0, Equation 4.1 and 4.2 can be solved as (20)

$$[M^*] = \frac{[M^*]_0}{\lambda_2 - \lambda_1} \{(\lambda_2 - k_M - k_{DM})e^{-\lambda_1 t} + (k_M + k_{DM} - \lambda_1)e^{-\lambda_2 t}\} \tag{4.8}$$

$$[D^*] = \frac{[M^*]_0}{\lambda_2 - \lambda_1} k_{DM} \{e^{-\lambda_1 t} + e^{-\lambda_2 t}\} \qquad (4.9)$$

where

$$\lambda_{2,1} = \frac{1}{2}\{k_M + k_{DM} + k_D + k_{MD} \pm [k_D + k_{MD} - k_M - k_{DM}]^2 + 4k_{DM}k_{MD}]^{1/2}\} \qquad (4.10)$$

The quantum intensity of monomer fluorescence (per initial excited molecule of M) (21) at time t is

$$i_M(t) = \frac{k_{fM}[M^*]}{[M^*]_0} = \frac{k_{fM}(\lambda_2 - X)}{\lambda_2 - \lambda_1}(e^{-\lambda_1 t} + Ae^{-\lambda_2 t}) \qquad (4.11)$$

where $X = k_M + k_{DM}$ and $A = (X - \lambda_1)/(\lambda_2 - X)$. The quantum intensity of excimer fluorescence (per initial excited molecule of M) (21) at time t is

$$i_E(t) = \frac{k_{fD}[D^*]}{[M^*]_0} = \frac{k_{fD}k_{DM}}{\lambda_2 - \lambda_1}(e^{-\lambda_1 t} - e^{-\lambda_2 t}) \qquad (4.12)$$

The total quantum yield of monomer fluorescence is

$$\phi_M = \int_0^\infty i_M(t)d(t) = \frac{k_{fM}Y}{k_M Y + k_{DM}k_D} \qquad (4.13)$$

$$\phi_E = \int_0^\infty i_D(t)d(t) = \frac{k_{fD}k_{DM}}{k_M Y + k_{DM}k_D} \qquad (4.14)$$

100

where

$$Y = k_{fD} + k_{iD} + k_{MD} \qquad (4.15)$$

From Equation 4.13, 4.14, 4.15

$$\frac{\phi_E}{\phi_M} = \frac{k_{fD}}{k_{fM}} \times \frac{k_{DM}}{k_{MD} + k_{fD} + k_{iD}} \qquad (4.16)$$

Equation 4.16 has the exact same expression as Equation 4.7.

For the sake of convenience, quantum yield ratio (ϕ_E/ϕ_M) in Equation 4.16 has often been replaced by excimer-to-monomer intensity ratio (E/M) in both isotropic solvent system (11, 31, 34) and membrane system (2, 4, 32, 37-39). The ϕ_E/ϕ_M and the E/M are connected through a proportionality constant (4, 11, 31, 32, 34). This constant is dependent on the monomer emission band chosen. If the monomer emission band is chosen at the second strongest band (about 395 nm), the proportionality constant is about 1 (2, 37-39). In this experiment, the monomer emission band is chosen at 375 nm, the strongest emission band. In order to determine the proportionality constant, the emission spectra of PBA and dipy at a given solvent mixture have been obtained under identical conditions. The spectra were then normalized with respect to the emission band at 375 nm. The monomer emission spectrum of dipy is almost identical to this of PBA as shown in Figure 4.2. After converting the spectra in wavelength to those in wavenumber, the total monomer emission intensity was obtained by integrating the whole emission

spectrum of PBA. The pure excimer emission spectrum was achieved by subtracting the emission spectrum of dipy from the emission spectrum of PBA and the intensity was obtained by integrating the pure excimer emission spectrum (from 1.72×10^4 cm^{-1} to 2.44×10^4 cm^{-1}). The excimer-to-monomer quantum yield (ϕ_E/ϕ_M) is then the ratio of the total integrated emission intensity ratio. The proportionality constant is obtained by dividing the ϕ_E/ϕ_M by the E/M. The above procedures were repeated under three typical solvent mixtures and within the temperature range in which experiments were normally performed. Thirty constants were generated. The final proportionality constant was the average of the thirty constants and has been determined to be 2.6 ± 0.1 at 95% confidence level. The proportionality constant is not a function of solvent and temperature.

The proportionality constant, however, is really a constant only if the emission band shape of the dipy probe remains unchanged in different solvents with different solvent polarity. This concern originates from the fact that the emission of pyrene is very sensitive to solvent polarity and is often used as a solvent polarity indicator (40). However, pyrene derivatives such as dipy and PBA are much less sensitive to solvent polarity than pyrene itself due to symmetry breaking after derivatization. In addition, the solvent mixture we used to change solvent viscosity is CH$_3$CN and PEG 600. The polarity of PEG 600 and CH$_3$CN is approximately same (i.e.: for CH$_3$CN, n = 1.344, ε = 38.8, polarity parameter Δf = 0.306; for ethylene glycol, n = 1.432, ε = 37, Δf = 0.274 at 20 ^{0}C). Therefore, the polarity of solvent mixture changes very little by varying the solvent composition of CH$_3$CN and PEG 600. This can be further illustrated in the normalized fluorescence spectra of dipy in three solvent mixtures (Figure 4.4). From
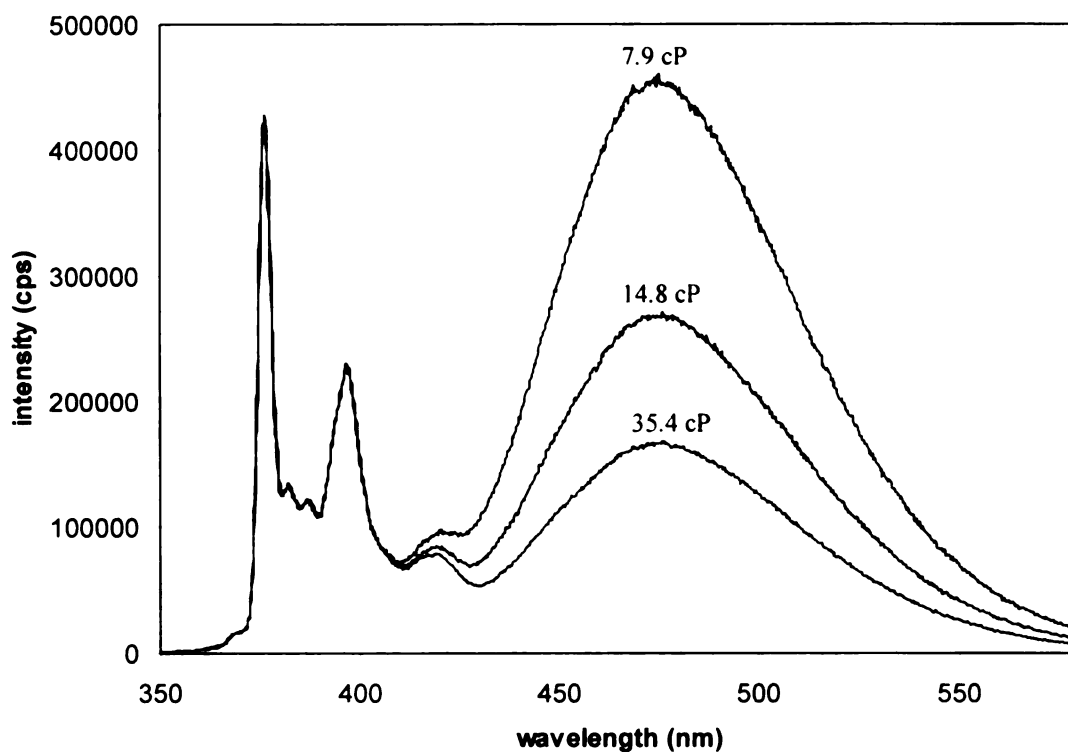
Figure 4.4. The fluorescence spectra of dipy in three solvent mixtures with solvent viscosity: 7.9 cP, 14.8 cP and 35.4 cP at 25 ^{0}C. Note that the band shape of both monomer and excimer emission remains the same at different solvents with different solvent polarity.

Figure 4.4, monomer emission peaks are completely overlapped and the shape of excimer emission remains unchanged. This indicates that under this experimental condition, E/M ratio is adequate to represent ϕ_E/ϕ_M with a proportionality constant.

To conclude the above argument,

$$\frac{\phi_E}{\phi_M} = \beta \frac{E}{M} = \frac{k_{fD}}{k_{fM}} \times \frac{k_{DM}}{k_{MD} + k_{fD} + k_{iD}}$$ (4.17)

where β is the proportionality constant determined to be 2.6 ± 0.1 in this experiment. In the five rate constants, only k_{DM} and k_{MD} depend significantly on solvent viscosity (11). At low temperature and relatively high viscosity, excimer dissociation becomes negligible (19), $k_{MD} << k_{fD} + k_{iD}$. Thus, Equation 4.17 is reduced to

$$\beta \frac{E}{M} = \frac{k_{fD}}{k_{fM}} \times \frac{k_{DM}}{k_{fD} + k_{iD}}$$ (4.18)

In Equation 4.18, only k_{DM} is a function of viscosity (11).

$$\frac{E}{M} = A \times k_{DM}$$ (4.19)

where $A = \frac{k_{fD}}{\beta k_{fM}} \times \frac{1}{k_{fD} + k_{iD}}$ is a constant at a given temperature. Therefore, the E/M ratio actually represents the rate constant for excimer formation.

Solvent effects on isomerization dynamics of many fluorescent molecules have been extensively studied both theoretically (22-24) and experimentally (25, 26 and references therein). The early part of the research activities (before 1986) has been reviewed by Bagchi (27). The motions of isomerization reaction in which isomer is formed through translational and rotational diffusion of chromophore around a chemical bond is same as the molecular motions of intramolecular excimer formation. Therefore, the excimer formation rate as represented by E/M ratio can be expressed in the following empirical form which is used to relate the isomerization rate with solvent viscosity and reaction temperature (27):

$$\frac{E}{M} \propto k_{DM} = A\eta^{-\alpha} \exp(-E_0 / kT) \tag{4.20}$$

where A is a viscosity-independent constant and E_0 is the intrinsic activation energy barrier. k is the Boltzmann constant and T is the temperature in Kelvin. The exponent α is in the range of $0.1 \leq \alpha \leq 1$, which is the measure of the relative importance of the viscosity. The α value from this fit is 0.80 ± 0.02.

Solvent viscosity effects on intramolecular excimer formation rate can be explained by Kramers' theory (28) if the excimer is formed after a single hindered rotation over a potential barrier. The typical examples of this kind are 1, 3-bis(2-naphthyl) propane (29) and 1,3-di(1-pyrenyl) propane (DPP) (19, 30). Hara etal (19, 30) found that the viscosity dependence on the formation of intramolecular excimer of DPP

105

can be fitted by Kramers' equation irrespective of solvent polarities, solvent size or solvent-solute mass ratio:

$$k_{DM} = (\sqrt{1 + B^2 \eta^2} - B\eta) \times k_{TST}$$

(4.21)

$k_{TST} = A \exp(-E_0 / kT)$ is the rate constant deduced from transition state theory (TST). $k_{KR} = \sqrt{1 + B^2 \eta^2} - B\eta$ is the transmission coefficient due to solvent friction based on Kramers' theory. η is the solvent viscosity and B is a constant related to effective radius of the rotating chromophore and vibrational frequency at activation barrier region. B has a unit cP^{-1} if the unit of viscosity is cP. Under our experimental condition where the solvent viscosity is 15 cP or higher, it is believed that excimer formation is in diffusing limit in which $(B\eta)^2 \gg 1$ (30, 31). Equation 4.21 is then reduced to

$$k_{DM} = \frac{1}{2B\eta} \propto \frac{1}{\eta}$$

(4.22)

This is so-called the Smoluchowski limit.

The theory described above predicts that α is equal to 1. Our experimental value, however, is 0.80. The deviation can be understood in terms of mode coupling and reaction pathway in the diffusive limit (22, 23). The one-dimensional Kramers' theory breaks down because thirteen bonds between the two pyrene moieties instead of 4 bonds

in DPP renders many non-reactive modes besides the reactive mode. The detail analysis is not in the scope of this chapter and will be the subject of Chapter 6.

3. Thermodynamic Constants of Dipy Excimer Formation

In the previous section, we discussed the effect of solvent viscosity on excimer formation rate and obtained a series of approximate equations. In this section, we will discuss the effect of temperature on the excimer formation rate in a similar analogy.

At low temperature and high viscosity such as the solvent mixture of acetonitrile and PEG 600 in this experiment, $k_{MD} \ll k_{fD} + k_{iD}$ (3, 19). Equation 4.17 is thus reduced to Equation 4.18. The radiative rate constants k_{fD} and k_{fM} are independent of solvent and temperature (3). In the low temperature range, k_{iD} is also independent of temperature as evidenced by the iso-emissive point of dipy fluorescence spectra when temperature is varied (Figure 6.2 in chapter 6) (32-34). Therefore, only k_{DM} in Equation 4.18 is a function of temperature:

$$\frac{E}{M} = C \times k_{DM} \qquad (4.23)$$

Where $C = \dfrac{k_{fD}}{\beta k_{fM}} \times \dfrac{1}{k_{fD} + k_{iD}}$ is a constant in low temperature range. E/M is thus the representation of k_{DM}, the rate constant for intramolecular excimer formation. According to Bagchi (25),

$$\frac{E}{M}(\propto k_{DM}) = F(\eta)\exp(-E_0 / kT) = A\eta^{-\alpha}\exp(-E_0 / kT) \quad (4.24)$$

F(η) is the pre-exponential factor which includes the solvent viscosity effect. From the graph ln(E/M) vs. 1/T, one can obtain the activation energy. However, the observed activation energy is not the intrinsic activation energy E_0 that separates the initial and final states on potential surface of the reaction coordinate. It also contains the contribution from the activation energy due to solvent viscous flow. The normal method to extract the intrinsic activation energy is through the iso-viscosity plot (25). By holding viscosity or the pre-exponential factor constant and varying temperature, the intrinsic activation energy E_0 can be extracted. However, this method generates significant data variance in our case. The method we used here is first to fit the curve E/M vs. η such as in Figure 4.3 according to Equation 4.24 at one temperature. The viscosity effect is included in F(η), leaving C = A exp($-E_0$/kT) as the function of temperature. A series of factor C can be generated by varying temperature. From the slope of a plot of a ln C vs. 1/T (Figure 6.7 in Chapter 6), E_0 is then obtained as 7.3 kJ/mole. The intrinsic energy barrier for dipy in this experiment is about half of the value for DPP (30). This is reasonable considering the longer chain length between pyrene moieties in dipy provides more flexibility for the necessary bond rotation to form excimer than the one in DPP. The advantage of this method is that every data point at one temperature is the average of the full range of viscosity. The data varaince is significantly reduced and more accurate value is thus obtained.

Another limiting case is at high temperature where $k_{MD} \gg k_{fD} + k_{iD}$. In this case, Equation (4.17) is reduced to:

$$\beta \frac{E}{M} = \frac{k_{fD}}{k_{fM}} \times \frac{k_{DM}}{k_{MD}} \qquad (4.25)$$

k_{DM}/k_{MD} the true molar equilibrium constant for the excimer formation. Again, k_{fD}/k_{fM} is independent of temperature. Therefore, E/M represents the equilibrium constant. This corresponds to Birks' "high temperature dynamic equilirium region" (3). Figure 4.5 shows ln (E/M) vs. 1/T of dipy in acetonitrile in high temperature range. The slope of the straight line gives - $\Delta H/R$ and then ΔH = -8.0 kJ/mole. The negative value signifies the excimer reaction is exothermic and the excimer is stabilized energetically.

The solvent viscosity effect on excimer formation is included in the pre-exponential factor $F(\eta)$ (Equation 4.24). The rate constant for excimer dissociation is also a function of solvent viscosity and the solvent effect on excimer dissociation can be written in a similar equation as Equation 4.24:

$$k_{DM} = F'(\eta) \exp(-E_0{}'/kT) \qquad (4.26)$$

$E_0{}'$ is the activation energy for excimer dissociation. Experimental results have showed that k_{DM} and k_{MD} have the same dependence on viscosity for 1, 3-bis(N-carbazoyl) propane (35), 1, 3-bis(1-naphthyl) propane (29) and 1, 3-bis(4-biphenyl) propane (36). It
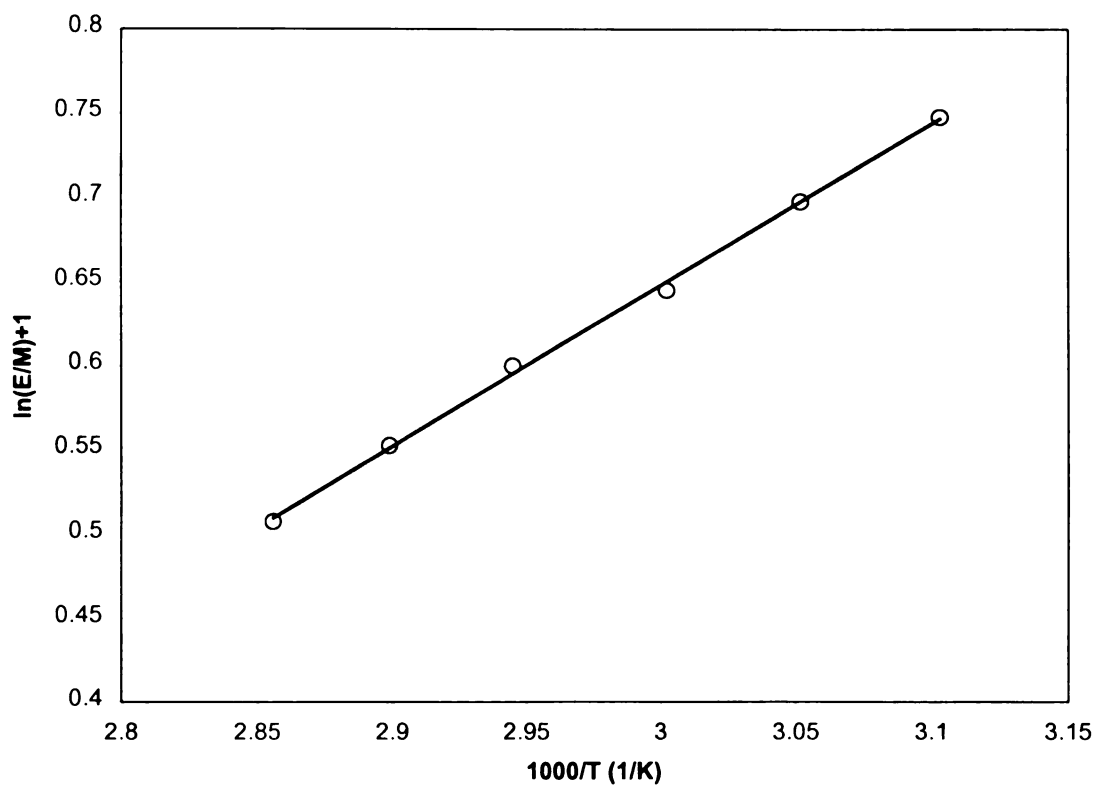
Figure 4.5. ln (E/M) vs. 1/T plot at high temperature dynamic equilibrium region. The slope of the plot yields the enthalpy for intramolecular excimer formation, ΔH: -8.0 kJ/mole.

is therefore reasonable to assume k_{DM}/k_{MD} is independent on viscosity for dipy at least in the same solvent. Under this condition,

$$E_0 - E_0^{'} = \Delta H \qquad (4.27)$$

The activation energy for excimer dissociation $E_0^{'}$ is thus equal to 15.3 kJ/mole.

Conclusion

In this chapter, we characterized the spectroscopic and thermodynamic properties of a novel lipid-like fluorescence probe, dipy, with two pyrene moieties at the end of lipid chains and a positive charge at the lipid head group. The close contact of pyrene moieties through chemical bonds in dipy renders a strong intramolecular excimer emission. Fluorescence and absorption (excitation) spectra in a series of solvents indicated that the dipole moment in S_1 state is similar to the dipole moment in S_0 state while the dipole moment in S_2 state is significantly higher than the one in S_0 state. The intramolecular excimer formation is strongly affected by solvent viscosity. The fitting according to equation $k_{DM} = A\eta^{-\alpha} \exp(-E_0/kT)$ yielded α value 0.80. The deviation of α value from theoretical value 1 is initially suggested due to mode coupling and reactive pathway in diffusive limit.

The mechanism of intramolecular excimer formation has two limiting cases. In the case of low temperature, the intrinsic activation energy barrier of excimer formation

is determined as 7.3 kJ/mole. At high temperature regime, we measured the enthalpy ΔH of the excimer formation as 8.0 kJ/mole. Under the condition that viscosity has the same effects on excimer formation as excimer dissociation, the intrinsic activation energy for excimer dissociation is equal to 15.3 kJ/mole.

Reference

1. Stubbs, C. D.; Williams, B. D. *Fluorescence in Membrane* chapter 5; in *Topics in Fluorescence Spectroscopy*; Lakowicz, J. R. (ed.); Plenum Press: New York, 1992

2. Hresko, R. C.; Sugar, I. P.; Barenholz, Y.; Thompson, T. E. *Biochemistry* **1986**, 25, 3813

3. Birks, J. B. *Photophysics of Aromatic Molecules;* Wiley Interscience: New York, 1970; Chapter 7

4. Galla, H.-J.; Hartmann, W.; Theilen, U.; Sackmann, E. *J. Membr. Biol.* **1979**, 48, 215

5. Somerharju, P. J.; Virtanen, J.A.; Edlund, K. K.; Vainio, P.; Kinnunen, P. K. J. *Biochemistry* **1985**, 24, 2773

6. Wiener, J. R.; Pal, R.; Barenholz, Y.; Wagner, R. R. *Biochemistry* **1985**, 24, 7651

7. Eisinger, J; Flores, J.; Petersen, W. P. *Biophys. J.* **1986**, 49, 987

8. Caruso, F.; Grieser, F.; Thistlethwaite, P. J.; Almgren M. *Biophys. J.* **1993**, 65, 2493

9. Vauhkonen, M.; Sassaroli, M.; Somerharju, P.; Eisinger, J. *Biophys. J.* **1990**, 57, 291

10. Cheng, K. H.; Ruymgaart, L.; Liu, L.-I.; Somerharju, P.; Sugar, I. P. *Biophys. J.* (a): **1994**, 67, 902; (b): **1994**, 67, 67, 914

11. Zachariasse, K. A. *Chem. Phys. Lett.* **1978**, 57, 429

12. Hara, K.; Suzuki, H. *J. Phys. Chem.* **1990**, 94, 1079

13. Haugland, R. P. *Handbook of Fluorescence Probes and Research materials* 6th edition, Molecular Probes Inc.

14. Huang, G. F.; Hollingsworth R.I. *Tetrahedron* **1998**, 54, 1355

15. Hollingsworth, R. I. *Private Communication*

16. McRae, E. G. *J. Phys. Chem.* **1957**, 61, 562

17. Weigang, O. E. Jr. *J. Chem. Phys.* **1960**, 33, 892

18. De Schryver, F. C.; Collart, P.; Vandendriessche, J.; Goedeweeck, R.; Swinnen, A.; van der Auweraer, M. *Acc. Chem. Res.* **1987**, 20, 159

19. Hara, K.; Yano, H. *J. Am. Chem. Soc.* **1988**, 110, 1911

20. Avouris, P.; Kordas, J.; El-Bayoumi, M. A. *Chem. Phys. Lett.* **1974**, 26, 373

21. Birks, J. B.; Dyson, D. J.; Munro, I. H. *Proc. Roy. Soc. A* **1963**, 275, 575

22. Grote, R. F.; Hynes, J. T. *J. Chem. Phys.* **1981**, 74, 4465

23. Van der Zwan, G.; Hynes, J. T. *J. Chem. Phys.* **1982**, 77, 1295

24. Agmon, N.; Kosloff, R. *J. Phys. Chem.* 1987, 91, 1988

25. Courtney, S. H.; Fleming, G. R. *J. Chem. Phys.* **1985**, 83, 215

26. Schroeder, J. *Ber. Bunsenges. Phys. Chem.* **1997**, 101, 643

27. Bagchi, B. *Intl. Rev. Phys. Chem.* **1987**, 6, 1

28. Kramers, H. A. *Physica* **1940**, 7, 284

29. Fitzgibbon, P. D.; Frank, C. W. *Macromolecules* **1981**, 14, 1650

30. Hara, K.; Akimoto, S.; Suzuki, H. *Chem. Phys. Lett.* **1990**, 175, 493

31. Du, X. Y.; Hollingsworth, R. I. *Manuscript in preparation*

32. Chandross, E. A.; Demster, C. J. *J. Am. Chem. Soc.* **1970**, 92, 3586

33. Goldenberg, M.; Emert, J. Morawetz., H. *J. Am. Chem. Soc.* **1978,** 100, 7171

34. Melnick, R. L.; Haspel, H. C.; Goldenberg, M.; Greenbaum, L. M.; Weinstein, S.

    Biophys.J. 34, 499

35. Johnson, G. E. *J. Chem. Phys.* **1975,** 63, 4047

36. Zachariasse, K. A.; Kuhnle, W.; Weller, A. *Chem. Phys. Lett.* **1978,** 59, 375

37. Sugar, I. P.; Zeng, J. W.; Vauhkonen, M.; Somerharju, P. *J. Phys. Chem.* **1991,** 95,

    7516

38. Cheng, K. H.; Chen, S.-Y.; Butko, P.; Wieb van der Meer, B.; Somerharju, P.

    Biophys. Chem. **1991,** 39, 137

39. Butko, P.; Cheng, K. H. *Chem. Phys. Lipids* **1992,** 62, 39

40. Karpovich, D. S.; Blanchard, G. J. *J. Phys. Chem.* **1995,** 99, 3951

Chapter 5

Lipid Chain Mobility Regulated by Membrane Net Surface Charge:

Direct Evidence from a Novel Dipyrenyl Membrane Probe

Introduction

It is well known that temperature can have huge effects on lipid membrane properties. In most biological systems, however, temperature is kept constant. In the physiological temperature scale, other external parameters such as pH, ionic strength or polar surface of the lipid bilayer, therefore, must play very important role in regulating membrane properties, i.e., chain melting temperature and chain motions. This type of regulatory mechanism provides a faster and energetically less expensive way to control membrane structure and phase behavior than the traditional adaptation theory by changing lipid chain composition (1 and references therein).

The pH effects on the main phase transition of ionizable lipids such as phosphatidic acid (2-4), phosphatidylserine (5), synthetic ionizable glycolipid (6) and the mixture of zwitterionic lipid, phosphatidylcholine, and fatty acid (7, 8) have been well studied. Membrane surface charge due to pH often decreases the phase transition temperature to relieve the electrostatic repulsion because lipid crystalline state is more expanded than the gel state. The more the net surface charge, the lower the phase transition temperature.

The phase transition temperature decrease is often accompanied by the decrease of phase transition enthalpy. The decrease in enthalpy can be explained by the absence of hydrogen bonding due to deprotonation in the case of phosphatidylserine (5). When hydrogen bonding was not considered, Jacobson and Papahadjopoulous (3) proposed that

the enthalpy decrease was because the electrostatic repulsion force at membrane surface caused a disordering effect on lipid aliphatic chain. The entropy of the phase transition is often reduced because of the decrease of enthalpy (i.e.: $\Delta S = \Delta H/T$ for a first order phase transition process). However, their DSC data provided no experimental evidence to support the proposal.

Pyrene and its derivatives have been used to study membrane properties for quite a long time (9-13). There are two reasons for the wide use of this chromophore. First, the fluorescence of pyrene has very high quantum yield (when not quenched by O_2) and thus provides enough sensitivity. Second, the excimer can be formed upon excitation and subsequent association of excited pyrene with ground state pyrene. The excimer emission with very high quantum yield is red-shifted and well separated from the monomer emission (14). The intensities of excimer and monomer can be easily evaluated with high accuracy. The excimer-to-monomer ratio (E/M) is a function of lateral diffusion (9-11), microviscosity (15, 16).

In the pyrene associated membrane probes, dipyrenyl probe in which pyrene is covalently attached to each end of lipid aliphatic chains is especially promising. The excimer in this case can be formed intramolecularly (a pseudo-monomolecular reaction) instead of intermolecularly (a bimolecular reaction). One advantage of this probe is that the E/M is not a function of probe concentration at low concentrations (17). A very low concentration of the probe can be doped in host membrane and thus the perturbation of the probe to the membrane original organization can be minimized. Another advantage of

the dipyrenyl probe is that this probe is a function of the intramolecular dynamics of acyl chains of the molecule itself, which is sensitive to the immediate environment in which the probe resides. Therefore, the probe is able to provide site-specific information (18).

In order to form intramolecular excimers, the pyrene moieties in the dipyrenyl probe have to diffuse together and orient themselves to an optimum configuration in which two pyrene rings are in a plane-parallel orientation with distance between pyrene planes about 3.5 Å (19). A conceptual vision to explain the excimer formation is that two pyrene moieties at end of lipid chains come together first through translational (lateral) diffusion and reorient themselves to a suitable conformation for the excimer formation through rotational diffusion (18). Both translational and rotational diffusions are sensitive to the lipid chain motions, which enables the probe to detect the motional information in membrane aliphatic chain region.

In this report, we have incorporated a novel dipyrenyl probe that has recently been synthesized in this laboratory (20) into DPPC large unilamellar vesicles (LUVs) under two different buffers with pH 4.7 and 6.9. We found that the phase transition enthalpy at pH 4.7 is significantly reduced comparing to the enthalpy at pH 6.9 while phase transition temperature remains same. Fluorescence measurement not only predicted the enthalpy difference under the two pHs but more importantly provided the direct evidence on how lipid membrane surface charge affects the lipid aliphatic chain ordering and motion.

Materials and Methods

1. Chemicals

The probe synthesis was reported early (20). The purity of the probe was checked by TLC (4 : 1 CH_3Cl : CH_3OH). Pyrene butyric acid (PBA) was from Aldrich (Milwakee, WI), DPPC from Sigma (Sigma, MO), both of which were used without further purification. The structures of the dipy probe and PBA are shown in Figure 5.1. Inorganic salts were of reagent grade. All of solvents were of Spectra AR grade and used without further purification.

2. Preparation of Vesicles

For differential scanning calorimeter (DSC) measurement, the multilamellar vesicles (MLVs) were prepared in a vial by drying approximately 1.0 mg DPPC in ethanol under N_2 beam first and subsequently in vacuum for at least 3 hours. The dried DPPC was hydrated in 0.5 ml buffer, heated to about 60 ^{0}C and vortexed. The sample was then frozen (acetone-dry ice, -78 ^{0}C) and reheated and re-vortexted. This freeze-heat-vortex cycle was repeated for several times. The DSC measurements of the MLVs were made on a Microcal-2 high sensitivity scanning calorimeter (Microcal, Inc., Amherst, MA) with heating and cooling rate at 60 ^{0}C/hr. Multiple scans (up to 5) were recorded from 10 ^{0}C to 70 ^{0}C.

For Fluorescence measurements, the samples were prepared first according to the above procedures. The samples contained 0.2 mg of DPPC and 1/1000 in molar ratio of dipy probe. The MLVs were passing through a liposome extruder equipped with a 100
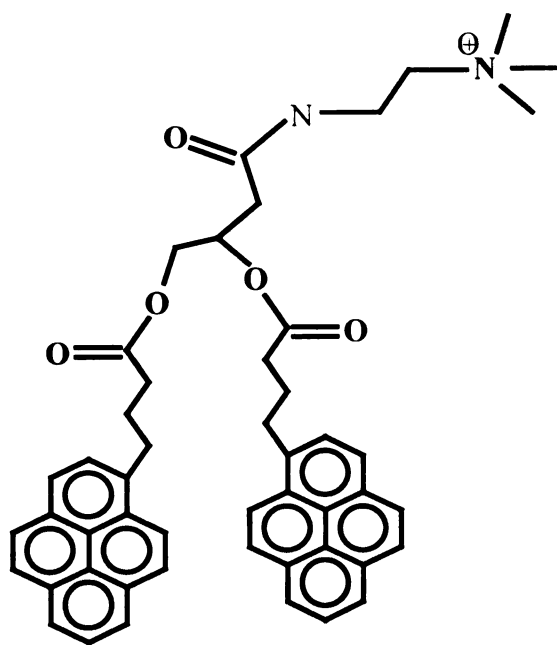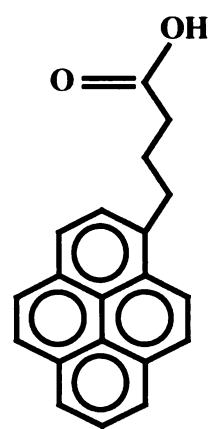
(A)   (B)

Figure 5.1. The chemical structures of dipy (A) and PBA (B).

nm (in diameter) filter (Avisten, Inc. Ottawa, ON) for about 19 times. The MLVs then became LUVs with uniform vesicle diameter (100 nm). Additional 2.0 ml of buffers was added in to make up enough solutions for fluorescence measurement. The solutions were clear by direct inspection. Background scattering measurement of the LUVs without probe is negligible.

3. Fluorescence Measurement

All of the fluorescence measurements were made on a FluoroMax-2 spectrofluorometer (Instruments S.A. Inc., NJ). The excitation for the emission spectra was set at 328 nm, the second vibrational band of the $S_0 \rightarrow S_2$ transition. The emission wavelength for excitation spectra was chosen at 374 nm, the 0-0 band of monomer emission. The excimer-to-monomer ratio (E/M) was the intensity ratio of the emission at 470 nm and 374 nm. The sample temperatures were regulated by a water bath (RTE-111, Neslab Instruments, Inc., Portsmouth, NH). The temperature was recorded by a Fluke 51 K/J thermocouple (John Fluke MFG Co., Everett, WA) inserted into a quartz cell just above the light path.

The fluorescence measurements in LUVs were made in atmospheric conditions. No degassing was carried out because the LUVs were not stable during the freeze-pump-thaw circles. Nitrogen gas bubbling into LUV solution caused huge data scattering. Fluorescence lifetime measurements showed that oxygen quenching efficiency to PBA was dramatically reduced comparing to pyrene. The lifetime of PBA in oxygen saturated aqueous solution is only about 10% less than the lifetime in oxygen free aqueous solution

(21). It is expected that the oxygen quenching effects on dipy should be similar to PBA. The oxygen quenching effects for dipy in DPPC LUVs should be further reduced because pyrene moieties are located in the hydrophobic aliphatic region (18, 22) and the concentration of oxygen in the hydrophobic region of lipid membrane is much less than the oxygen concentration in aqueous solution. Therefore, it is fairly safe to say that oxygen quenching effects on dipy in LUVs are quite small and the experimental error due to oxygen quenching is negligible.

DPPC LUVs alone showed no fluorescence in the range of interests. All of the spectra reported here were background subtracted.

Results

Figure 5.2 shows the fluorescence spectra of dipy and PBA when incorporated into DPPC LUVs with the same concentration of pyrene moieties (pyrene moiety : DPPC =1 : 500 in molar ratio). A strong excimer fluorescence is found with peak around 470 nm in the case of dipy but no excimer fluorescence in PBA. This indicates that excimer is formed intramolecularly instead of intermolecularly at such a low concentration.

DPPC LUVs with dipy probe were prepared in two different buffers with pH 4.7 (acetate buffer) and 6.9 (phosphate buffer). The ionic concentration of the two buffers was kept constant at 80 mM in order to observe the sole pH effects on excimer formation rate of dipy in DPPC LUVs. Figure 5.3A shows the excimer formation rate represented
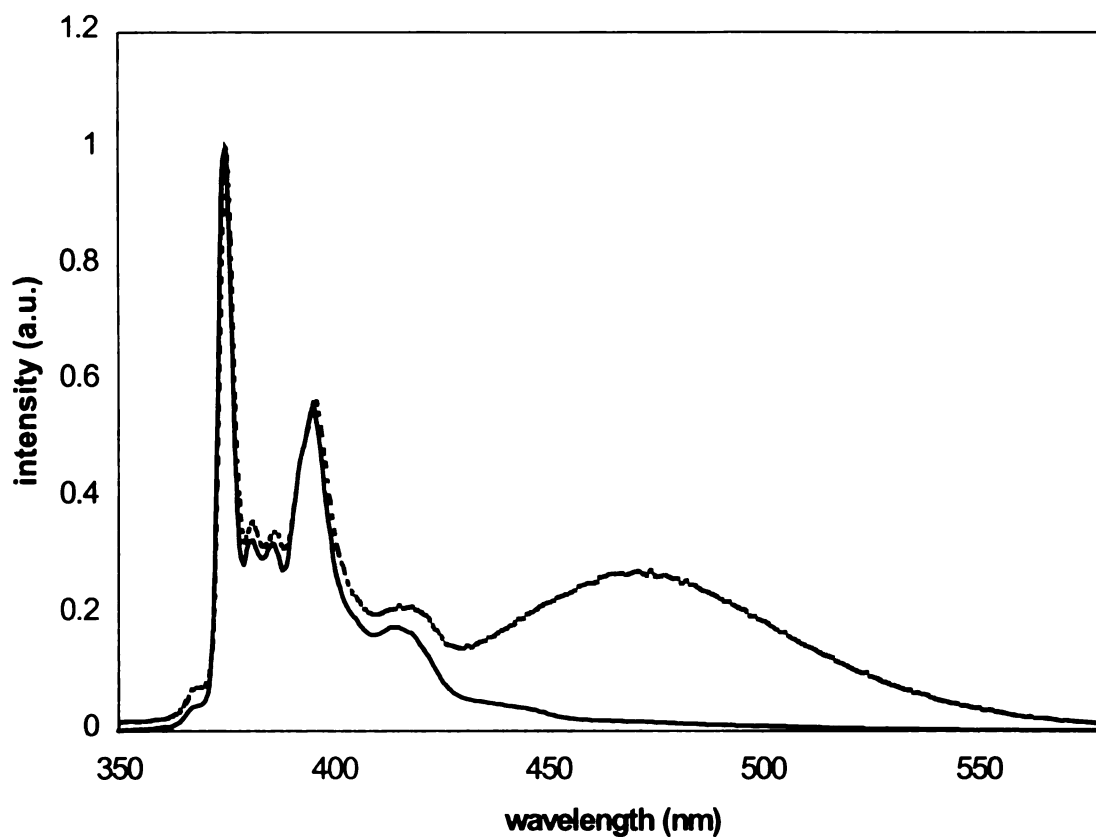
Figure 5.2. The normalized fluorescence spectra of dipy (dashed line) and PBA (solid line) in DPPC LUVs with pyrene moiety : DPPC = 1:500 (molar ratio); temperature: 20 ^{0}C; pH: 6.9. Note the strong excimer emission for dipy but no excimer emission for PBA.

by E/M ratio as a function of temperature. An abrupt increase in E/M ratio was found at ~ 42 ^{0}C, the known gel (L_β) to liquid crystalline (L_α) phase transition, for DPPC LUVs in both buffers. Even though DPPC at two pHs had the same main phase transition temperature, the absolute E/M ratios were remarkably different. At gel phase, E/M ratios were larger at pH 4.7 than those at pH 6.9. After passing the phase transition point, in which the E/M ratio was essentially same for both pHs, E/M ratios at pH 4.7 became smaller than those at pH 6.9. The net effect is that the E/M ratio change at phase transition at pH 4.7 is smaller than the change at pH 6.9. This observation is further illustrated in the first derivative plot of $\Delta(E/M)/\Delta t$ vs temperature as shown in Figure 5.3B. The peak positions for DPPC at two pHs are approximately same, at 42 ^{0}C. The peak area representing the enthalpy of the phase transition, however, is significantly different. By integrating the peak areas at two pHs, the enthalpy ratio from the fluorescence measurement is obtained as 1.42.

The DSC of DPPC MLVs in two buffers was performed as shown in Figure 5.3C. From Figure 3C, the phase transition temperature didn't change, but the enthalpy of the phase transition was significantly reduced at pH 4.7 comparing to the enthalpy at pH 6.9. Integrating the area of DSC thermograms at two pHs yields the enthalpy ratio 1.45, which is in excellent agreement with the ratio from fluorescence measurement. It is therefore concluded that the fluorescence measurement based on dipy not only accurately tells the lipid phase transition but also precisely shows the pH effects on the phase transition enthalpy.

Figure 5.3. (A) dipy in DPPC LUVs. Excimer-to-monomer ratio as a function of temperature; (B) the first derivative plot of E/M vs temperature; (C) the DSC scans of DPPC. Solid line: DPPC in pH 6.9 buffer; dashed line: DPPC in pH 4.7 buffer. Note that both fluorescence measurement and DSC show that the phase transition enthalpy is reduced by 1.4 times while the phase transition temperature remains unchanged.
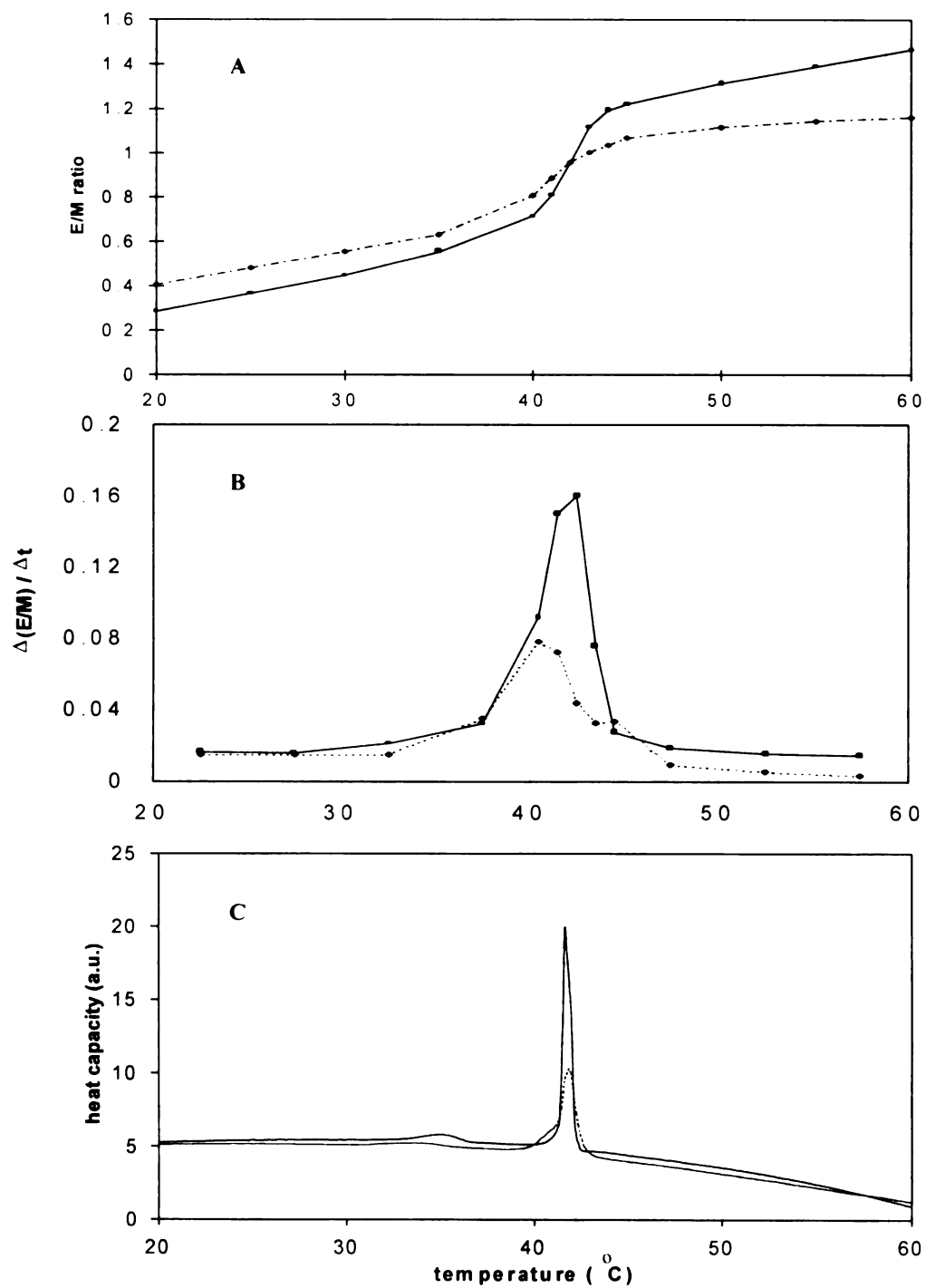
The mechanism for pyrene excimer formation was first proposed by Birks (14) and later modified by a number of investigators for the intramolecular excimer formation (15, 23). However, the applicability of the excimer formation mechanism in isotropic solvent into lipid membrane system was challenged by Suger etal (24, 25) and Cheng etal (18, 26). Based on the measurement of frequency-domain time-resolved fluorescence intensity decay, they modified the Birks' two-state collisional model to the so-called 3-state model by including an additional association state which is formed through translational or lateral diffusion. According to the 3-state model, the fitting of the frequency-domain data was improved over the 2-state model. Even though the 3-state model is very informative on physical concepts, the use of this model requires extensive analysis of time-resolved data. In addition, the curve fitting involves so many variables, which usually generates huge data uncertainties. For the sake of simplicity, Birks' two-state model is still used. It is believed that the two-state model is accurate enough for the apparent activation energy measurement in the following.

Upon light excitation, one pyrene moiety in dipy is excited. The excited and ground state pyrene moieties are brought together through translational diffusion and then reach a plane-parallel conformation through pyrene reorientation to form excimer. Therefore, the excimer formation rate is a function of membrane lateral and rotational mobility. The kinetics can be summarized in the following scheme:
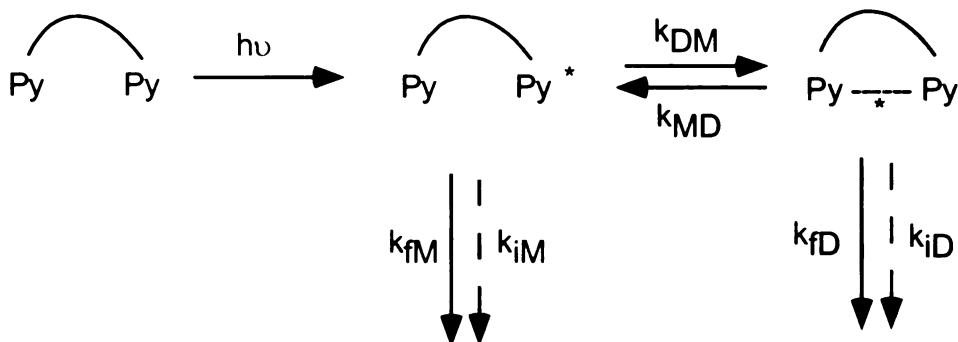
Py   Py $h\upsilon$ Py   Py * k_{DM} / k_{MD} Py ---- Py *

k_{fM} | k_{iM} k_{fD} | k_{iD}

where k_{fD} and k_{fM} represent the radiative rate constant of excimer and monomer; k_{iM} and k_{iD} are the radiationless rate constant of monomer and excimer; k_{DM} and k_{MD} are the rate constant for excimer formation and dissociation, respectively.

According to the above scheme, the excimer-to-monomer ratio (E/M) can be approximated in:

$$\frac{\phi_E}{\phi_M} = \beta \frac{E}{M} = \frac{k_{fD}}{k_{fM}} \times \frac{k_{DM}}{k_{MD} + k_{fD} + k_{iD}} \qquad (5.1)$$

where ϕ_E and ϕ_M are the quantum yield of excimer and monomer emission, resepctively; β is the proportionality constant relating the excimer-to-monomer quantum yield ratio (ϕ_E/ϕ_M) to excimer-to-monomer fluorescence intensity ratio (E/M). In Equation 5.1, k_{fD} and k_{fM} are independent of temperature and media (14). At low temperature and high viscosity (i.e., the aliphatic region of lipid membrane at gel state) (14, 23),

$$k_{MD} << k_{fD} + k_{iD} \tag{5.2}$$

In the low temperature range, k_{iD} can be considered as a constant (27, 28). Therefore, E/M ratio can be connected with the excimer formation rate in the following approximate equation (refer Chapter 4 for the detailed description about this approximation),

$$\frac{E}{M} = C \times k_{DM} = C \times A\exp(-E_0 / RT) \tag{5.3}$$

where $C = \dfrac{k_{fD}}{\beta k_{fM}} \times \dfrac{1}{k_{fD} + k_{iD}}$ is a constant in the low temperature range. From the plot of

$\ln(E/M)$ vs. 1/T (Figure 5.4), the apparent activation energy E_{app} is obtained as 22.1 kJ/mole at pH 4.7 and 32.7 kJ/mole at pH 6.9. The apparent activation energy at pH 6.9 is about 10 kJ/mole higher than the one at pH 4.7.

Discussion

The pH effects on DPPC can be understood as H^+ bonds to phosphate in DPPC, which then renders a net positive charge on lipid bilayer surface. The charge at membrane surface is not strong enough to affect phase transition temperature at least in the pH range studied. Previous experiments (2, 7, 29) have shown that the phase transition temperature of DPPC didn't change in the pH range of 3 to 9.
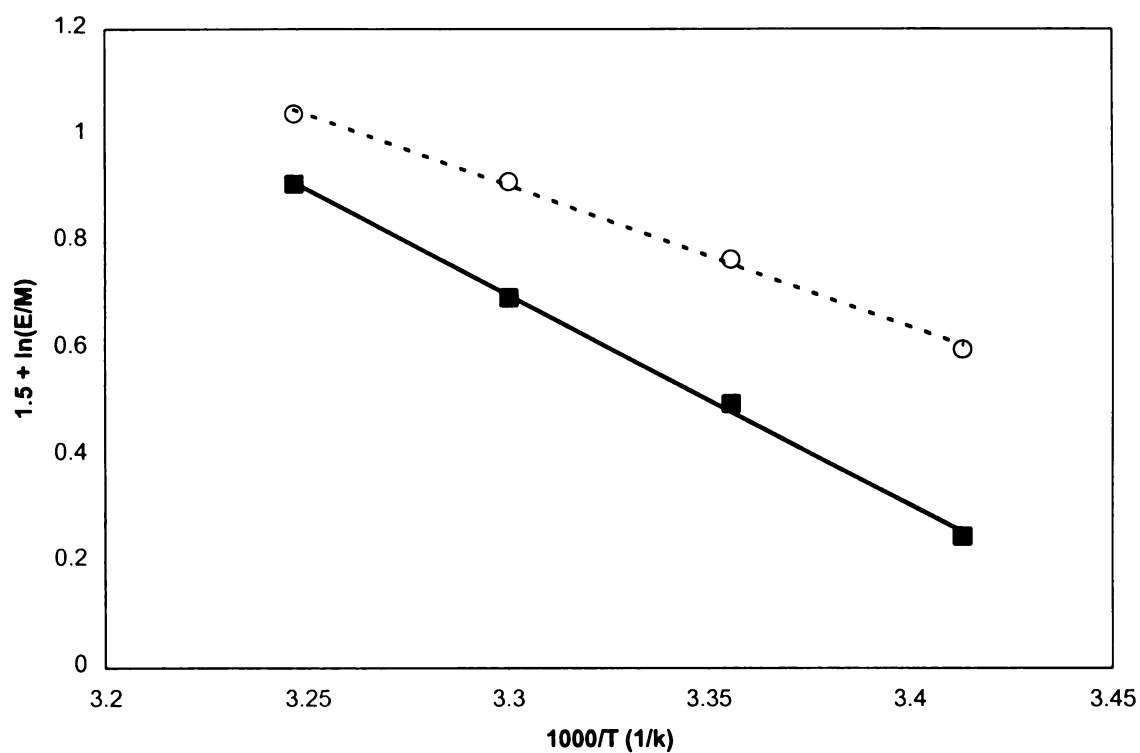
Figure 5.4. the apparent activation energy of dipy intramolecular excimer formation in DPPC gel phase. Solid line: DPPC in pH 6.9 buffer, E_{app} = 32.7 kJ/mole; Dashed line: DPPC in pH 4.7 buffer, E_{app} = 22.1 kJ/mole.

However, the charge at membrane surface does change and normally reduces the phase transition enthalpy ΔH and consequently change the phase transition entropy ΔS (i.e., $\Delta S = \Delta H / T_m$ for first-order phase transition, where T_m is the main phase transition temperature). One of the contributions to the enthalpy reduction is the electrical double layer energies (ΔΓ) as proposed by Trauble et. al. (2, 30). If there is no net surface charge such as DPPC at pH 6.9, ΔΓ = 0. However, for DPPC at pH 4.7, due to net surface charge (2, 30),

$$\Delta\Gamma = \Gamma(L_\alpha) - \Gamma(L_\beta) = -2RT \times \frac{f_\alpha - f_\beta}{f_\alpha} \times \frac{\sigma'}{e} \qquad (5.4)$$

R, T and e are gas constant, temperature in Kelvin and electronic charge respectively. f_α and f_β are the lipid mean molecular area in the liquid crystalline (L_α) and gel state (L_β) respectively. σ' is the charge per lipid polar group. For DPPC, $f_\alpha = 70$ Å², $f_\beta = 48$ Å² (7). If we assume σ' = 1, at DPPC main phase transition temperature (42 ^{0}C), ΔΓ = -1.7 kJ/mole, the highest possible contribution from the electrical double layer energy.

The total ΔH is the sum of a non-electrostatic term ΔH^0 and ΔΓ. The negative ΔΓ signifies that the phase transition enthalpy is reduced due to charged lipid membrane. However, our experimental data showed that the amount of enthalpy reduction is about 10 kJ/mole. The reduction due to charge only accounts a small fraction of total reduction.

The second contribution to the enthalpy reduction has been proposed by Jacobson and Papahadjopoulos (3) based on their DSC measurement. They believed that the net surface charge not only affected the electrical properties of lipid bilayer but also produced the structural alterations in lipid aliphatic region and causes a "disordering" effect particularly in membrane gel phase. This disordering effect then resulted in a reduction of ΔH and consequently ΔS (i.e.: for a first order phase transition, $\Delta G = 0$, $\Delta S = \Delta H/T$). The net surface charge altering aliphatic chain motion has been reported previously. For DMPA at different pHs, Raman spectra of C-C stretch vibration has shown the electrostatically induced changes of internal chain conformation (32). Michaelson etal (33) studied the pH effects on ^1H NMR of phosphatidylethanolamine (PE). They found that the peak intensity and peak sharpness of methylene and methyl protons were increased with pH. This observation was interpreted as the repulsive force due to negative charge of lipid head group at high pH increased aliphatic chain motion. X-ray study of DHPA showed that the repulsive force due to net surface charge at high pH caused lateral expansion at bilayer surface, which then increased lipid chain tilt angle (34).

In our experiment, the pyrene moieties of dipy are sitting in the middle of aliphatic chain region of DPPC by comparing the chain length of dipy with DPPC. The E/M ratio is therefore very sensitive to the surface charge induced alteration of chain motion. At gel phase, the lipid mean molecular area of DPPC is 48 Å^2 (7). Lipids in this phase are tightly packed. The pyrene moieties in dipy are in close contact. Re-orientation of the pyrene moieties is the only motion necessary that leads to the excimer formation

(35). Therefore, rotational diffusion rate of pyrene determines the E/M ratio. The higher E/M ratios in gel phase at pH 4.7 (Figure 5.3A) indicate that repulsive force due to positive charge at lipid head group increases the aliphatic chain motion and consequently the chain rotational mobility. In liquid-crystalline phase, the lipid mean molecular area of DPPC is significantly increased to 70 $\mathring{A}^2$ (7). In this case, the average chain separation is 4.7 $\mathring{A}$. Comparing to excimer inter-pyrene distance of 3.5 $\mathring{A}$ (19), it is expected that both rotational diffusion and translational diffusion participate in the intramolecular excimer formation. The further increase of mean area due to electrostatical repulsion gives the pyrene moieties too much available conformational space or free volume (36). The pyrene moieties will spend longer time to attain the suitable conformation for excimer formation at pH 4.7 than at pH 6.9. The excimer formation rate or E/M ratio at pH 4.7 is therefore lower than the ratio at pH 6.9 as shown in Figure 5.3A. Cheng et al (18) reported the excimer formation rate of dipyrenyl PC with variable chain length ($dipy_nPC$) decreased with chain length. They interpreted the rate decrease as the increase of available conformational space or free volume with increase of lipid chain length. The E/M ratio increases in the gel phase and decreases in the liquid crystalline phase at pH 4.7, rendering less E/M ratio change during DPPC phase transition and therefore a reduced phase transition enthalpy. We believe the reduction in enthalpy at pH 4.7 is mostly due to the effects of membrane surface charge on lipid chain motion or mobility.

The additional evidence about surface charge affecting lipid chain motion or ordering comes from the apparent activation energy measurement (Figure 5.4). The apparent activation energy includes two parts: E_0, intrinsic energy barrier associated with

bond rotation and E_η, activation energy due to media viscous flow related to media friction force exerted on the bond rotation in the process of intramolecular excimer formation. The media viscosity effects on excimer formation rate can be expressed in the following equation (37, 38):

$$k_{DM} = A\eta^{-\alpha} \exp(-E_0 / kT) \qquad (5.5)$$

where A is a viscosity-independent constant and E_0 is the intrinsic activation energy barrier. k is the Boltzmann constant and T is the temperature in Kelvin. The exponent α is in the range of $0.1 \leq \alpha \leq 1$, which is the measure of the relative importance of the viscosity. Our previous experiments (38) showed that α value is 0.80 ± 0.02 and E_0 is 7.3 kJ/mole when dipy is in solvent mixture of acetonitrile and PEG 600.

Since the Equation 5.5 is appropriate for excimer formation in liquids, it is necessary to find the evidence that it is also valid in lipid membranes, especially in the membrane hydrocarbon region. I begin the discussion with lipid motional dynamics. It is generally believed that there are six common motions in lipid membrane: lateral diffusion, wobbling diffusion, axial rotational diffusion, chain flexibility, director fluctuation and flip-flop (39). Within the fluorescence lifetime scale, the first four types of motions are important.

Lateral diffusion describes how lipids migrate across the surface of the membrane. This motion is random, that is, displacement occurs in all directions with

equal probability. The relevant parameter to characterize this motion is the lateral diffusion constant, D_L, which is the squared displacement per second, normally in the unit of $\mu m^2/s$. The most common technique to obtain the lateral diffusion constant is the fluorescence recovery after photobleaching (FRAP) (40). The FRAP experiment works first to irreversibly bleach fluorophores by a small intense laser beam and then monitor the fluorescence intensity recovery. The time for the recovery is a function of membrane lateral diffusion constant.

Rotational diffusion includes wobbling motion with diffusion constant D_w and axial rotation with diffusion constant D_R. The axial rotation is the rotation around the lipid optical axis while the wobbling ration is about an axis perpendicular to lipid optical axis. Because of the lipid anisotropic or ordering properties, the rotation about the axis perpendicular to lipid optical axis is not a free rotation, that is, lipids can not tumble freely. Instead, lipids are described as wobbling in a cone. The most common technique to obtain the diffusion constants, D_w or D_R, is fluorescence depolarization (41). The most common membrane probe to study membrane wobbling motion is 1,6-diphenyl-1,3,5-hexatriene (DPH) which is a rod-shaped molecule sitting in the membrane hydrophobic chain region. The wobbling diffusion constant D_w for a rod-shaped probe like DPH embedded in membrane can be obtained by the following approximated equation (41, 62):

$$\frac{r(t)}{r(0)} = A_x + (1 - A_x)\exp(-D_w t / <\sigma>) \qquad (5.6)$$

with,

$$A_r = \frac{r(\infty)}{r(0)} \tag{5.7}$$

$$<\sigma> = \sum_{i \neq r} A_i \sigma_i / (1 - A_r) \tag{5.8}$$

where r(t), r(∞) and r(0) are the fluorescence anisotropy at time t, ∞ and 0 respectively. A_i and σ_i are constants which depend only on cone angle.

However, rotation about DPH long axis does not displace the emission dipole and hence does not depolarize the emission. Therefore, the axial rotational constant D_R can not be obtained by DPH fluorescence depolarization experiment. For large integral proteins that have negligible wobbling, the rotational diffusion can be described by Saffman-Delbrück equation (63) in which proteins are treated as a Brownian particle in biological membrane. The equation was then extended by Jähnig (64) to relate the axial rotational diffusion constant D_R with membrane microviscosity η:

$$D_R = \frac{kT}{2\pi\eta h(a^2 + b^2)} \tag{5.9}$$

where h is the lipid bilayer thickness. a and b are the protein radius along one axis and the other.

Lipid chain flexibility or the internal dynamics mainly deals with the trans-gauche isomerizations of lipid hydrocarbon chains. This type of motions can be studied with

NMR (42, 43), ESR (44) and fluorescence depolarization (45). An alternative technique to study lipid chain flexibility is through the intramolecular excimer formation of dipyrenyl probe. This technique has gained popularity recently with the advantages described in the introduction section. The intramolecular excimer is formed through lipid chain trans-gauche isomerizations to reach an optimum excimer conformation. This isomerization process involves a swing of pyrene moieties. The friction experienced in the course of swing can be decomposed into two parts: translational drag and pure rotational drag of pyrene moieties around the pyrene long axis (37, 46). When the coupling between rotational and translational friction is zero (47), the total friction is the sum of the two contributions.

At this point, it is important to remember that the information based on fluorescence is at different level from that based on NMR. The NMR is to analyze the movement of each atom or segment in lipid chains. The resulting lipid chain mobility is different at the different position of a given lipid chain. The information obtained by NMR is therefore at microscopic level. For fluorescence, a foreign probe is introduced into a membrane organization. The probe, by its spontaneous distribution and movement, averages out most of the microscopic details and therefore reports the information about lipid mobility at submacroscopic level (60). In addition, NMR as a nonperturbing technique in principle produces more reliable information than the fluorescence because the fluorescence probe is essentially an impurity and therefore perturbs the original membrane organization. However, the perturbation can be minimized substantially by introducing very small amount of probe such as the dipy probe used in this study.

Besides, useful information is transmitted through the boundaries of the regions where probes is localized, and thus probes are sensitive to the ordering, changes in mobility and other physical events. The structure differences between probes and the components of lipid membranes do not necessarily reduce the useful information obtained from fluorescence experiments (61).

Comparing the motions in anisotropic membranes with the motions in isotropic liquids, the most significant difference is the wobbling rotational diffusion. Molecules can tumble freely in liquids while wobble in membranes due to the restriction from ordered lipids. However, the wobbling motion in membrane will not affect the intramolecular excimer formation because the excimer formation is determined primarily by the closeness and the orientation of pyrene moieties. The evidence to support this statement comes from the fluorescence depolarization experiment in which DPH is incorporated into DPPC vesicles. It has been found that the wobbling diffusion constant, D_w, depends solely on temperature, not on phase transition temperature nor on order parameters (39, 48, 49). It is well known that lipid chain flexibility strongly depends on membrane phase transition (50). Therefore, this experimental observation indicates that there is no or weak coupling between the wobbling motion and lipid chain flexibility. Theoretical calculation (51) also indicates that the coupling between the internal motion and wobbling motion of lipid chain is negligible.

The findings that D_w doesn't depend on membrane phase transition temperature or order from the fluorescence depolarization experiment also indicate that the internal

dynamic motion in a bilayer is very similar to that of a neat alkane liquid. This observation from fluorescence measurement has been supported by spin-lattice (T_1) relaxation of ^2H (52, 53), ^{13}C (52, 54) and ^{14}N (53) in DPPC bilayers. From the experimental data as well as the theory of spin-lattice relaxation in lipid bilayers, they concluded that the microviscosity of the bilayer hydrocarbon region is not appreciably different from that of paraffinic liquids. Stochastic simulation of DPPC performed by Pastor, Karplus and et al (51, 55) further asserted that the internal dynamics or trans-gauche isomerization of a hydrocarbon chain in a bilayer is very similar to that of hydrocarbon liquids. The orientational freedom of the lipid chain manifested by the wobbling motion and nonzero order parameters has only a small effect on the local motion such as trans-gauche isomerization which is important on intramolecular excimer formation.

So far, I have shown that lipid chain wobbling motion does not affect lipid chain trans-gauche isomerization and the lipid chain flexibility or internal dynamics of lipid hydrocarbon chains is very similar to that of liquids. The further evidence is from the experiment performed by Hara and et al (16, 56). They incorporated the 1,3-di(1-pyrenyl) propane (DPP) into micelle, an ordered system. They found out that the experimental data could be fully fitted by Kramers' theory, just like in isotropic liquids (23, 57). They further estimated the intramicellar viscosity based on Kramers relationship between the excimer formation rate and solvent viscosity.

Based on the above experimental data and theoretical calculations, Equation 5.5 which describes chromophore trans-gauche isomerization process in liquids should be valid in lipid hydrocarbon region since the motion in liquids is very similar to that in lipid hydrocarbon region. From Equation 5.5,

$$E_{app} = -R\frac{\partial \ln(k_{DM})}{\partial(1/T)} = \alpha R\frac{\partial \ln \eta}{\partial(1/T)} + E_0 \qquad (5.10)$$

The change of η with temperature was described in a simple exponential form (58, 59)

$$\eta = A\exp(E_\eta / RT) \qquad (5.11)$$

where E_η is the activation energy due to viscous flow in simple liquids and fusion activation energy in membranes (58, 59). Combining Equations 5.10 and 5.11 yields

$$E_{app} = \alpha E_\eta + E_0 \qquad (5.12)$$

To the first approximation, α and E_0 are same for DPPC LUVs in different buffers. The difference in E_{app} is thus due to E_η. The lower E_{app} means the lower E_η at pH 4.7. According to Equation 5.11, the lower E_η renders lower viscosity at pH 4.7 than at pH 6.9. The lower viscosity indicates that the lipid chains have faster motions at pH 4.7 than the well organized all-trans aliphatic chains at pH 6.9, where the net surface charge and

140

consequently the repulsive force is absent. Therefore, the net surface charge indeed caused a disordering effects in gel phase as Jocobson and Papahodjopolous proposed (3).

At liquid crystalline state, the assumption that $k_{MD} \ll k_{fD} + k_{iD}$ and k_{iD} is a constant becomes questionable at the elevated temperature. E/M ratio may not represent k_{DM}, the rate constant for intramolecular excimer formation. But comparing the slope flatness of ln (E/M) vs 1/T as shown in Figure 5.5, we can still tell the apparent activation energy at pH 4.7 is lower than the energy at pH 6.9. This observation further indicates that net charge on membrane surface increases lipid mobility and decreases membrane microviscosity at both gel phase and liquid crystalline phase.

Conclusion

In this report, dipy as a membrane probe has been exploited. As one specific example, dipy is incorporated into DPPC large unilamellar vesicles (LUVs) under two different buffers with pH 4.7 and 6.9. The measurement of excimer-to-monomer ratio (E/M) as a function of temperature shows that the low pH significantly reduces the enthalpy of main phase transition while phase transition temperature remains unchanged. This observation based on fluorescence measurement is in excellent agreement with DSC result. The pH effects on phase transition enthalpy of DPPC can be understood as H^+ bonding to phosphate at low pH renders net membrane surface charge. Because intramolecular excimer formation in dipy is sensitive to lipid chain motion, the detailed
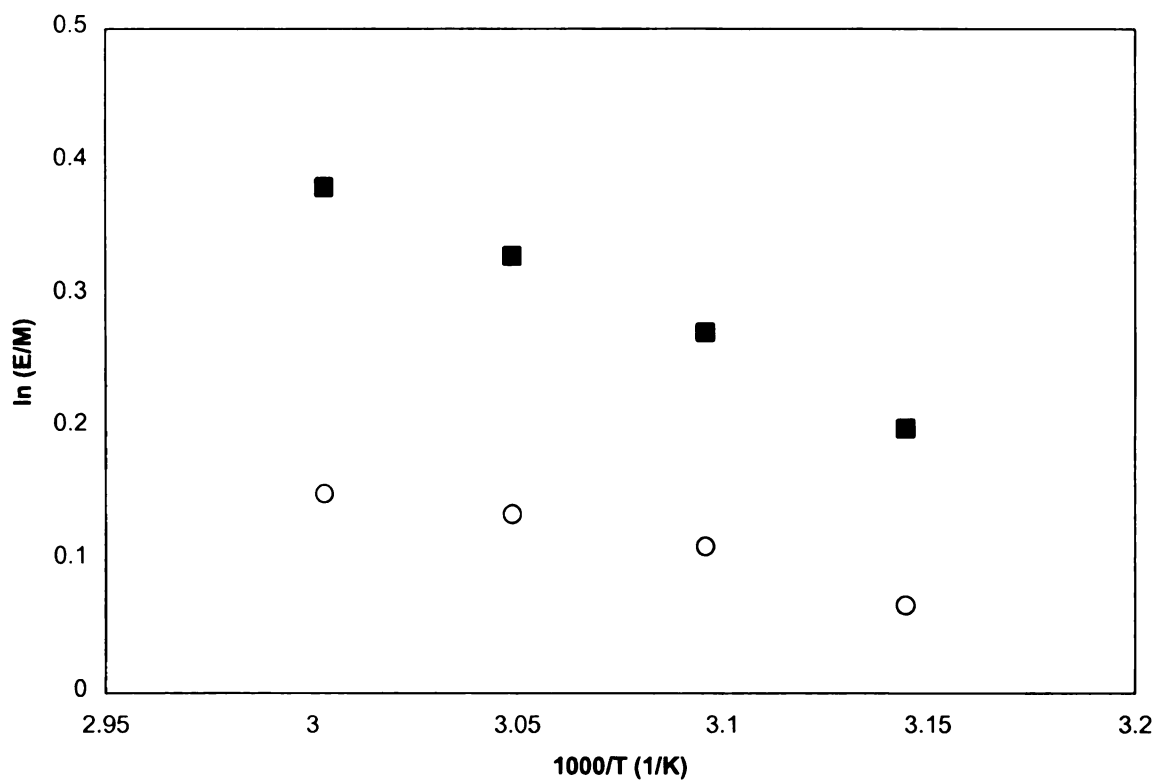
Figure 5.5. the plot of ln (E/M) vs 1/T at DPPC liquid crystalline. Solid square: DPPC in pH 6.9 buffer; open circle: DPPC in pH 4.7 buffer. The plot doesn't yields a straight line because the assumptions, $k_{MD} \ll k_{fD} + k_{iD}$ and k_{iD} independent of temperature, are no longer valid at the elevated temperature. But comparing the trend of the plot flatness, one can still tell the apparent activation energy at pH 4.7 is less than the energy at pH 6.9.

analysis of E/M ratio clearly indicates that the charge at membrane surface increases lipid chain mobility especially in gel phase. The apparent activation energy of dipy intramolecular excimer formation shows that the microviscosity of DPPC at pH 4.6 is lower than the one at pH 6.9. The decrease of microviscosity at lower pH is a direct consequence of the increase in lipid chain mobility.

Reference

1. Cevc, G. *Biochemistry* **1987**, 26, 6305

2. Träuble, H.; Eibl, H. *Proc. Nat. Acad. Sci. USA* **1974**, 71, 214

3. Jacobson, K.; Papahadjopoulos, D. *Biochemistry* **1975**, 14, 152

4. Blume, A.; Eibl, H. *Biochim. Biophys. Acta* **1979**, 558, 13

5. MacDonald, R. C.; Simon, S. A.; Baer, E. *Biochemistry* **1976**, 15, 885

6. Koynova, R. D.; Tenchov, B. G.; Kuttenreich, H.; Hinz, H.-J. *Biochemistry*, **1993**, 32, 12437

7. Fernández, M. S.; González-Martinez, M. T.; Calderón, W *Biochim. Biophys. Acta* **1986**, 863, 156

8. Koynova, R. D.; Tenchov, B. G.; Quinn, P. J.; Laggner, P. *Chem. Phys. Lipids* **1988**, 48, 205

9. Galla, H.-J.; Hartmann, W.; Theilen, U.; Sachmann, E. *J. Membr. Bio.* **1979**, 48, 215

10. Somerharju, P. J.; Virtanen, J.A.; Edlund, K. K.; Vainio, P.; Kinnunen, P. K. J. *Biochemistry* **1985**, 24, 2773

11. Wiener, J. R.; Pal, R.; Barenholz, Y.; Wagner, R. R. *Biochemistry* **1985**, 24, 7651

12. Eisinger, J; Flores, J.; Petersen, W. P. *Biophys. J.* **1986**, 49, 987

13. Caruso, F.; Grieser, F.; Thistlethwaite, P. J.; Almgren M. *Biophys. J.* **1993**, 65, 2493

14. Birks, J. B. *Photophysics of Aromatic Molecules;* Wiley Interscience: New York, 1970; Chapter 7

15. Zachariasse, K. A. *Chem. Phys. Lett.* **1978**, 57, 429

16. Hara, K.; Suzuki, H. *J. Phys. Chem.* **1990**, 94, 1079

17. Vauhkonen, M.; Sassaroli, M.; Somerharju, P.; Eisinger, J. *Biophys. J.* **1990**, 57, 291

18. Cheng, K. H.; Ruymgaart, L.; Liu, L.-I.; Somerharju, P.; Sugar, I. P. *Biophys. J.* **1994**, 67, 902

19. De Schryver, F. C.; Collart, P.; Vandendriessche, J.; Goedeweeck, R.; Swinnen, A.; van der Auweraer, M. *Acc. Chem. Res.* **1987**, 20, 159

20. Huang, G. F.; Hollingsworth R.I. *Tetrahedron* **1998**, 54, 1355

21. Blanchard, G. J. *private communication*

22. Sunamoto, J.; Kondo, H.; Nomura, T.; Okamoto, H. *J. Am. Chem. Soc.* **1980**, 102, 1146

23. Hara, K.; Yano, H. *J. Am. Chem. Soc.* **1988**, 110, 1911

24. Sugar, I. P.; Zeng, J. W.; Vauhkonen, M.; Somerharju, P. *J. Phys. Chem.* **1991**, 95, 7516

25. Sugar, I. P.; Zeng, J. W.; Chong, P. L.-G. *J. Phys. Chem.* **1991**, 95, 7524

26. Cheng, K. H.; Ruymgaart, L.; Liu, L.-I.; Somerharju, P.; Sugar, I. P. *Biophys. J.* **1994**, 67, 914

27. Goldenberg, M.; Emert, J. Morawetz., H. *J. Am. Chem. Soc.* **1978**, 100, 7171

28. Melnick, R. L.; Haspel, H. C.; Goldenberg, M.; Greenbaum, L. M.; Weinstein, S. *Biophys.J.* 34, 499

29. Papahadjopoulos, D. *Biochim. Biophys. Acta* **1968**, 163, 240

30. Träuble, H.; Teubner, M.; Woolley, P.; Eibl, H. *Biophys. Chem.* **1976**, 4, 319

31. Chen, S. C.; Sturtevant, J. M.; Gaffney, B. J. *Proc. Natl. Acad. Sci. U.S.A.* **1980**, 77, 5060

32. Vogel, H.; Stockburger, M.; Träuble, H. *Proc. Intl. Conf. Raman Spectrosc. 5th*, **1976**, 176

33. Michaelson, D. M.; Horwitz, A. F.; Klein, M. P. *Biochemistry*, **1974**, 13, 2605

34. Jähnig, F.; Harlos, K.; Vogel H.; Eibl, H. *Biochemistry*, **1979**, 18, 1459

35. Lemmetyinen, H.; Yliperttula, M.; Mikkola, J.; Virtanen, J. A.; Kinnunen, P. K. J. *J. Phys. Chem.* **1989**, 93, 7170

36. Cheng, K. H.; Chen, S.-Y.; Butko, P.; Wieb van der Meer, B.; Somerharju, P. *Biophys. Chem.* **1991**, 39, 137

37. Bagchi, B. *Intl. Rev. Phys. Chem.* **1987**, 6, 1

38. Du, X. Y.; Hollingsworth, R. I. *Manuscript in Preparation*

39. Van der Meer, B. W. in *Biomembrane, Physical Aspects* Shinitzky, M. (Ed.); Ch. 4; **1993**, VCH: Weinheim, New York

40. Henis, Y. I. in *Biomembrane, Physical Aspects* Shinitzky, M. (Ed.); Ch. 6; **1993**, VCH: Weinheim, New York

41. Lipari G.; Szabo, A. *Biophys. J.* **1980**, 30, 489

42. Meier, P.; Ohmes, E.; Kothe, G. *J. Chem. Phys.* **1986**, 85, 3598

43. Rommel, E.; Noack, P.; Meier, P.; Kothe, G. *J. Phys. Chem.* **1988**, 92, 2981

44. Meier, P.; Blume, A.; Ohmes E. *Biochemistry* **1982,** 21, 526

45. Kutchai, H.; Chandles, L. H.; Zavoico, G. B. *Biochim. Biophys. Acta* **1983,** 736, 137

46. Akesson, E.; Sundstrom, V.; Gillbro, T. *Chem. Phys.* **1986,** 106, 269

47. Happel, J.; Brenner, H. *Low Reynolds Number Hydrodynamics* **1965,** Prentice Hall: Englewood Cliffs

48. Ameloot, M; Hendrickx, H; Herreman, W.; van Cauwelaert, F.; van der Meer, W. *Biophys. J.* **1984,** 46, 525

49. Kawato, S.; Kinosita, K.; Ikegami, A. *Biochemistry* **1977,** 16, 2319

50. Lange, A.; Marsh, D.; Wassmer, K.-H.; Meier, P.; Kothe, G. *Biochemistry* **1985,** 24, 4383

51. Pastor, R. W.; Venable, R. M.; Karplus, M.; Szabo, A. *J. Chem. Phys.* **1988,** 89, 1128

52. Brown M. F.; Ribeiro, A. A.; Williams, G. D. *Proc. Natl. Acad. Sci. USA* **1983,** 80, 4325

53. Brown, M. F. *J. Chem. Phys.* **1982,** 77, 1576

54. Sefcik, M. D.; Schaefer, J.; Stejskal, E. O.; McKay, R. A.; Ellena, J. F.; Dodd, S. W.; Brown, M. F. *Biophys. J.* **1983,** 41, 282a

55. Pastor, R. W.; Venable, R. M.; Karplus, M. *J. Chem. Phys.* **1988,** 89, 1112

56. Hara, K.; Suzuki, H.; Takisawa, N. *J. Phys. Chem.* **1989,** 93, 3710

57. Hara, K.; Akimoto, S.; Suzuki, H. *Chem. Phys. Lett.* **1990,** 175, 493

58. Shinitzky, M.; Dianoux, A.-C.; Gitler, C.; Weber, G. *Biochemistry* **1971,** 10, 2106

59. Cogan, U.; Shinitzky, M.; Weber, G.; Nishida, T. *Biochemistry* **1973,** 12, 521

60. Shinitzky, M. *Physiology of Membrane Fluidity,* Vol. I (Shinitzky, M. ed.); CRC Press: Boca Raton, FL; Chapter 1, 1984

61. Azzi, A. *Quart. Rev. Biophys.* **1975,** 8, 237

62. Kinoita, K.; Kawato, S.; Ikegami, A. *Biophys. J.* **1977,** 20, 289

63. Saffman, P. G.; Delbrück, M. *Proc. Nat. Acad. Sci. USA* **1975,** 72, 3111

64. Jähnig, F. *Eur. Biophys. J.* **1986,** 14, 63

Chapter 6

Probing the Reaction Dynamics in Solution Phase Through

Intramolecular Excimer Formation

Introduction

Most of the chemical and biological reactions occur in liquid solution phase. However, the reaction in liquid phase is far less understood than the reaction in gas phase due to the complex solvent effects on reaction. Within many classes of chemical reactions in liquid phase, isomerization reaction in solution provides a unique way to study how solvent properties affect reaction dynamics due to relative simple reaction mechanism and potential surface (1). Of particular interest are the solvent frictional forces on the rate of isomerization reaction in solution. Kramers (2) in more than half century ago first modeled the reactive motion as the passage of Brownian particle over a one-dimensional barrier, which is described by an ordinary Langevin equation. By solving the steady-state Fokker-Planck equation, Kramers derived a simple and elegant equation for the reaction rate constant:

$$k = \frac{\omega_R}{2\pi\omega_b} \times [(\frac{\zeta^2}{4} + \omega_b^2)^{1/2} - \frac{\zeta}{2}]\exp(-E_0 / k_B T) = \kappa_{KR} \times k_{TST} \qquad (6.1)$$

Where,

$$k_{TST} = \frac{\omega_R}{2\pi}\exp(-E_0 / k_B T) \qquad (6.2)$$

is the rate constant deduced from transition state theory (TST) with ω_R, vibrational frequency in the reactant well; E_0, the intrinsic activation energy of the one-dimensional surface; k_B, the Boltzmann constant.

$$\kappa_{KR} = \frac{1}{\omega_b} \times [(\frac{\zeta^2}{4} + \omega_b^2)^{1/2} - \frac{\zeta}{2}] \qquad (6.3)$$

is the Kramers' transmission coefficient, which explicitly tells how solvent friction force influences the reaction rate in solution phase. ζ is the zero-frequency friction parameter, ω_b is the imaginary frequency at activation barrier region.

In the high friction limit where $\zeta \gg 2\omega_b$,

$$\kappa_{KR} = \frac{\omega_b}{\zeta} \qquad (6.4)$$

Therefore, the reaction rate constant is inverse proportional to solvent friction force. By assuming the simple hydrodynamic relationship between ζ and solvent viscosity η, the rate constant is then inverse proportional to η, which corresponds to Smoluchowski limit (3). However, many experimental results on photochemical isomerization of dye molecules in solution (1, 4-11) have shown that the reciprocal viscosity dependence of the rate constant is not obeyed. Instead, a fractional viscosity dependence of the rate constant was observed.

$$k = A\eta^{-\alpha}\exp(-E_0 / k_B T) \qquad\qquad (6.5)$$

A is the viscosity-independent pre-exponential factor. The exponent α is typically between zero and unity.

Theoretical and experimental work has attributed the deviation from Kramers theory to the following four factors:

(1) In Kramers model, the friction force that rotating moieties experienced is macroscopic zero-frequency friction force. For sharp activation barriers where vibrational frequency ω_b is comparable to or larger than solvent vibrational frequency (bath correlation time), the reactant doesn't stay at the barrier long enough to probe all of the solvent motions. The frictional forces that are exerted on the rotating moieties are therefore vibrational frequency dependent and the forces are less than the zero-frequency frictions (9, 11-13).

(2) In many realistic situations, the size of isomerizing molecule is comparable to that of solvent molecules. In such cases, Kramers' approach of treating reactant as Brownian particle is not justified. (14-17).

(3) The potential surface of reaction is solvent dependent (18-20).

(4) Kramers treatment is one-dimensional. In isomerization reaction, the reactive mode may be coupled to other non-reactive modes (21-24).

The molecular motions of isomerization reaction in which isomer is formed through translational and rotational diffusion of chromophore around a chemical bond are same as the motions of intramolecular excimer formation. Therefore, intramolecular excimer formation is one special type of isomerization reactions. The advantage of using pyrene excimer formation to study reaction dynamics in solution phase is that pyrene and pyrene excimer have very long lifetime and very high quantum yield. The excimer emission is red-shifted and well separated from monomer emission, which enables monomer and excimer intensity to be measured with high accuracy (25). Under reasonable assumptions, excimer-to-monomer ratio (E/M) can represents the intramolecular excimer formation rate (26). Therefore, a simple steady-state fluorescence spectroscopy can be used to study reaction dynamics in solution phase, which usually utilizes ultrafast time-resolved fluorescence spectroscopy.

The typical examples of probing reaction dynamics in solution phase through intramolecular excimer formation are 1, 3-di(2-naphthyl) propane (DNP) (27) and 1, 3-di(1-pyrenyl) propane (DPP) (28). Because only four bonds are between two fluorophore moieties, it is believed that a single gauche-trans rotation will lead to excimer formation (29, 30). Therefore, DNP and DPP are excellent probes for testing the utility of Kramers one-dimensional barrier-crossing model. Indeed, they found that viscosity was well fitted by the full Kramers equation.

A dipyrenyl probe synthesized in this laboratory (31) has thirteen bonds between two pyrene moieties. It's therefore expected that there are many non-reactive modes

besides one reactive mode. Hynes and his co-workers have developed the multi-dimensional expansion of Kramers theory (21, 22). They proposed that mode coupling especially in high viscosity region results in an enhancement of the reaction rate constant. This enhancement can be understood as a biasing of reaction in the direction of minimum friction. In this report, we first study the temperature dependence of fluorescence behavior in different solvent mixtures and discuss the photophysics behind the reasonable assumptions used throughout this report. We then attempt to provide direct evidence that mode coupling enhances reaction rate in the diffusive limit through the detailed analysis of the excimer formation rate as a function of solvent viscosity.

Materials and Methods

1. Chemicals

The probe synthesis was reported early (31). The purity of the probe was checked by TLC (4 : 1 CH_3Cl : CH_3OH). The structure of the dipy probe is shown in Figure 6.1. All of solvents were of Spectra AR grade and used without further purification.

2. Solvent Viscosity Measurement

Solvent viscosity was varied by mixing different ratios of acetonitrile and PEG 600 (polyethylene glycol with average molecular weight 600, from Sigma, MO). The kinematic viscosity of the solvent mixtures was determined with Cannon-Fenske viscometers (Ace Glass, Vineland, NJ) which were thermostated in 50:50 ethylene glycol : water bath controlled by Neslab RTE-111 (Portsmouth, NH). The densities of the solvent mixtures at different temperature were determined by specific gravity bottles
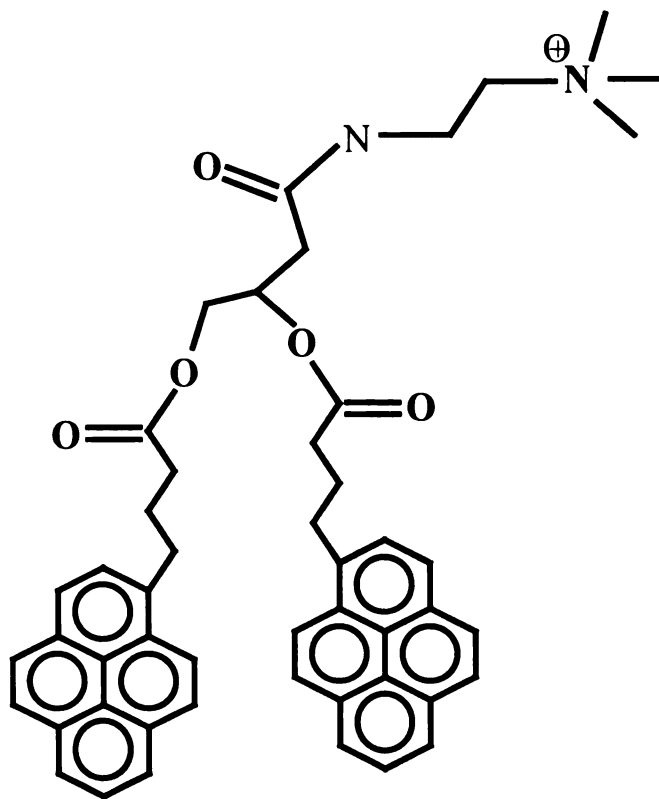
Figure 6.1. The chemical structure of the dipyrenyl membrane probe (dipy).

(Ace Glass, Vineland, NJ). The absolute viscosity was then the product of kinematic viscosity and solvent density.

3. Fluorescence Measurement

All of the fluorescence measurements were made on FluoroMax-2 (Instruments S.A. Inc., NJ). The excitation for the emission spectra was set at 326 nm, the second vibrational band (0-1) of the $S_0 \rightarrow S_2$ transition. The emission wavelength for excitation spectra was chosen at 0-0 band of monomer emission, 375 nm. The peak of excimer emission is around 470 nm. The excimer-to-monomer ratio (E/M) was the intensity ratio of the emission at 470 nm and 375 nm, respectively. The sample temperatures were regulated by a water bath (RTE-111, Neslab Instruments, Inc., Portsmouth, NH). The temperatures were recorded by a Fluke 51 K/J thermocouple (John Fluke MFG Co., Everett, WA) inserted into the fluorometer cell compartment in close contact with quartz cell.

The samples were degassed through freeze-pump-thaw cycles (at least 3 times). All solvents showed no fluorescence in the range of interests. All of the spectra reported here were solvent (background) subtracted.

Results and Discussion

1. Temperature Dependence of Dipy Fluorescence Behavior

The fluorescence behavior of dipy can be divided in two regions. At low temperature, there is a steady decrease in monomer emission accompanied by an increase in excimer emission. This results in a well-defined iso-emissive point as shown in Figure 6.2. For instance, in the case of dipy in the mixture of PEG 600 and acetonitrile with viscosity η = 28.0 cP at 20 ^{0}C, this iso-emissive point is at 436 nm. In this temperature range, the production of intramolecular excimer formation is a thermally activation process and its rate competes with monomer fluorescence.

As temperature is further increased, the iso-emissive point of the fluorescence spectra no longer exists. The intensity of both monomer and excimer emission bands decreases although in a different proportion as shown in Figure 6.3. Figure 6.4 gives a logarithmic plot of the E/M ratio in three solvent mixtures of PEG 600 and acetonitrile as a function of temperature. The E/M ratio increases with temperature in the range in which excimer fluorescence is determined by the rate of excimer formation. At higher temperature, E/M passes through a maximum at temperature T_{max} and decreases as the temperature is further increased, reflecting the excimer dissociation equilibrium. Comparing the T_{max} at three solvent mixtures, T_{max} increases with solvent viscosity. This is because the apparent activation energy for excimer formation increases with solvent viscosity (32).

The intensity changes which characterize the formation and deactivation of intramolecular excimer state can be described by the following kinetic scheme:
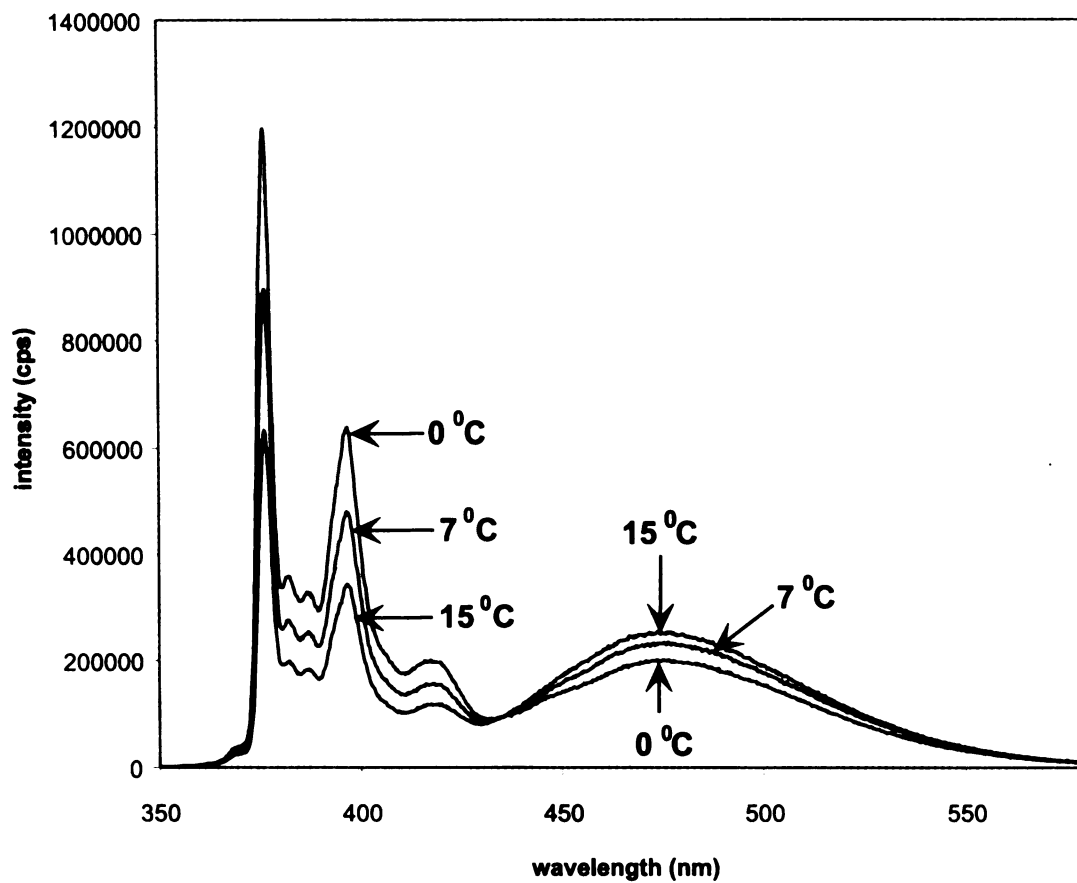
Figure 6.2. Fluorescence spectra of dipy in the low temperature range exibilting an iso-emissive point (436 nm). The viscosity of solvent mixture is 28 cp at 20 ^{0}C.
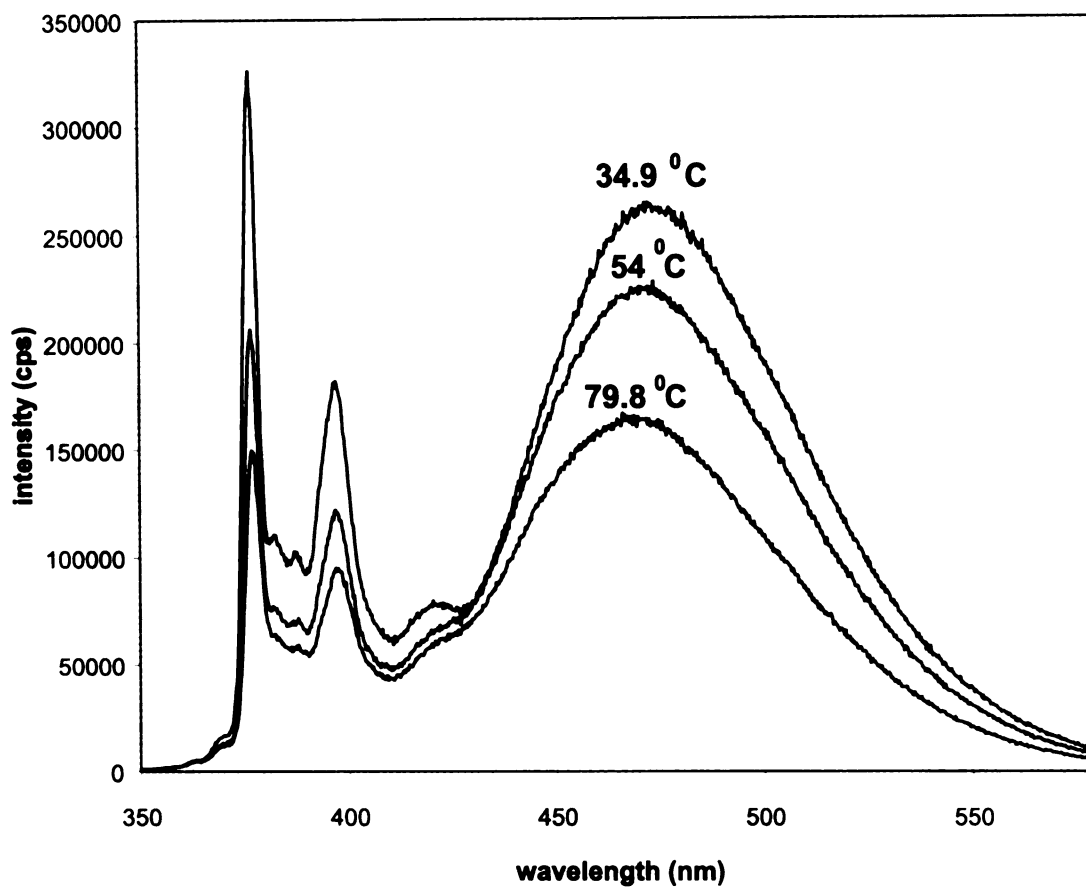
Figure 6.3. Fluorescence spectra of dipy at high temperature range. Note that the iso-emissive point characteristic in the low temperature range no longer exists. The viscosity of solvent mixture is 28 cp at 20 °C
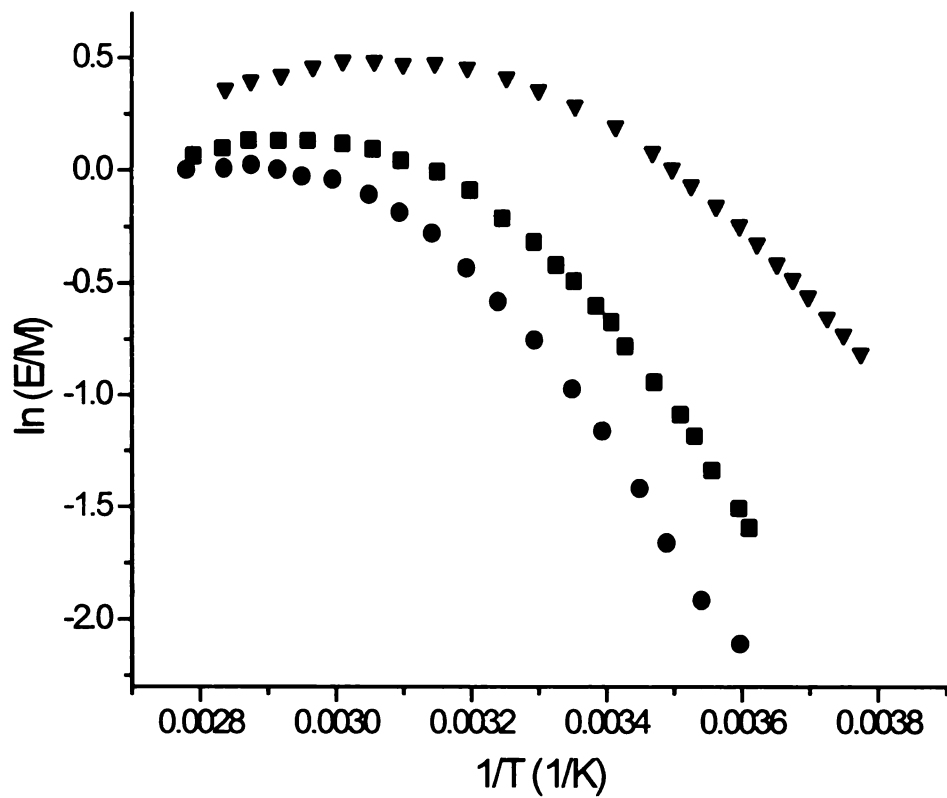
Figure 6.4. Temperature dependence of E/M of dipy in three solvent mixtures with viscosity η: 6.64 cP (▼), 28.0 cP (■), 54.2 cP (●).
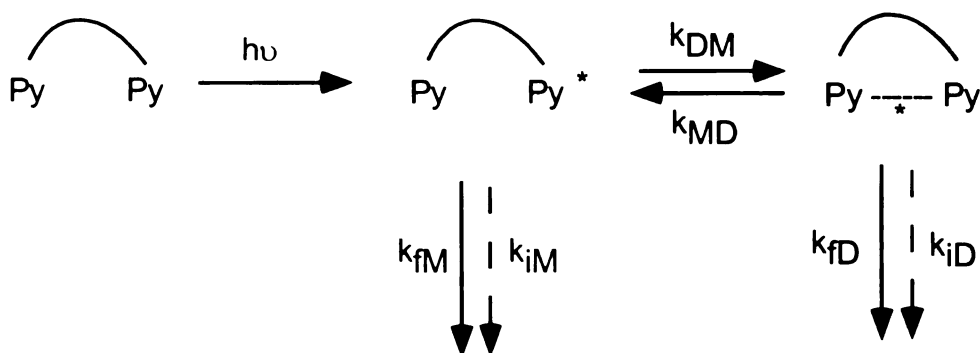
$$\text{Py}\quad\text{Py}\quad\xrightarrow{\ h\upsilon\ }\quad\text{Py}\quad\text{Py}^{*}\quad\underset{k_{MD}}{\overset{k_{DM}}{\rightleftarrows}}\quad\text{Py}\text{---}\text{Py}$$

$$k_{fM}\Big|\ k_{iM}\qquad\qquad k_{fD}\Big|\ k_{iD}$$

where k_{fD} and k_{fM} represent the radiative rate constant of excimer and monomer; k_{iM} and k_{iD} are the radiationless rate constant of monomer and excimer; k_{DM} and k_{MD} are the rate constant for excimer formation and dissociation, respectively.

According to the above scheme, the excimer-to-monomer ratio (E/M) can be approximated in:

$$\frac{E}{M}=\frac{k_{fD}}{\beta\times k_{fM}}\times\frac{k_{DM}}{k_{MD}+k_{fD}+k_{iD}}\qquad\qquad(6.6)$$

where β is a proportionality constant. In Equation 6.6, k_{fD} and k_{fM} are independent of temperature and solvent (25). In the low temperature range, more specifically when $T < T_{max}$, excimer fluorescence is determined by the rate of excimer formation as shown in Figure 6.4. The excimer dissociation rate is thus negligible (33). The presence of iso-emissive point in the low temperature range (Figure 6.2) signifies that radiationless rate constants k_{iM} and k_{iD} are temperature independent (34-36). Therefore,

160

$$\frac{E}{M} = C \times k_{DM} = C \times A \exp(-E_a / RT) \qquad (7)$$

where $C = \dfrac{k_{iD}}{\beta \times k_{iM}} \times \dfrac{1}{k_{iD} + k_{iD}}$ is a constant in the low temperature range in which there

is an iso-emissive point. The E/M thus represents the excimer formation rate. From the

plot of ln(E/M) vs. 1/T, the apparent activation energy E_a is obtained. Figure 6.5 shows a

few examples of the plot ln (E/M) vs. 1/T under different solvent mixtures. The apparent

activation energy E_a in the whole solvent series is listed in table 6.1.

The solvent viscosity in a finite temperature range follows an empirical

hydrodynamic relationship with temperature as following:

$$\eta = \eta_0 \exp(E_\eta / k_B T) \qquad (8)$$

where η_0 is the limited solvent viscosity when temperature is approaching infinity, k_B is

the Boltzmann constant, E_η is the activation energy due to solvent viscous flow. The E_η

values are listed in Table 6.1. From the Table 6.1, E_η increases with solvent viscosity.

If the intramolecular excimer formation is a diffusion-controlled pseudo-

monomolecular reaction, the excimer formation rate should follow the Einstein-

Smoluchoski diffusion theory (37):
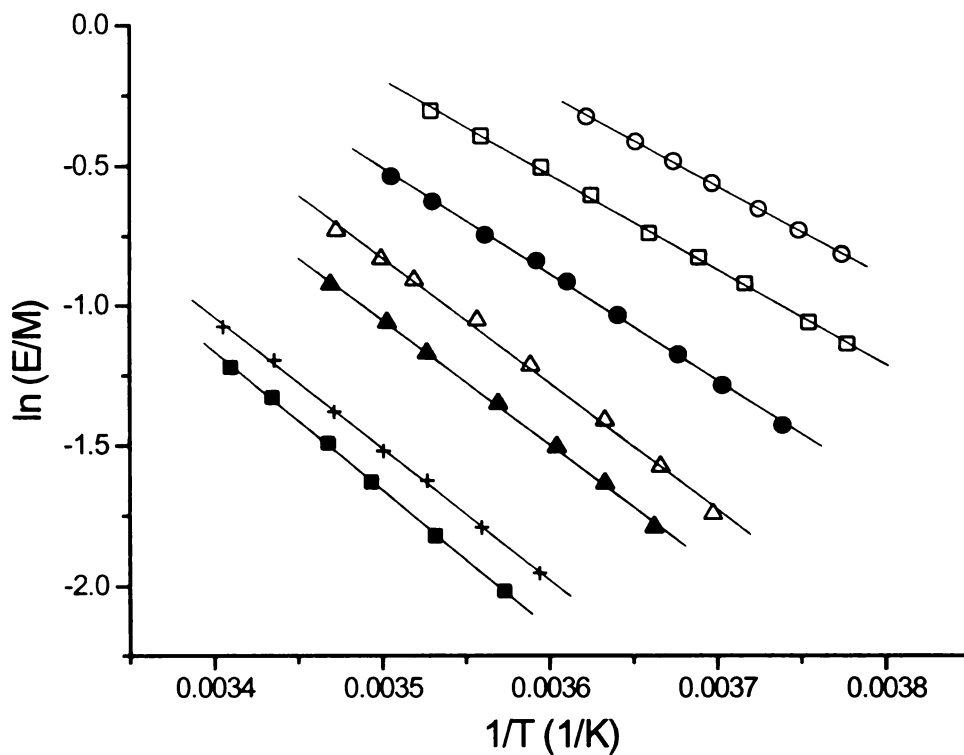
Figure 6.5. In the low temperature range in which an iso-emissive point exists, the plot of ln(E/M) vs 1/T yields the apparent activation energy for the intramolecular excimer formation in different solvent mixtures with viscosity: 54.2 cP (■), 43.5 cP (+), 28.0 cP (▲), 20.4 cP (△), 12.2 cP (●), 8.66 cP (□), 6.64 cP (○) at 20 ^{0}C.

Table 6.1. the activation energies at different solvent mixtures. E_a, E_η and E_{diff} are apparent activation energy derived from Equation 6.7, activation energy due to viscous flow (Equation 6.8) and activation energy for diffusion-controlled reaction (Equation 6.9), respectively.

η at 20 ^{0}C (cP)	E_η (kJ/mol)	E_{diff} (kJ/mol)	E_a (kJ/mol)
5.80	21.43	23.85	24.24
6.33	22.02	24.44	24.37
6.64	23.56	25.96	26.99
8.66	25.76	28.15	28.22
11.31	27.10	29.53	32.59
12.19	27.36	29.79	31.76
18.50	28.41	30.89	35.91
20.44	29.83	32.29	35.95
23.29	30.91	33.38	36.53
28.00	32.75	35.17	36.94
31.27	34.78	37.21	37.28
35.89	34.72	37.15	38.21
43.54	34.53	37.00	38.96
54.18	36.02	38.49	39.49
58.75	36.10	38.56	36.79
68.69	36.45	38.92	37.67

$$k_{DM} = \frac{8RT}{3000\eta} = A_{diff} \exp(-E_{diff} / RT) \tag{6.9}$$

where η is solvent viscosity in cP, R is the gas constant in J mol^{-1} K^{-1}, A$_{diff}$ is the pre-exponential factor. E$_{diff}$ is the activation energy for the diffusion-controlled reaction. The plot of ln (T/η) vs. 1/T yields E$_{diff}$, which is also listed in Table 6.1.

Within experimental errors, E$_{diff}$ is equal to E$_a$. Therefore, the intramolecular excimer formation is also a diffusion controlled reaction as is the intermolecular excimer formation (25, 38). The Einstein-Smoluchoski diffusion rate is the collision rate of pyrene moieties, which is determined by translational friction or translational diffusion rate. This indicates that slip boundary condition under which the rotational friction is zero (1, 19) is adequate approximation for the pyrene intramolecular excimer formation as used by Hara etal (28).

2. Viscosity Dependence of Intramolecular Excimer Formation

In the previous section, it has been shown that in the low temperature range, E/M ratio is proportional to excimer formation rate and the plot of ln (E/M) vs. 1/T yields a straight line. At higher temperature but still far lower than T$_m$, E/M ratio starts to deviate from the straight line as shown in Figure 6.4 because the assumption that k$_{iD}$ is temperature independent breaks down. In this section, we study solvent viscosity effects on excimer formation rate represented by E/M ratio at constant temperature. All of the E/M ratios is the calculated value from the linear relationship of ln(E/M) vs 1/T. In the low temperature range, the calculated E/M is almost identical to the experimental E/M

due to little data scattering as shown in Figure 6.5. In the case that temperature is over the limited low temperature range, the extrapolated E/M based on the straight line is used. This calculated E/M ratio is adequate to represent k_{DM}, the excimer formation rate, because k_{DM} is not a function of k_{iD} while experimental E/M is.

Figure 6.6 shows the calculated E/M vs solvent viscosity at two different temperatures. The curve is fitted well by empirical relationship (Equation 6.5). Two parameters generated from the curve fitting, $f(T) = A \exp(-E_0/RT)$ and α value are listed in Table 6.2.

Table 6.2. the parameters obtained through curve fitting based on the empirical Equation 6.5.

Temperature ($^\circ$C)	$f(T) = A \exp(-E_0/RT)$	α
5.0	5.22	0.796
7.5	5.37	0.793
10.0	5.51	0.790
12.5	5.66	0.787
15.0	5.82	0.784
17.5	5.97	0.780
20.0	6.13	0.777

The viscosity effect on rate constant is included in term $\eta^{-\alpha}$, leaving $f(T) = A \exp(-E_0/RT)$ is a function of temperature. The intrinsic activation energy E_0 derived from the plot of ln $(f(T))$ vs. $1/T$ (Figure 6.7) is obtained as 7.25 kJ/mol.

Figure 6.6. The solvent viscosity effects on intramolecular excimer formation rate at (A): 5 ^{0}C; (B): 10 ^{0}C. Solid circle: actual data points; dot line: fitting based on empirical relationship (equation 5); solid line: fitting based on Kramers theory (equation 10). Note especially the deviation of the theoretical value predicted by Kramers theory from the experimental data in high viscosity region.
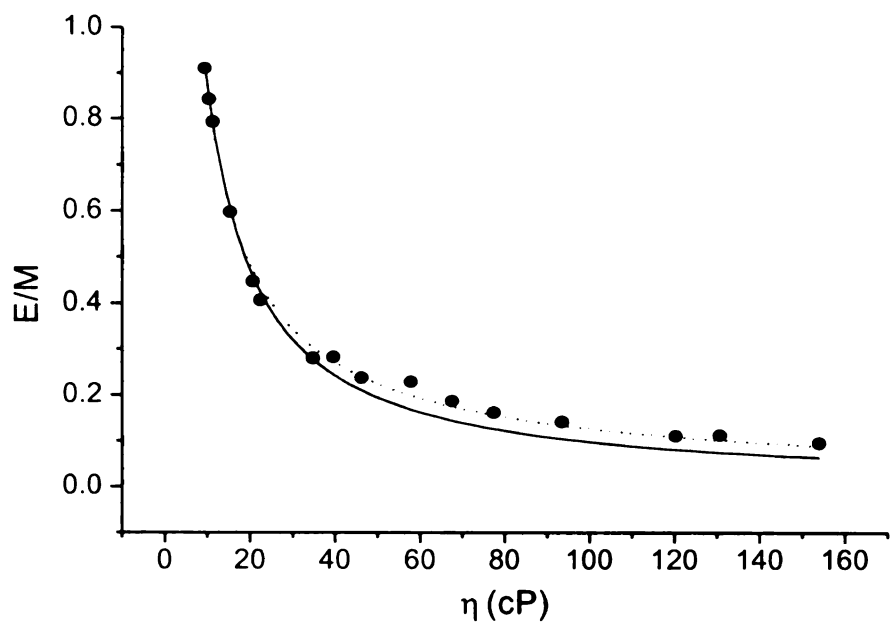
(A)
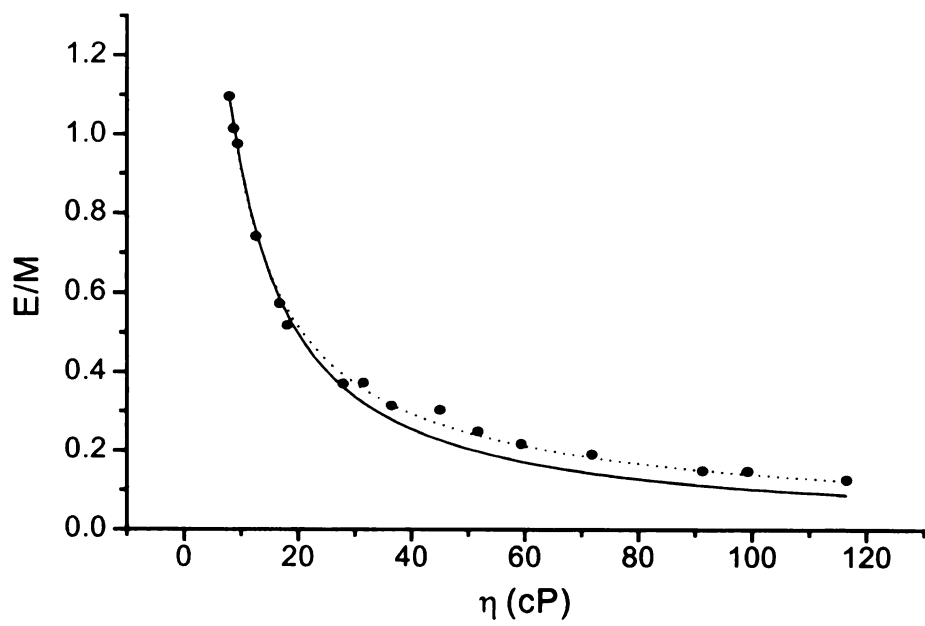
(B)
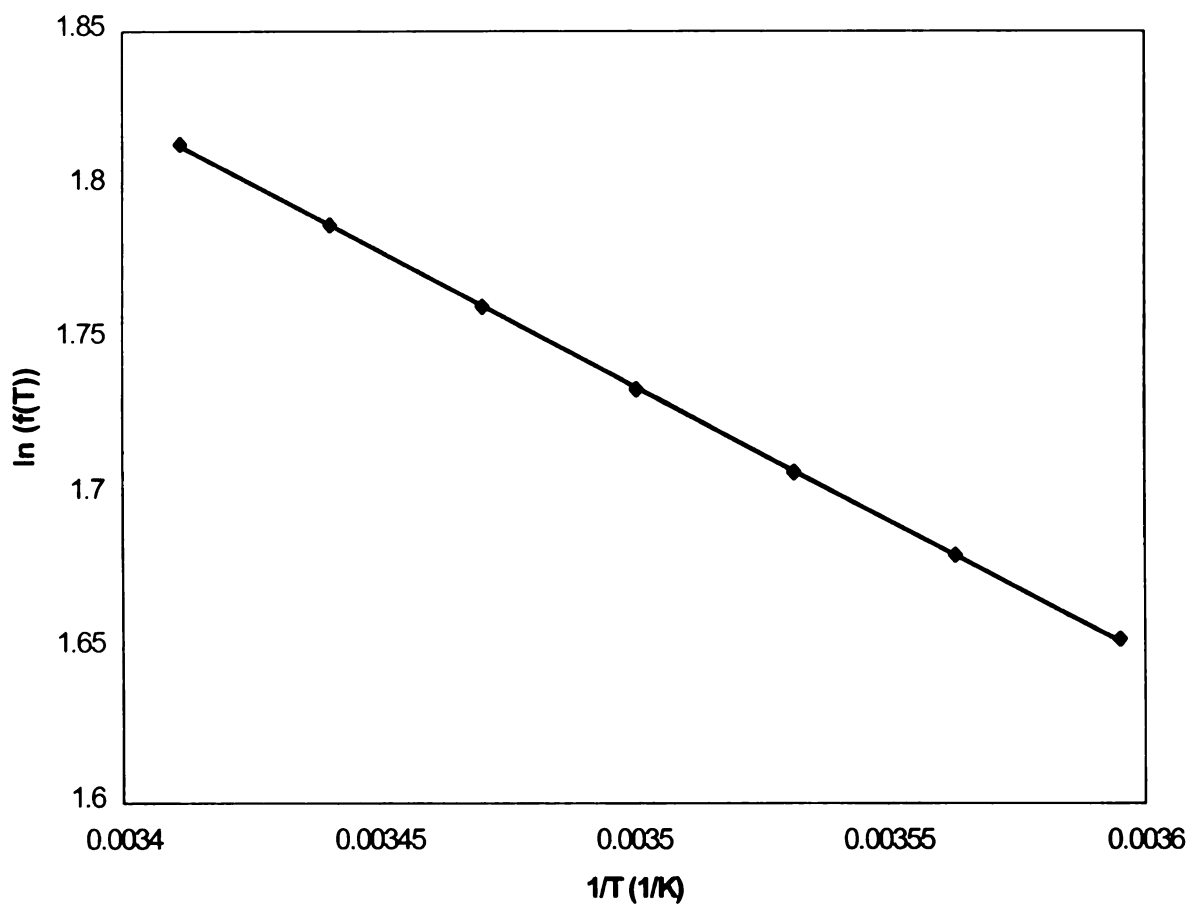
Figure 6.7. The intrinsic activation energy of the dipy intramolecular excimer formation: 7.25 kJ/mol. f(T) is the sole function of temperature obtained from curve fitting based on the empirical equation 5. Note the perfect linear relationship.

If we assume the slip boundary condition ($\zeta = 4\pi r\eta$) for the present analysis,

Kramers equation (Equation 6.3) can be re-written in:

$$k_{KR} = (1 + B^2\eta^2)^{1/2} - B\eta \qquad (6.10)$$

$$B = \frac{2\pi r}{\mu\omega_b} \qquad (6.11)$$

where r is the rotating radius, μ is the reduced mass, ω_b is the frequency at barrier top. The fitting based on Equation 6.10 is not satisfactory, especially in the higher viscosity region as shown in Figure 6.6. There are four possible reasons for the breakdown of Kramers theory as discussed in the introduction part.

The first possible reason is due to the frequency dependent friction. For DPP, Hara etal (28) found that the curve of k_{DM} vs. zero-frequency shear viscosity was well fitted by Kramers equation. Dipy has the same rotating pyrene moieties as DPP. Furthermore, the intrinsic activation energy barrier of dipy is even lower than that of DPP, which indicates that barrier curvature or imaginary fequency ω_b at barrier top is less than that of DPP. The reactant molecule dipy will spend more time at the barrier top to probe the solvent motion than DPP will. If no frequency dependent friction has been found in DPP, the deviation due to frequency dependent friction is even less unlikely for dipy.

The second possible reason is because the size of rotating pyrene moiety is comparable to that of solvent molecules, PEG 600 in particular. In this case, Skinner and Wolynes (14, 15) adopted a different stochastic approach to the dynamics of chemical reactions in solution. They used the BGK collision model (39, 40) which is considered to yield the best description when solute and solvent molecular masses are comparable. They finally derived the following hydrodynamics equation by assuming that friction coefficient (ζ) is proportional to solvent viscosity (η) (16, 17):

$$k_{DM} = \frac{4\pi\eta}{B}(1 + \frac{2\pi\eta}{B} + \frac{8\pi\eta^2}{B^2})^{-1} \times k_{TST}$$

(6.12)

k_{TST} is rate constant derived from transition state theory. $B = 2\omega\eta g^{-1}$ with ω, the frequency at barrier top and well (assuming they are same); g, average collision frequency. The fitting based on Skinner and Wolynes theory is almost identical as Kramers theory (Figure 6.8). Therefore, solvent-solute size ratio contributes little to the deviation at higher viscosity region.

The third possible reason is that solvent changes reaction potential surface. Hara etal (28) showed that for DPP, Kramers equation fits the whole range of viscosity irrespective to solvent type and polarity. This indicates that the potential surface is affected very little by solvent in the pyrene intramolecular excimer formation. In addition, fluorescence and absorption (excitation) spectra (data not shown) showed little change in different solvent mixtures. The very little data scattering in the plot of $\ln(f(T))$
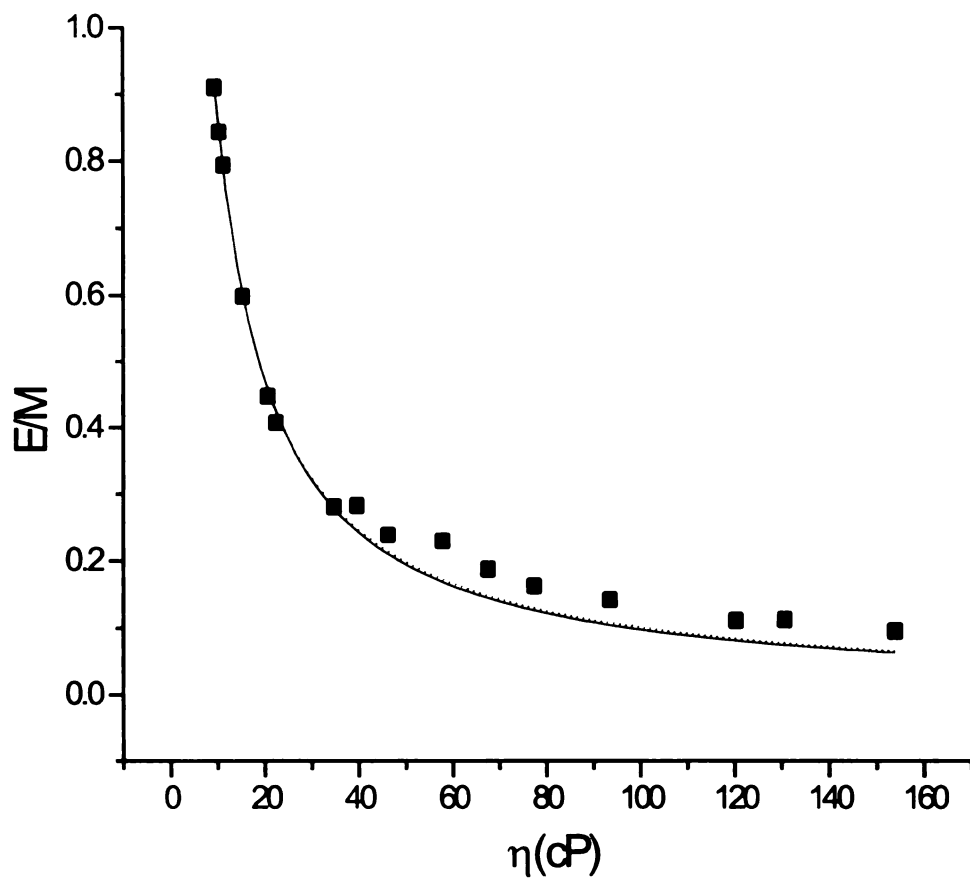
Figure 6.8. The comparison of the curve fitting based on Skinner-Wolynes theory (equation 12, dot line) and Kramers theory (equation 10, solid line). Solid squares are actual data points. Note the almost complete overlap of the two fitting curves.

vs 1/T (Figure 6.7) provides further evidence that the potential surface remains almost unaffected by solvent mixtures.

Therefore, the only possible reason left for the deviation in the high viscosity region is the multidimensional nature of the potential surface of dipy molecule. Comparing dipy with DPP, the major difference between the two molecules is the bond number between two pyrene moieties. For DPP, it is believed that only one hindered rotation is involved in the intramolecular excimer formation. Therefore, the one-dimensional Kramers' theory is adequate to describe the behavior of DPP excimer formation. For dipy, however, the one-dimensional Kramers' theory breaks down because thirteen bonds are between two pyrene moieties. Besides the reactive mode, there are many non-reactive modes. With the relative low potential barrier of the dipy excimer reaction and in the diffusion or high friction limit, the activation barrier curvature is so small and the solvent damping force is so large that the barrier is crossed and re-crossed many times before excimer is finally formed. Therefore, there is enough time for the coupling between reactive mode and non-reactive mode to occur. This coupling enables the reaction system to take the path with least friction. The reaction rate is thus enhanced (21, 22). The best possible fitting based on Kramers equation yields B values at different temperature. The B values are listed in Table 6.3.

Table 6.3: Kramers' parameter (B) derived from curve fitting

Temperature (^{0}C)	B (cP^{-1})
5.0	0.129
7.5	0.132
10.0	0.134
12.5	0.137
15.0	0.140
17.5	0.142
20.0	0.144

The B value for dipy is around 0.13 cP^{-1} in good agreement with 0.11 cP^{-1} for DPP (28). The fitting based on one-dimensional Kramers' theory starts to deviate from experimental data at solvent viscosity ~ 20 cP (Figure 6.6 A). At $\eta \geq$ 20 cP and with B = 0.13 cP^{-1},

$$k_{KR} = (1 + B^2 \eta^2)^{1/2} - B\eta \cong 1 / (2B\eta) \qquad (13)$$

$k_{KR} \propto 1/\eta$ and consequently $k_{DM} \propto 1/\eta$ corresponds to the reaction rate in the diffusion limit. In this limit, mode coupling becomes significant and the reaction rate for excimer formation is enhanced. The actual rate as represented by E/M is therefore higher than the rate predicted by Kramers' theory as shown in Figure 6.6. The theoretical rate starts deviating from the experimental value at lower viscosity when temperature is increased (Figure 6.6). This is because the higher B value at higher temperature pushes the diffusion limit to lower shear viscosity value.

Conclusion

In this report, a dipyrenyl membrane probe (dipy) has been studied in isotropic organic solvents. In low temperature range, a steady increase of intramolecular excimer intensity is accompanied by a decrease of monomer emission intensity, which results in a well defined iso-emissive point signifying that radiationless rate constants of monomer and excimer are independent of temperature. The further increase in temperature results in the decrease of both excimer and monomer emission intensity. The excimer-to-monomer ratio (E/M), however, increases until it reaches a maximum at temperature T_m, reflecting the excimer formation is the dominating factor in this temperature range. After T_m, E/M ratio decreases with temperature, reflecting the excimer dissociation at high temperature range becomes dominating. The apparent activation energy for intramolecular excimer formation can be derived in the low temperature range. By comparing the apparent activation energy with the activation energy for diffusion reaction, we can conclude that the intramolecular excimer formation of dipy is also a diffusion-controlled reaction.

The intramolecular excimer formation rate as a function of viscosity is studied in a wide range of solvent viscosity. The function is fitted well by the empirical relationship between the reaction rate and solvent viscosity with α value, the fractional dependence of solvent viscosity, around 0.8. The intrinsic activation energy derived from the curve fitting at different temperature has been obtained as 7.25 kJ/mole. The fitting according

to Kramers equation, however, deviates from the experimental value, especially in high viscosity region where the experimental rates are higher than the rates predicted by Kramers theory. Four factors that attribute to the deviation have been examined one by one. It is finally concluded that the higher experimental rates are due to the reactive mode coupling to non-reactive modes. The mode coupling and long barrier crossing and re-crossing time in high viscosity region enable the reaction to choose a reaction pathway with the least friction, which, in turn, enhances the intramolecular excimer formation rate. To our best knowledge, our data have provided the direct experimental evidence to the theory on mode coupling and reaction pathway in solution phase proposed almost two decade ago.

Reference

1. Bagchi, B. *Intl. Rev. Phys. Chem.* **1987**, 6, 1

2. Kramers, H. A. *Physica* **1940**, 7, 284

3. Smoluchowski, M. V. *Z. Phys. Chem.* **1917**, 92, 129

4. Rothenberger, G; Negus, D. K.; Hochstrasser, R. M. *J. Chem. Phys.* **1983**, 79, 5360

5. Vesko, S. P.; Fleming, G. R. *J. Chem. Phys.* **1982**, 76, 3553

6. Vesko, S. P.; Waldeck, D. H.; Fleming, G. R. *J. Chem. Phys.* **1983**, 78, 249

7. Courtney, S. H.; Fleming, G. R. *J. Chem. Phys.* **1985**, 83, 215

8. Lang, J. M.; Dreger, Z. A.; Drickamer, H. G. *Chem. Phys. Lett.* **1995**, 243, 78

9. Hara, K.; Kiyotani, H.; Bulgarevich, D. S. *Chem. Phys. Lett.* **1995**, 242, 455

10. Hara, K.; Kiyotani, H.; Kajimoto, O. *J. Chem. Phys.* **1995**, 103, 5548

11. Hara, K.; Naoki, I.; Kajimoto, O. *J. Phys. Chem.* **1997**, 101, 2240

12. Grote, R. F.; Hynes, J. T. *J. Chem. Phys.* **1980**, 73, 2715

13. Bagchi, B.; Oxtoby, D. W. *J. Chem. Phys.* **1983**, 78, 2735

14. Skinner, J. L.; Wolynes, P. G. *J. Chem. Phys.* **1978**, 69, 2143

15. Skinner, J. L.; Wolynes, P. G. *J. Chem. Phys.* **1980**, 72, 4913

16. Sundstrom, V.; Gillbro, T. *Chem. Phys. Lett.* **1984**, 110, 303

17. Sundstrom, V.; Gillbro, T. in *Applications of Picosecond Spectroscopy to Chemistry* edited by Eisenthal, K. B.; Reidel Publishing Company, **1984**, 79

18. Akesson, E.; Sundstrom, V.; Gillbro, T. *Chem. Phys. Lett.* **1985**, 121, 513

19. Akesson, E.; Sundstrom, V.; Gillbro, T. *Chem. Phys.* **1986**, 106, 269

20. Harju, T. M.; Korppi-Tommola, J. E. I.; Huizer, A. H.; Varma, C. A. G. O. *J. Chem. Phys.* **1996**, 100, 3592

21. Grote, R. F.; Hynes, J. T. *J. Chem. Phys.* **1981**, 74, 4465

22. Van der Zwan, G.; Hynes, J. T. *J. Chem. Phys.* **1982**, 77, 1295

23. Carmeli, B.; Nitzan, A. *Chem. Phys. Lett.* **1984**, 106, 329

24. Agmon, N.; Kosloff, R. *J. Chem. Phys.* **1987**, 91, 1988

25. Birks, J. B. *Photophysics of Aromatic Molecules;* Wiley Interscience: New York, 1970; Chapter 7

26. Du, X. Y.; Hollingsworth, R. I. *Manuscript in preparation*

27. Fitzgibbon, P. D.; Frank, C. W. *Macromolecules* **1981**, 14, 1650

28. Hara, K.; Akimoto, S.; Suzuki, H. *Chem. Phys. Lett.* **1990**, 175, 493

29. De Schryver, F. C.; Collart, P.; Vandendriessche, J.; Goedeweeck, R.; Swinnen, A.; van der Auweraer, M. *Acc. Chem. Res.* **1987**, 20, 159

30. Winnik, F. M. *Chem. Rev.* **1993,** 93, 587

31. Huang, G. F.; Hollingsworth R.I. *Tetrahedron* **1998,** 54, 1355

32. Birks, J. B.; Lumb, M. D.; Munro, I. H. *Proc. Roy. Soc. A,* **1964,** 280, 289

33. Hara, K.; Yano, H. *J. Am. Chem. Soc.* **1988,** 110, 1911

34. Chandross, E. A.; Demster, C. J. *J. Am. Chem. Soc.* **1970,** 92, 3586

35. Goldenberg, M.; Emert, J. Morawetz., H. *J. Am. Chem. Soc.* **1978,** 100, 7171

36. Melnick, R. L.; Haspel, H. C.; Goldenberg, M.; Greenbaum, L. M.; Weinstein, S.

    Biophys.J. 34, 499

37. Atkins, P. W. *Physical Chemistry* 5th edition: Freeman: New York, 1994; Chapter 27

38. Zagrobelny A.; Betts, T. A. and Bright, F. A. *J. Am. Chem. Soc.* **1992,** 114, 5249

39. Bohm, D.; Gross, E. P. *Phys. Rev.* **1949,** 75, 1864

40. Bhatnagar, P. L.; Gross, E. P.; Krook, M. *Phys. Rev.* **1954,** 94, 511

Chapter 7

Domain Shape Evolution with Time in Lipid Multilayer Films

Introduction

Stripes and bubbles are the basic domain patterns in a variety of chemical, physical and biological systems (1-3). It is the elementary stripe and bubble that constitute remarkably similar microscopic textures regardless of molecular structure and composition. A universal mechanism for the formation of the similar domain textures in a variety of systems has been proposed by the competing interactions that generate the so-called modulated phase (4). The relative strength of the competing forces and consequently the relative contribution of the forces to the total free energy determine the final domain texture, either in bubble domain, stripe domain or the coexistence of two domains (5-7). The variation of the competing forces by changing parameters such as temperature, surface pressure, magnetic field or hydrodynamic flow initiates the domain pattern transition process. In a Langmuir film confined at the air-water interface, the transition between stripe and bubble domain textures is a first order phase transition (7, 8). The phase transition is involved in the context of an activated process. In this chapter, we report the first order transition process between stripe and bubble domains with time in a mulitlayer liquid crystal film, we consider the possible competing forces give rise to the transition processes. In addition, we estimate the thermodynamic parameters of the phase transition process between stripe and bubble and discuss future experimental improvements in order to analyze the domain pattern transition process quantitatively.

179

A Brief Background about Domain and Domain Shape Evolution

The concept of domain originates from ferromagnetic films. Within the context of the ferromagnetic films, domain is defined as a small region of ferromagnetic substance that contains many atoms all oriented in the same direction. The basic domain elements are bubbles and stripes even though the overall domain patterns may vary from one experiment to another (5). The bubbles and stripes are not unique in ferromagnetic films. Instead, they exist in a variety of chemical, physical and biological systems such as chemical reaction-diffusion system (1), block copolymers (19), Langmuir films (20) with a length scale ranging from a few hundred Angstrom (e.g.: lipid ripple phase) (21) to a few centimeters (e.g.: CO_2 convective roll pattern) (22). Seul and Andelman examined the wide range of systems and found that the systems with completely different chemical and physical origins share common competing interactions (5). For example, in Langmuir films, the electrostatic dipolar interaction that favors long stripe shape is balanced by the local line tension favoring bubble shape (20). In ferromagnetic films, a repulsive dipolar interaction is balanced by the attractive exchange interaction between ferromagnetically coupled spin (23). Within the framework of competing interactions, Seul and Andelman (5) generalized the concept of modulated phase and proposed that the competing interactions modulate the otherwise uniformed phase, which then causes phase separations. The basic domain patterns within the context of modulated phase are the uni-directionally modulated strips and trigonally modulated bubbles. The modulation period is determined by the balance of competing contributions to the free energy and generally varies as a function of temperature and applied field.

The system that is more familiar to chemists is the lipid monolayer film confined at air-water interface. The experimental setup is simple, mounting an epifluorescence microscope onto a Langmuir trough. The monolayer film in the Langmuir trough consists of lipids and an amphiphilic fluorescent probe with the concentration in the order of 1 mol%. Lipid domain can be visualized by taking advantage of the probe partition difference in difference lipid phases. Lipid domains were first observed by Peters and Beck (24) and later greatly expanded by McConnell's laboratory (20) and Möhwald's laboratory (25). Domain shape and domain shape evolution depends sensitively on temperature, surface pressure and, sometimes, low concentration of "impurities" (e.g.: cholesterol). As with many other systems, the basic domain patterns in monolayer films are bubbles and stripes. The competing interactions are the attractive local line tension and the repulsive dipolar interaction. Adjusting one of the interactions can dramatically change the domain shape. For example, a bubble domain can be switched immediately to a stripe domain by adding 2-4 mol% cholesterol while maintaining other parameter constant (26). The fundamental reason behind the domain transition is that cholesterol decreases the line tension between the domain boundaries and thus the dipolar interaction that favors stripe domain becomes dominated. The domain transition between bubble and stripe can also be realized by surface pressure of the lipid monolayer. The size of bubble domains increases with the increase of surface pressure and the bubble domain eventually becomes electronically unstable. The domain will then assume either an ellipse shape or bubble shape with higher harmonics that will finally becomes a stripe domain as the surface pressure is further increased. This domain shape evolution process can also be reversed at least theoretically by change the surface pressure (20).

Materials and Methods

The specimens were prepared according to the procedures in ref. 9. Egg lecithin was sandwiched between a microscope slide and a cover slip. The lipid multilayer with alternate water layer and lipid bilayer was then formed by a slow hydration process in a chamber with a constant temperature (about 60 ^{0}C) and humidity for several days. All images were visualized at room temperature with Zeiss LSM 210 laser scanning confocal microscope (Carl Zeiss, Thornwood, NY) equipped with a 488 nm Ar laser. A 40X dry objective was used unless otherwise specified. A program called time series has been used to collect images at specific time intervals. The dynamic events of the domain transition process under a hydrodynamic flow with time have been visualized and recorded. In contrast to conventional liquid crystal visualization, our images were obtained by phase contrast and confocal reflection microscopy. The methodology development has been published elsewhere (9).

Results and Discussion

1. The First Order Domain Shape Transition Process

Figure 7.1 shows the stripe to bubble transition process after generating a hydrodynamic flow. The stripe was first bent from (a) to (b) after domain shape fluctuation. The bending stripe was in higher energy state due to elastic modulus (10, 11). A bubble and a straight stripe were then formed (c) after domain shape relaxation and consequent fission process. The newly formed domains were in equilibrium or metastable equilibrium state since there was no obvious domain pattern evolution from (c) to (d).

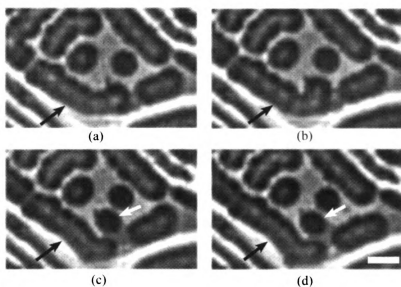Figure 7.1. Stripe to bubble transition by phase contrast microscopy. (a) Stripe (black arrow) started bending; (b) A sharp bending provided enough energy for the stripe to reach a transition state; (c) Bubble (white arrow) was then formed through fission of the bending stripe and quickly reached an equilibrium or metastable equilibrium state (d). The time between consecutive frames is 0.9 second. Scale bar in (d) is 5 μm.
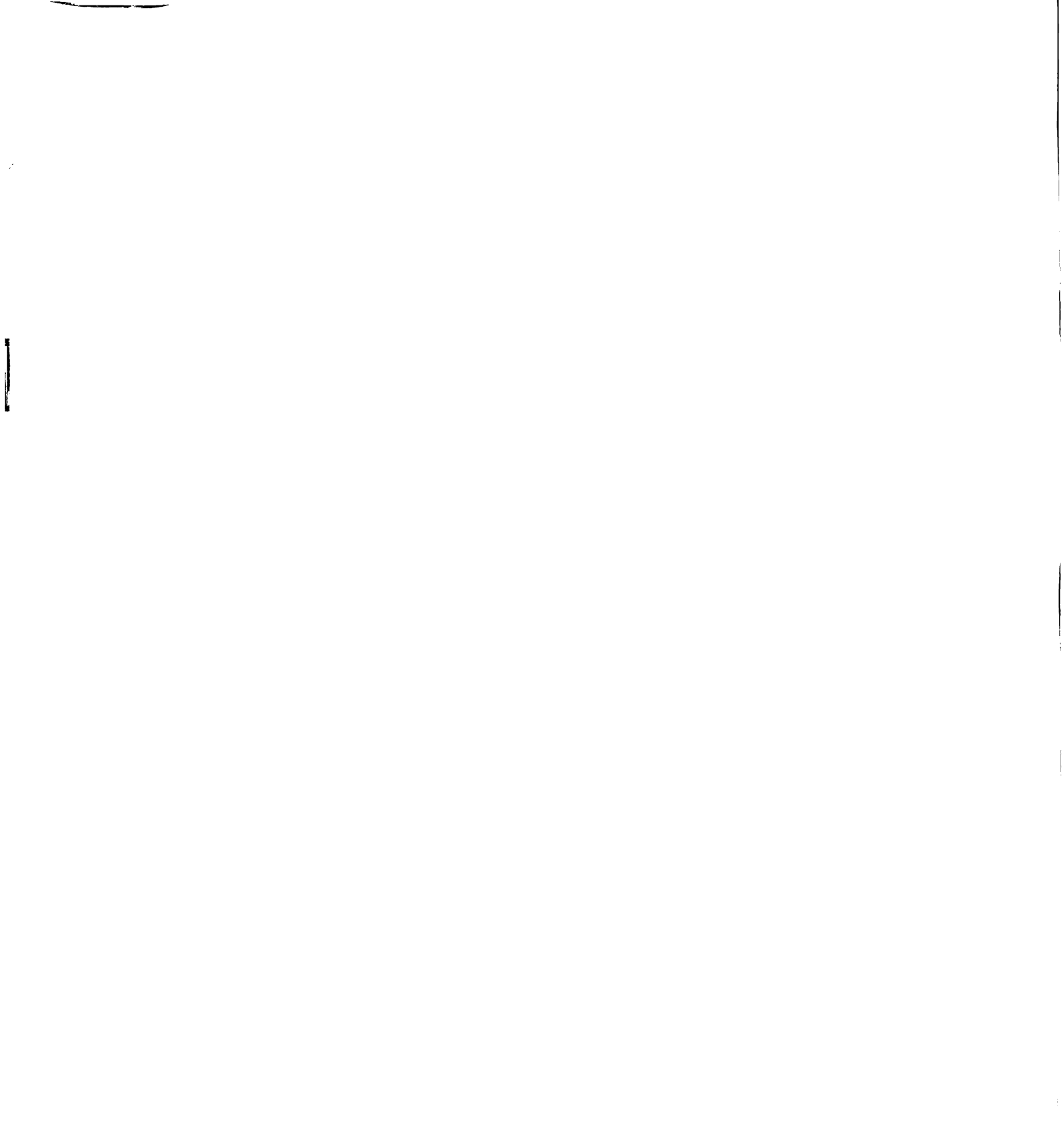
The domain pattern transition between stripe and bubble is a typical first order phase transition process, reminiscent of a monolayer at the air-water interface (2, 7). After passing an energy barrier corresponding to the energetic state of the bending stripe, it is believed that stripe transformed to bubble in a continuous fashion just like a bubble to an ellipse and finally to a stripe in monolayer. However, the time interval between consecutive frames, 0.9 second, is too long for observing the continuous transition process. In order to prove the continuous domain shape evolution process, we conducted another experiment by heating the specimen to about 60 ^{0}C in a closed chamber and then cooling it down to room temperature. A snapshot image at room temperature under confocal reflection microscopy was obtained as shown in Figure 7.2. The transition processes can be visualized by stripe contracting to bubble stepwise in the order of A to C as seen clearly in Figure 7.2. Phase contrast and polarizing images also indicated the continuous evolution process (9). Due to thermal inhomogeneity within the liquid crystal film, it was at different time for the stripes to acuminate enough energy and to reach the transition state and then to initiate the domain transition process. As a result, we can picture the domain transition process of one stripe through a snapshot of domain transitions of many stripes even though we did not track down the domain pattern evolution process of a specific stripe. It was also impossible to visualize the process by microscopy because of thermal turbulence (12). In addition, heating the liquid crystal film is essentially to generate a hydrodynamic flow because thermal turbulence due to heating caused the liquid crystal rearrangement (12, 13). The results obtained from the two experiments are thus comparable.
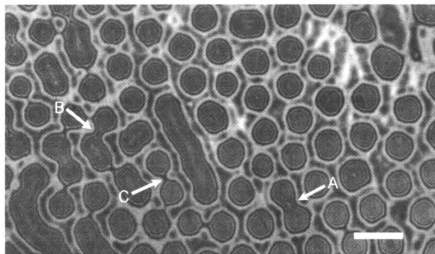
Figure 7.2. One snapshot of transition processes of many stripes after specimen heating and cooling. Note especially the stepwise contraction of stripe to bubble in the order of A to C. Bar scale is 10 μm. Imaging mode: confocal reflection.

In addition, we also observed that the transition from bubble to stripe, the reverse process of stripe to bubble, was also a first order process in the multilayer liquid crystal film. Bubbles with higher harmonic shape that were presumably in thermally excited state or transition state were formed and consequently transformed to stripe domain (Figure 7.3). The fact that stripe and bubble coexist (Figure 7.2) and can be converted back and forth indicates that the two types of domains are in approximately same energy level. The domain transition is therefore controlled possibly by kinetic driving force, which is determined by the activation energy barrier. Our observation about the domain transition with time provided a possible means to obtain the kinetic information. If the kinetics of the domain transition is well understood, it is then possible to convert stripe domain completely to bubble domain and vise versa. The two types of domains converting back and forth is the basic property of switchable optics and electronics. It may also be a possible mechanism of living organisms responding to external or internal perturbations such as temperature variations, pH changes or protein binding to membrane surface.

2. The Competing Interactions

Our experimental results in the lipid mulitlayer film are very similar to the results obtained from monolayer at air-water interface even though these are different systems. The different systems sharing same phenomena directly point to the recently proposed universal mechanism based on competing interactions (4). In an amphiphilic monolayer
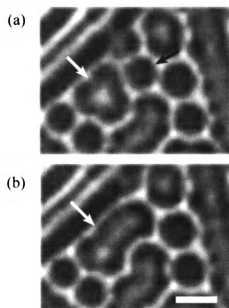
Figure 7.3. Transition from bubble to stripe by phase contrast microscopy. (a) Round bubbles formed a bubble with higher harmonics (white arrow); (b) A stripe (white arrow) was then formed by fusing the higher harmonic bubble with another bubble (black arrow). Scale bar in (b) is 5 μm.

confined at air water interface, a repulsive electrostatic dipolar interaction which favors long stripe shape is balanced by a local line tension favoring bubble shape (14). As with Langmuir films, we believe that the domain shape transition in our experiment is also the result of competing interactions. The shear force due to a hydrodynamic flow causing stripe fission is opposed by hydrodynamic drag force. The proposed competing forces are based on recent experimental observation and theoretical calculation on monolayer and bilayer domain deformation under extensional flow field (15-17). The two competing forces contribute to the total free energy function in an opposite way. The minimization of the total free energy determines the final domain shape. The quantitative analysis of the free energy function requires a stable and controlled flow field and is thus an open object for future research.

3. Estimation of Thermodynamic Parameters of Stripes and Bubbles

We estimate the energy difference of stripe and bubble at ground state and treat the system as a two-level system. At equilibrium, the number of stripes and bubbles follows Boltzmann distribution when stripe and bubble coexist (figure 7.2). Three approximations have been used in this estimation:

(1). We ignore the detail processes of how stripe and bubble are transformed. This approximation is valid because energy is a state function. So the net transition process can be expressed:

$$\text{stripe (S)} \leftrightarrow \text{bubble (B)} \tag{7.1}$$

(2). We assume that all of the stripes and bubbles at equilibrium as shown in figure 7.2 are at ground state and uniform. The stripe curvature or bubble size is averaged and the variance is ignored. The stripe thus represents an energy level and bubble represents another.

(3). Energy levels of stripe and bubble at excited states are a continuous function of stripe bending curvature and bubble diameter respectively (10, 15). The energy level density of stripe and bubble is assumed to be approximately same.

From Boltzman distribution,

$$P_s/P_b = \exp(-\Delta E/RT) = 12/59 \qquad (7.2)$$

where P_s is the number or possibility of stripes; P_b is the number or possibility of bubbles. The energy difference (ΔE) between stripe and bubble at ground state can be obtained from Equation 7.2 as 3.9 kJ/mol at 25 ^{0}C. The positive value signifies that the stripe is at higher energy state.

The equilibrium constant of the phase transition process between stripe and bubble is

$$K = (Q_s/Q_b)\exp(-\Delta E/RT) \qquad (7.3)$$

Q_s and Q_b are partition functions of stripe and bubble respectively. Q_s is equal to Q_b since we assume the energy density of stripe is equal to that of bubble. Therefore, the equilibrium constant K is equal to 0.2 and the free energy at equilibrium state is 3.9 kJ/mol. Since $H = U + PV$, $\Delta H = \Delta U + \Delta(PV)$. If assuming the volume change after the domain transition remain the same, $\Delta H = \Delta U = \Delta E = 3.9$ kJ/mol. In addition, $\Delta G = \Delta H - T\Delta S$. Therefore, $\Delta S = (\Delta H - \Delta G)/T = 0$. This zero entropy difference between stripe and bubble is understandable because entropy represents the dispersal of energy and we assumed that the energy level densities of bubble and stripe are continuous and same.

4. Added in Proof and Future Perspectives

In order to reproduce the dynamic events of domain transition process, further experiments have been performed. The sample preparation follows the same procedures as those in the experimental section. The experimental conditions to get the coexistence of stripe domain and bubble domain are still unknown. As estimated in the previous section in this chapter, the energy difference between the stripe and bubble is very small. The domain patterns obtained are most often either pure stripes or pure bubbles due to the easy conversion process between stripe and bubble. To get the coexistence of the stripe and bubble thus requires fine tuning and more or less luck at least at this stage of the experiment. Substantial amount of extra water is often added into the specimen in preparation of the hydrodynamic flow. The microscope slide and cover slip have been sheared slightly to initiate the hydrodynamic flow.

As shown in Figure 7.4, stripe bending is often the prerequisite for the stripe to bubble domain transition process. Even though the whole sequence of the stripe bending is not captured, the image series do show the stripe bending is increased from (a) to (b). When the stripe is bent to enough degree and the corresponding energetic state of the bending stripe reaches a sufficient high level, the domain transition is initiated. A bubble is formed through stripe fission, a phenomenon which is similar to lipid monolayer confined at air-water interface (2, 18). A new channel of the domain transition process has also been observed as shown in figure 7.5. Stripe is transformed to bubble through stripe elongation. Even though the bubble is formed through different channels, they share the same physical origin. Both bent stripe ((b) in Figure 7.4) and elongated stripe ((c) or (d) in Figure 7.5) correspond to the transition state of the domain transition process. After the stripe gains enough energy from the flow field to pass the transition state, the domain transition process is initiated and a stable bubble domain is then formed. This is a typical first order phase transition process (2, 7). These experimental observations are in excellent agreement with the previous experimental result (Figure 7.1).

The bubble to stripe transition process has also been observed (Figure 7.6). Similar to the previous result (Figure 7.3), the bubble with higher harmonic shape (HS in (a) and (b) of Figure 7.6), which is presumably in higher energy state, fuses with another bubble to form a straight stripe (arrow in (c)). The newly formed domain is in equilibrium or metastable equilibrium state since there was no obvious domain pattern evolution from (c) to (d).
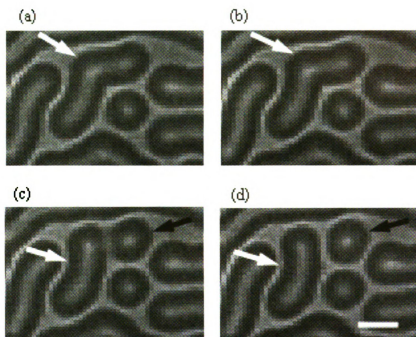
Figure 7.4. The domain shape transition process from stripe to bubble through stripe bending. (a) bent stripe; (b) stripe bending is further increased; (c) Domain transition is initiated through stripe fission. Note the bubble and the straight stripe are still partially connected. (d) The fission process is complete. A stable bubble and a straight stripe are formed. Time interval between two consecutive images is 0.3 second. Bar scale in (d): 5 μm.
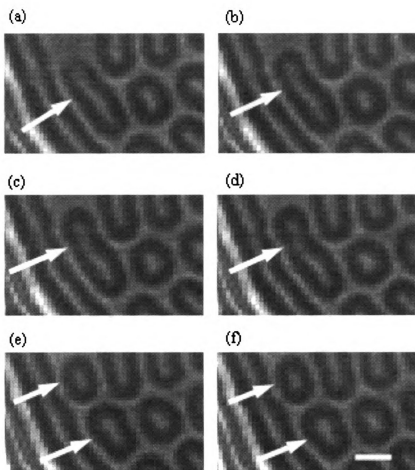
Figure 7.5. The image sequence recording the stripe shape transition process through stripe elongation. A stripe is elongated from (a) to (d). Note especially the stripe starts thinning at the part pointed by white arrow. The stripe fission is initiated at the thinning point. After the fission process, stable bubbles are formed, (e) and (f). Time interval: 0.3 second. Bar scale: 5 μm.
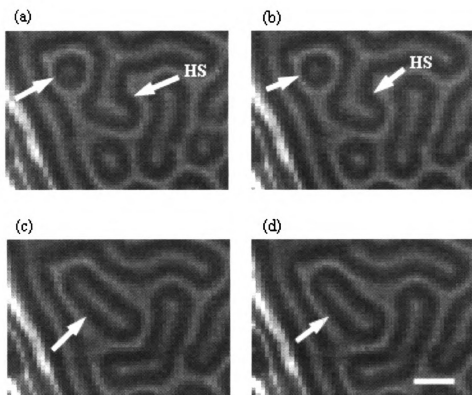
Figure 7.6. An image sequence recording a bubble domain with higher harmonics fuses with another bubble to form a straight stripe. HS: stripe with higher harmonic shape. Time interval: 0.3 second. Bar scale: 5 μm.

So far, we have demonstrated the complete reproducibility of the domain pattern evolution process. However, these results serve only as initial observations. They are by no means complete. The outlines in the following are the necessary refinement or improvement which, in my opinion, should be done in the future.

(1). A video camera should be coupled with the laser scanning microscope (LSM) to record the domain transition process in real time. The fastest time interval for the time series performed currently is about 0.3 second, which is too long to observe the rather quick domain transition process especially when the flow field is quite strong. So many details between the time interval are gone without recorded. It is because of this reason that the estimation of domain transition rate becomes very difficult if not possible. This problem can be solved by the video camera with real time capability.

(2). A heating stage with a temperature control is needed to incorporate into the laser scanning microscope (LSM). By changing temperature and measuring the rate constant of the domain transition process at different temperature, theoretically, it is possible to obtain the activation energy of domain shape transition process. As demonstrated previously, the domain transition process is most likely a kinetically controlled process. The activation energy is thus one of the most critical parameters to help understand the unique phase transition process.

(3). A device that can generate a stable, adjustable and known flow field should be designed and coupled into the lipid mulitlayers. As we have shown before, the domain transition process is basically an energetic process. Further quantitative analysis is thus hinged on how much energy is input into the system. Currently, a flow field is generated through shearing the microscope slides. The characteristic of the flow field and

consequently the corresponding energy input into the system is completely unknown. Furthermore, after the hydrodynamic flow is generated, everything is out of control. We can not increase the flow field in case the domain transition requires more energy, nor can we decrease the flow field if we want to observe the detailed domain transition process. Therefore, obtaining a flow field which is continuously adjustable with a known energy is the key to quantitatively analyze the process.

Conclusion

The domain shape evolution process between stripe and bubble under a hydrodynamic flow has been observed and characterized. A stripe is transformed to a bubble after passing an energy barrier corresponding to the bent or elongated stripe. A bubble with higher harmonic shape fuses with another bubble to form a stable stripe. These observations have directly shown that the domain shape transition process is a typical first order phase transition process. The domain transition process has been explained in terms of modulated phase based on the framework of competing interactions. It has been proposed that the competing forces are the shear force due to hydrodynamic flow and the hydrodynamic drag force that opposes the shear force. The energy difference between stripe and bubble at ground state has been estimated as about 3.9 kJ/mol. Future experiments has been suggested in order to quantitatively analyze the domain transition process.

Reference

1. Ouyang, Q. And Swinney, H. L. *Nature* **1991,** 352, 610

2. Seul, M. and Chen, V. S. *Phys. Rev. Lett.* **1993,** 70, 1658

3. Meinhart, H. *Models of Biological Pattern Formation* Academic: New York, 1982

4. Seul, M. and Andelman, D. *Science* **1995,** 267, 476

5. Andelman, D., Broçhard, F. And Joanny, J.-F. *J. Chem. Phys.* **1987,** 86, 3673

6. McConnell, H. M. *Proc. Natl. Acad. Sci. USA* **1989,** 86, 3452

7. McConnell, H. M. *Annu. Rev. Phys. Chem.* **1991,** 42, 171

8. Mayer, M. A. & Vanderlick T. K. *J. Chem. Phys.* **1994,** 100, 8399

9. Du, X.; Whallon, J. H.; Hollingsworth, R. I. *Langmuir* **1998,** 14, 5581

10. Stratton, C. J., Zasadzinski & Elkins, D. *Anat. Rec.* **1988,** 221, 503

11. De Gennes, P.-G. & Prost J. *The Physics of Liquid Crystals* Charendon: Oxford, 2nd

    edition, 1993

12. Nawa, N. & Nakamura, K. *Japan. J. Appl. Phys.* **1978,** 17, 219

13. Kawachi, M., Kogure, O. and Kato, Y. *Japan. J. Appl. Phys.* **1974,** 13, 1457

14. Keller, D. J., McConnell, H. M., & Moy, V. T. *J. Phys. Chem.* **1986,** 90, 2311

15. Benvegnu, D. J. & McConnell, H. M. *J. Phys. Chem.* **1992,** 96, 6820

16. McConnell, H. M. *Proc. Natl. Acad. Sci. USA* **1996,** 93, 15001

17. Läuger, J., Robertson, C. R., Frank, C. W. & Fuller, G. G. *Langmuir* **1996,** 12, 5630

18. Seul, M.; Sammon M. J. *Phys. Rev. Lett.* **1990,** 64, 1903

19. Thomas, E. N.; Witten, T. *Phys. Today* **1990,** 21, 27

20. McConnell, H. M. *Annu. Rev. Phys. Chem.* **1991,** 42, 171

21. Zasadzinski, J.; Schneider, M. B. *J. Phys. (France)* **1987,** 48, 2001

22. Bodenschatz E.; de Bruyn, J. R.; Ahlers, G.; Cannell, D. S. *Phys. Rew. Lett.* **1991,** 67, 3078

23. Seul, M. *Adv. Mater.* **1992,** 4, 521

24. Peters, R.; Beck, K. *Proc. Natl. Acad. Sci. USA* **1983,** 80, 7183

25. Möhwald, H. *Ann. Rev. Phys. Chem.* **1990,** 41, 441

26. Weis, R. M.; McConnell, H. M. *J. Phys. Chem.* **1985,** 89, 4453